Fachbereich 18
Elektrotechnik und Informationstechnik

TECHNISCHE UNIVERSITÄT DARMSTADT

# Short Primary Linear Drive Designed for Synchronous and Induction Operation Mode with On-Board Energy Storage

genehmigte
Dissertation

von
M.Sc. Tobias Rafael Fernandes Neto
aus Fortaleza/Brasilien

| | |
|---|---|
| Referent: | Prof. Dr.-Ing. Peter Mutschler |
| Korreferent: | Prof. Dr.-Ing. Bernd Orlik |
| Tag der Einreichung: | 07.02.2012 |
| Tag der mündlichen Prüfung: | 28.06.2012 |

D17
Darmstadt 2012

# Short Primary Linear Drive Designed for Synchronous and Induction Operation Mode with On-Board Energy Storage

Vom Fachbereich Elektrotechnik und Informationstechnik
der Technischen Universität Darmstadt
zur Erlangung des akademischen Grades eines
Doktor-Ingenieurs (Dr.-Ing.)
genehmigte Dissertation

von
**Tobias Rafael Fernandes Neto, M.Sc.**
geboren am 30. März 1981 in Fortaleza, Brasilien

| | |
|---|---|
| Referent: | Prof. Dr.-Ing. Peter Mutschler |
| Korreferent: | Prof. Dr -Ing. Bernd Orlik |
| Tag der Einreichung: | 07. Februar 2012 |
| Tag der mündlichen Prüfung: | 28. Juni 2012 |

D17
Darmstadt 2012

# Preface

The present PhD represents the result of my 4-years study and research in the Department of Power Electronics and Control of Drives (SRT) from Darmstadt University of Technology. I wish to thank all the people involved directly or indirectly in the process of my work.

First, I would like to express my sincere gratitude to Prof. Dr.-Ing Peter Mutschler, my supervisor and head of the Department, who introduced me to this very interesting research topic and gave me the opportunity to work under his able guidance. His enormous expertise and encouragement have been of enormous significance to me.

To Prof. Dr.-Ing. Bernd Orlik, I thank for his interest to be the second reviewer for his work.

I would like to thank CNPq for the financial support, providing me such wonderful opportunity to live in Germany and feel a new culture and a new outlook of life.

I thank the Darmstadt University of Technology for financially supporting my work.

I am deeply indebted to all my colleagues at the Department of Power Electronics and Control of Drives for the fine and challenging working atmosphere I had the pleasure to be surrounded with. Especially, I would like to thank also the workshop staff and the department's office which helped me a lot during these years.

I would like to thank God. I could never have done this without the faith I have in you, the Almighty.

I dedicate my life, my work, and whatever I have achieved in my life so far to my family. Especially, I would also like to thank my dear friends for your warm support and belief. Finally, I am very grateful to my wife, Lara, for her endless patience, understanding and love. With her, my life has so much meaning and fills with joy.

Darmstadt, 07th February 2012.

# Abstract

The idea of a flexible industrial manufacturing system for the transfer of material, tooling, processing/filling, etc., in which several vehicles can travel with high speed, high degree of independency and high precision is proposed in this thesis. Such flexible systems show a meaningful economic potential for modern manufacturing systems. The basic concept is that a linear motor has the secondary part fixed to the track while the primary (moving winding) travels along the track (short primary topology). The same principle can work in the other way around, arranging the primary in segments and letting the secondary (carrier) to move from segment to segment (long primary topology). The concept's implementation involves technical issues, such as: the position measurement, the energy and information transfer, the individual position and speed control of the vehicle in which varying speeds increase the possibility of collision, and the smooth transition between segments or different types of the secondary. Finally, multiple vehicles traveling at high speed, high positioning repeatability and rapid acceleration rates increase the production throughout and the reliability compared to conventional manufacturing conveyor systems. As an example, a transporting and processing system based on linear drives is a continuous and closed structure with multiple loops, which permits the safe transport of fragile loads. Although such solutions often need higher investment costs, the lack of mechanical coupling parts and wearing elements in these motors greatly increases their reliability.

The long primary topology allows a passive and lightweight vehicle (secondary), avoiding brushes and cables to transfer energy and information. For long distances, the primary is arranged in several electrical independent segments. On the other hand, the short primary configuration uses the winding mounted on the moving part (active vehicle) to produce the traveling wave, the secondary as guide way (induction rail or stationary magnets), and the energy and information should be transmitted contactless to the active vehicle. Regarding the features of the material handling application, the short or long primary topology can be used.

Short primary linear drives on passive track are advantageous in material handling applications, where high precision, moderate dynamic, very long track and closed paths are required. Nevertheless, depending on the requirements of the section, the costs can be reduced considerably by using a simple induction rail at the long transporting sections, instead of permanent magnets on the track. Therefore, in this thesis a combined operation of permanent magnet linear synchronous motor (PMLSM) and linear induction motor (LIM) is applied to operate the short primary as vehicle, avoiding adjustment or releasing of the material during the drive cycle. In summary, the passive track will consist of two section types: a high thrust force section (processing station) with PMLSM and a low thrust force section with LIM (transporting section). To the author's knowledge, using two operation modes (PMLSM / LIM) in the same drive is a new approach.

A theoretical and experimental study was conducted to assess the feasibility of employing the short primary linear motor for a flexible manufacturing system, in which a contactless energy transmission provides the basic power and an ultracapacitor (UC) storage system provides the peak power.

The system uses a bidirectional DC-DC converter between the ultracapacitor bank and the DC-link, to make sure that the ultracapacitor can store the braking energy and supply the peak power demanded by the active vehicle. A control strategy has been developed for controlling the ultracapacitor to deliver the peak of power, to charge, to protect against overvoltage and to recover the energy generated when the vehicle is braking.

A control strategy for the transition between the two operation modes (PMLSM / LIM) has been developed to provide a low speed drop, a sufficient thrust force, an optimal dynamic performance and a low power consumption, when it moves between the permanent magnets and the induction rail sections and considering that the linear scale is installed along the whole track.

Moreover, a sensorless transition control strategy was implemented in sections where no fast speed changes are necessary (transporting section). Then, a suitable motion strategy is necessary, especially during the transition between synchronous to induction motor operation (or vice versa) and between sensor based and sensorless sections of the track. The classic MRAS (Model Reference Adaptive System) speed and flux estimators are only activated in the sensorless induction motor operation mode. Surely, the costs can be reduced installing the position sensing system only within the processing station and its surrounding.

An experimental setup composed by software and hardware, was developed and implemented for the proposed system to perform a smooth transition between the different secondaries, and between sensor based and sensorless sections of the track. Finally, the obtained experimental data confirm the feasibility of the presented approach.

# Kurzfassung

Die vorliegende Dissertation präsentiert den Gedanken einer flexiblen industriellen Fertigungsanlage für den Materialtransport, die Bereitstellung von Werkzeugen sowie die Verarbeitung/Abfüllung etc., in der sich mehrere Fahrzeuge mit hoher Geschwindigkeit, einem hohen Grad der Unabhängigkeit und großer Präzision bewegen können. Derartige flexible Anlagen weisen ein bedeutendes wirtschaftliches Potential für moderne Produktionsstätten auf. Das grundlegende Konzept besteht darin, dass der Sekundärteil eines Linearmotors an dem Fahrweg befestigt ist, während der Primärteil (bewegte Wicklung) sich entlang dem Fahrweg bewegt (Kurz-Primärteil Topologie). Dasselbe Prinzip kann auf umgekehrte Weise funktionieren, wobei der Primärteil (Fahrzeug) in Segmenten angeordnet wird und es dem Sekundärteil gestattet, sich von Segment zu Segment zu bewegen (Langstator Topologie). Die Implementierung des Konzepts involviert technische Fragen, wie etwa: Lagemessungen, die Energie- und Signalübertragung ebenso wie die individuelle Position und Geschwindigkeitsregelung des Fahrzeugs, wobei variable Geschwindigkeiten die Möglichkeit von Zusammenstößen erhöhen, sowie die glatte Bewegung zwischen Segmenten oder verschiedene Typen von Sekundärteilen. Zu guter Letzt steigern multiple Fahrzeuge, die sich mit hoher Geschwindigkeit, einem hohen Grad der Wiederholgenauigkeit bei der Positionierung und hohen Beschleunigungswerten bewegen, im Vergleich zum herkömmlichen Transportband die Produktivität ebenso wie die Zuverlässigkeit. So stellt zum Beispiel ein Transport- und Verarbeitungssystem, das auf linearen Antrieben beruht, eine kontinuierliche und in sich geschlossene Struktur mit zahlreichen Regelkreisen dar, was den sicheren Transport von zerbrechlichem Ladegut gestattet. Auch wenn derartige Lösungen oft höhere Investitionskosten erforderlich machen, steigert der Verzicht auf mechanische Kupplungs- und Verschleißteile in diesen Motoren ihre Zuverlässigkeit.

Die Langstator-Topologie lässt ein passives Fahrzeug (Sekundärteil) mit geringem Gewicht zu, wodurch sich Bürsten und Kabel für die Übertragung von Energie und Information erübrigen. Für große Entfernungen wird der Primärteil in mehreren, elektrisch unabhängigen Segmenten realisiert. Auf der anderen Seite setzt die Kurzstator-Topologie die auf dem beweglichen Teil (aktives Fahrzeug) montierte Wicklung zur Erzeugung der Wanderwelle ein. Beim Sekundärteil als Führungsbahn (Induktionsschiene oder stationäre Magneten) sollen Energie und Information berührungslos an das aktive Fahrzeug übertragen werden. Im Hinblick auf die Eigenschaften der Anwendung für den Materialtransport können die Kurz- oder die Langstator - Topologie genutzt werden.

Der Kurzstator auf einem passiven Fahrweg ist für Anwendungen beim Materialtransport von Vorteil, wenn hohe Präzision, geringe Dynamik, ein sehr langer Fahrweg und geschlossene Bahnen gefordert sind. Dennoch können die Kosten je nach den Anforderungen des Abschnitts durch den Einsatz einer einfachen Induktionsschiene an den langen Transportabschnitten anstelle von Permanentmagneten entlang des Fahrweges beträchtlich gesenkt werden. Daher wird der kombinierte Einsatz eines Permanentmagnet-Linear-Synchronmotors (PMLSM) und eines Induktion-Linearmotors (LIM) für den Betrieb des Kurzstator-Fahrzeuges genutzt, wobei die

Justierung oder die Freigabe des Materials im Verlauf des Fahrzyklus vermieden wird. Der passive Fahrweg besteht also aus zwei Abschnitten: einem hohen Schubkraft-Abschnitt mit PMLSM (Verarbeitungsstation) und einem niedrigen Schubkraft-Abschnitt (Transportabschnitt).

Zur Einschätzung der Machbarkeit dieses Konzepts für ein flexibles Produktionssystem wurde eine theoretische und experimentelle Studie durchgeführt, bei der eine berührungslose Energieübertragung den Mittelwert der Antriebsenergie liefert und ein Speichersystem mit Ultrakondensatoren die Spitzenleistung abdeckt.

Die Anlage setzt einen Zweiquadrantensteller zwischen der Ultrakondensatorbank und dem Zwischenkreis ein, um sicherzustellen, dass der Ultrakondensator die Bremsenergie speichern und die Spitzenleistung bringen kann, die von dem aktiven Fahrzeug gefordert wird. Zur Steuerung des Ultrakondensators wurde eine Kontrollstrategie für die Abgabe der Spitzenleistung, zum Aufladen, zum Schutz vor Überspannung und für die Wiedergewinnung der beim Bremsen des Fahrzeugs erzeugten Energie entwickelt.

Zur Steuerung des aktiven Fahrzeugs wurde eine Übergangssteuerung-Strategie für einen geringeren Geschwindigkeitsabfall, eine ausreichende Schubkraft, eine optimale dynamische Leistung und geringeren Stromverbrauch entwickelt, wenn es sich zwischen den Permanentmagneten und den Abschnitten mit Induktionsschienen bewegt, wobei angenommen wird, dass der Linearmaßstab entlang des gesamten Fahrweges installiert ist.

Darüber hinaus wurde eine sensorlose Übergangssteuerung in Abschnitten implementiert, in denen keine schnellen Geschwindigkeitsveränderungen erforderlich sind (Transportabschnitt). Deshalb wird eine Bewegungsstrategie notwendig, dies vor allem während des Übergangs vom Betrieb mit Synchronmotor zum Betrieb mit Induktionsmotor (oder umgekehrt), sowie zwischen den mit Sensoren versehenen und den sensorlosen Abschnitten des Fahrweges. Die Geschwindigkeits- und Flussschätzung werden nur beim sensorlosen Induktionsmotor-Betrieb aktiviert. Mit Sicherheit lassen sich die Kosten reduzieren, wenn der Positionssensor nur innerhalb der relativ kurzen Verarbeitungsstationen und ihrer Umgebung installiert wird.

Für die vorgeschlagene Anlage wurde ein Versuchsaufbau mit Software und Hardware entwickelt und implementiert, um eine glatte Bewegung zwischen den verschiedenen Sekundärteilen sowie zwischen den mit Sensoren versehenen und sensorlosen Abschnitten des Fahrweges zu vollziehen. Letztendlich bestätigen die resultierenden Daten die Durchführbarkeit des vorgeschlagenen Ansatzes.

# Contents

# List of symbols

| | |
|---|---|
| $2p$ | :Number of poles |
| $\gamma$ | :Best transition position [m] |
| $\gamma_i$ | :Air-gap for induction operation [mm] |
| $\gamma_s$ | :Air-gap for synchronous operation [mm] |
| $\theta$ | :Phase angle of the reference voltage vector[rad] |
| $\varepsilon$ | :Error between the adaptive and reference reactive powers |
| $\lambda$ | :Duty cycle for DC model |
| $\sigma$ | :Blondel's leakage factor |
| $\lambda'$ | :$(1-\lambda)$ |
| $\beta_k$ | :Angular position of the secondary flux [rad] |
| $\beta_2$ | :Slip angle [rad] |
| $\beta_m$ | :Measured mechanical angle [rad] |
| $\hat{\beta}_1$ | :Estimated angular position of the secondary flux [rad] |
| $\omega_1$ | :Synchronous angular speed [rad/s] |
| $\omega_2$ | :Slip angular speed [rad/s] |
| $\hat{\omega}_m$ | :Estimated angular mechanical speed [rad/s] |
| $\omega_m$ | :Mechanical angular speed [rad/s] |
| $v_{syn}$ | :Synchronous speed [m/s] |
| $v_{synmax}$ | :Maximum synchronous speed [m/s] |
| $v_2$ | :Slip speed [m/s] |
| $v_m$ | :Mechanical speed [m/s] |
| $v_m$* | :Mechanical reference speed [m/s] |
| $v_{fm}$ | :Filtered speed feedback [m/s] |
| $\hat{v}_m$ | :Estimated mechanical speed [m/s] |
| $\Psi_2$ | :Secondary flux linkage [Wb] |
| $\Psi_{2A}$, $\Psi_{2B}$ | :Secondary flux linkage in rotating *AB*- reference frame [Wb] |
| $\Psi_{2a}$, $\Psi_{2b}$, $\Psi_{2c}$ | :Secondary flux linkage in (abc) reference frame [Wb] |
| $\hat{\Psi}_{2A}^{\ i}$, $\hat{\Psi}_{2B}^{\ i}$ | :Current model secondary flux linkage in rotating *AB*- reference frame [Wb] |
| $\hat{\Psi}_{2\alpha}^{\ i}$, $\hat{\Psi}_{2\beta}^{\ i}$ | :Current model secondary flux linkage in $\alpha\beta$- stationary reference frame [Wb] |
| $\hat{\Psi}_{1\alpha}^{\ i}$, $\hat{\Psi}_{1\beta}^{\ i}$ | :Current model primary flux linkage in $\alpha\beta$- stationary reference frame [Wb] |
| $\hat{\Psi}_{1\alpha}^{\ v}$, $\hat{\Psi}_{1\beta}^{\ v}$ | :Voltage model primary flux linkage in $\alpha\beta$- stationary reference frame [Wb] |
| $\hat{\Psi}_{2\alpha}^{\ v}$, $\hat{\Psi}_{2\beta}^{\ v}$ | :Voltage model secondary flux linkage in $\alpha\beta$- stationary reference frame [Wb] |
| $\Psi_{1A}$, $\Psi_{1B}$ | :Primary flux linkage in rotating *AB*- reference frame [Wb] |
| $\Psi_{1a}$, $\Psi_{1b}$, $\Psi_{1c}$ | :Primary flux linkage in (abc) reference frame [Wb] |
| $\Psi_{pm}$ | :Secondary flux generated by stationary magnets [Wb] |
| $\tau$ | :Pole pitch [mm] |
| $\Delta I$ | :Inductor current ripple [A] |

$\Delta V_{dclink}$ :Peak-to-peak output voltage ripple [V]
$\varpi_{z1}$ :Zero
$C_{dclink}$ :DC-link capacitance [F]
$C_{UC}$ :Ultracapacitor capacitance [F]
$d$ :Differential duty cycle for small signal model
$\hat{d}$ :Differential perturbed duty cycle for small signal model
$e_\alpha{}^i$, $e_{1\beta}{}^i$ :Current model back-EMF in $\alpha\beta$- stationary reference frame [V]
$e_{1\alpha}{}^v$, $e_{1\beta}{}^v$ :Voltage model back-EMF in $\alpha\beta$- stationary reference frame [V]
$F_{friction}$ :Friction force [N]
$F_{in}$ :Nominal thrust force for induction operation [N]
$F_o$ :Open-loop transfer function
$f_s$ :Switching frequency [Hz]
$F_{smax}$ :Peak thrust force [N]
$F_{sn}$ :Nominal thrust force for synchronous operation [N]
$F_w$ :Closed-loop transfer function
$i_1$ :Average capacitor current small signal model [A]
$i_{1A}$, $i_{1B}$ :Primary phase currents in rotating $AB$- reference frame [A]
$i_{1a}$, $i_{1b}$, $i_{1c}$ :Primary phase currents in (abc) reference frame [A]
$i_{1d}$, $i_{1q}$ :Primary phase currents in rotating $dq$- reference frame [A]
$i_{2A}$, $i_{2B}$ :Secondary phase currents in rotating $AB$- reference frame [A]
$i_{2a}$, $i_{2b}$, $i_{2c}$ :Secondary phase currents in (abc) reference frame [A]
$i_{2\alpha}$, $i_{1\beta}$ :Primary phase currents in $\alpha\beta$- stationary reference frame [A]
$i_{2\alpha}$, $i_{2\beta}$ :Primary phase currents in $\alpha\beta$- stationary reference frame [A]
$i_{m\alpha}$, $i_{m\beta}$ :Magnetizing current in $\alpha\beta$- stationary reference frame [A]
$i_a$ :Average terminal a current small signal model [A]
$i_b$ :Average terminal b current small signal model [A]
$i_c$ :Average terminal c current small signal model [A]
$I_c$ :Average terminal c current dc model [A]
$I_{dclink}$ :Average DC-link current [A]
$I_L$ :Average inductor current [A]
$i_L$ :Inductor current [A]
$I_L'$ :Average inductor current at boundary condition [A]
$i_{Lpeak}$ :Inductor peak current [A]
$I_{si}$ :Nominal current for induction operation [A]
$I_{mobile}$ :Mobile converter current [A]
$I_{smax}$ :Peak current for synchronous operation [A]
$I_{sn}$ :Nominal current for synchronous operation [A]
$I_{UC}$ :Ultracapacitor current [A]
$I_{UCmax}$ :Maximum average ultracapacitor current [A]
$I_{UCmin}$ :Minimum average ultracapacitor current [A]
$k_I$ :Proportional gain for the flux PI compensator

$k_2$ :Integral gain for the flux PI compensator
$k_{if}$ :Force constant for induction operation [N/A]
$k_{LIM}$ :Gain of the LIM current loop
$k_p$ :Gain of the PI controller
$k_{pi}$ :PI controller gain
$k_{PMLSM}$ :Gain of the PMLSM current loop
$k_{sf}$ :Force constant for synchronous operation [N/A]
$k_1^s$ :Proportional gain for the speed PI compensator
$k_2^s$ :Integral gain for the speed PI compensator
$L$ :Inductance [H]
$L_{min}$ :Minimum value of inductance for continuous conduction [H]
$l_i$ :Secondary length for induction operation [mm]
$L_{i1}$ :Primary inductance for induction operation [H]
$L_{i2}$ :Secondary inductance for induction operation (H)
$l_s$ :Secondary length for synchronous operation [mm]
$L_{s1}$ :Primary inductance for synchronous operation [H]
$L_{s2}$ :Secondary inductance for synchronous operation [H]
$M$ :Magnetizing self-inductance [H]
$m_v$ :Total mass [kg]
$P$ :Constant power [W]
$P_{em}$ :Electromechanical output power for induction operation [W]
$P_{in}$ :Instantaneous input power for induction operation [W]
$P_{mag}$ :Power stored in the magnetic field for induction operation [W]
$P_{ohm}$ :Copper losses for induction operation [W]
$P_{sem}$ :Electromechanical output power for synchronous operation [W]
$P_{smag}$ :Power stored in the magnetic field for synchronous operation [W]
$P_{sn}$ :Instantaneous input power for synchronous operation [W]
$P_{sohm}$ :Copper losses for synchronous operation [W]
$q^v$ :Instantaneous reference reactive power [VAR]
$q^i$ :Instantaneous adjustable reactive power [VAR]
$R_1$ :Primary phase resistance [Ω]
$R_2$ :Secondary resistance [Ω]
$R_{UC}$ :Ultracapacitor equivalent series resistance [Ω]
$R_L$ :Inductor resistance [Ω]
$R_{dclink}$ :Equivalent series resistance of the DC-link capacitors [Ω]
$T_D$ :Control time delay [s]
$T_i$ :Integral time of the PI controller [s]
$T_{LIM}$ :Time constant of the LIM current loop [s]
$t_{off}$ :Switch off period [s]
$t_{on}$ :Conduction period [s]
$t_{UC}$ :Ultracapacitor discharge time [s]

| | |
|---|---|
| $T_1$ | :Time intervals of applying $\vec{V}_1$ [s] |
| $T_2$ | :Time intervals of applying $\vec{V}_2$ [s] |
| $T_0$ | :Time intervals of applying the zero-voltage vectors $\vec{V}_0$ and $\vec{V}_7$ [s] |
| $T_a$ | :Time compare value for the primary phase voltage a [s] |
| $T_b$ | :Time compare value for the primary phase voltage b [s] |
| $T_c$ | :Time compare value for the primary phase voltage c [s] |
| $T_{PMLSM}$ | :Time constant of the PMLSM current loop [s] |
| $T_s$ | :Switching period [s] |
| $T_{sample}$ | :Sample time period [s] |
| $T_{secondary}$ | :Secondary time constant [s] |
| $T_{speed}$ | :Equivalent time constant of the speed control loop [s] |
| $T_{\alpha\beta}$ | :*abc* to $\alpha\beta$ transformation matrix |
| $T_{AB}$ | :$\alpha\beta$ to *AB* transformation matrix |
| $T_{set}$ | :Time constant of the first-order low-pass reference filter [s] |
| $T_{filter}$ | :Time constant of the low-pass feedback filter [s] |
| $u_{1A}$, $u_{1B}$ | :Primary phase voltage in rotating *AB*- reference frame [V] |
| $u_{1a}$, $u_{1b}$, $u_{1c}$ | :Primary phase voltage in (abc) reference frame [V] |
| $u_{1d}$, $u_{1q}$ | :Primary phase voltage in rotating *dq*- reference frame [V] |
| $u_{2A}$, $u_{2B}$ | :Secondary phase voltage in rotating *AB*- reference frame [V] |
| $u_{2a}$, $u_{2b}$, $u_{2c}$ | :Primary phase voltage in (abc) reference frame [V] |
| $u_{max}$ | :Maximum voltage variable [V] |
| $u_{max}$ | :Minimum voltage variable [V] |
| $u_{1a}$*, $u_{1b}$*, $u_{1c}$* | :Primary phase voltage reference in (abc) [V] |
| $u_{1\alpha}$, $u_{1\beta}$ | :Primary phase voltage in $\alpha\beta$- stationary reference frame [V] |
| $u_{2\alpha}$, $u_{2\beta}$ | :Secondary phase voltage in $\alpha\beta$- stationary reference frame [V] |
| $\vec{u}_1$ | :Primary phase voltage space vector [V] |
| $\tilde{v}_{cp}$ | :Instantaneous voltage between terminals c-p [V] |
| $\tilde{v}_{ap}$ | :Instantaneous voltage between terminals c-p [V] |
| $V_{dclink}$ | :DC-link voltage [V] |
| $v_{dclink}$ | :DC-link voltage small signal model [V] |
| $v_L$ | :Inductor voltage [V] |
| $V_{UC}$ | :Ultracapacitor voltage [V] |
| $V_{UCf}$ | :Ultracapacitor final voltage [V] |
| $V_{UCi}$ | :Ultracapacitor initial voltage [V] |
| $V_{max}$* | :Maximum value of the reference voltage vector [V] |
| $x$ | :Acquired position [mm] |
| $x$* | :Reference position [mm] |
| $\hat{x}$ | :Estimated position [mm] |

# Abbreviations

| | |
|---|---|
| AC | :Alternating Current |
| ADC | :Analog-to-digital Converter |
| CAN | :Controller Area Network |
| CCS | :Code Composer Studio |
| CPS | :Contactless Power Supply |
| DC | :Direct Current |
| DSP | :Digital Signal Processor |
| EMF | :Electromagnetic Field |
| ESR | :Equivalent Series Resistance |
| EVM | :Event manager modules |
| FOC | :Field Oriented Control |
| I/O | :Input / Output |
| IGBT | :Insulated Gate Bipolar Transistor |
| IPM | :Intelligent Power Module |
| KERS | :Kinetic Energy Recovery Systems |
| LIM | :Linear Induction Motor |
| LSM | :Linear Synchronous Motor |
| MC | :Motion Controller |
| McBSP | :Multichannel Buffered Serial Port |
| MMF | :MagnetoMotive Force |
| MRAS | :Model Reference Adaptive System |
| PC | :Personal Computer |
| PDPINT | :Power Drive Protection Interrupt |
| PLC | :Power Line Carrier |
| PM | :Permanent Magnet |
| PWM | :Pulse-Width Modulation |
| QEP | :Quadrature-Encoder Pulse |
| SPI | :Serial Peripheral Interface |
| SV | :Space Vector |
| UART | :Universal Asynchronous Receiver/Transmitter |
| VC | :Vehicle Controller |
| VSI | :Voltage Source Inverter |

# 1. Introduction

## 1.1. Linear motor

Nowadays, the control of electrical machines has an increasingly progress, due to the evolution of the power electronics components and the information processing devices, improving the efficiency and safety of industrial systems through the adjustment of the speed, thrust and braking control. The linear electric motors have taken a good place and they are now becoming widely used in industrial applications [1][2][3]. Linear motors are very similar to a rotary motor, as they convert electric energy directly into mechanical energy. Unlike the rotary motor, the linear motor performs a linear movement (linear thrust force), i.e. there is no rotary motion or torque production. Linear motors can be distinguished into two parts: the primary, which is responsible to generate the travelling electromagnetic field and the secondary, which generates a magnetic flux either by magnets or by induced currents. By the interaction of both fields, a linear force is produced. Furthermore, the primary is placed parallel to the secondary, and they are separated by a small air-gap.

The main linear motor advantage is when the linear motion is required. Often rotary electrical motors with a complex mechanical system of gears, belts, and pulley and screw systems are used to convert the rotary motion into linear motion. However, this increases the size of the system and reduces the overall system efficiency. Thereby, the use of a linear motor allows to improve the characteristics of an industrial system involving a linear movement of the load, like e.g. low operational and maintenance costs, high efficiency, no backslash, high production throughout and no extra mechanical coupling elements [3][4]. Therefore, for each type of rotary electrical machine such as: synchronous, induction, reluctance and direct current (DC), there is a linear equivalent.

Linear motors were first developed at middle of 19$^{th}$-century at the same time as the others rotary electrical machines [3]. Difficulties in driving the linear motor due to its operation characteristics, as well as the problems caused by the longitudinal end and transverse edge effects, restricted its use to a few applications. Moreover, the alternating current (AC) motor drives had initially fixed voltage and frequency supply, and a feasible solution to overcome these drive constraints were not available, limiting the application of such linear machines. With the mentioned problems, linear machines were rarely used for almost the entire first half of the XX century [2][3].

The greatest interest about linear motor started with its use for public transportation systems in the 1970s, for high speed transportations system with magnetic levitation and also wheel-on-rail traction cars [2][5]. Over the past few years the continuous progress in areas such as power electronics, machine design and numerical processing devices, has made that the linear motors can be found in several application areas, like: machine tools [6], roller coasters [7], aircraft launch system [8], elevators [9], ocean wave generators [10] and high speed transportation [11].

### 1.1.1 Linear motor classification and topologies

As the linear motors are equivalent to rotary machines, thus they can be splitted in various topologies and classifications. Figure 1.1 shows a brief general classification for the linear motors. The classification and topology of the linear motors studied in this thesis have been marked in bold in Figure 1.1.

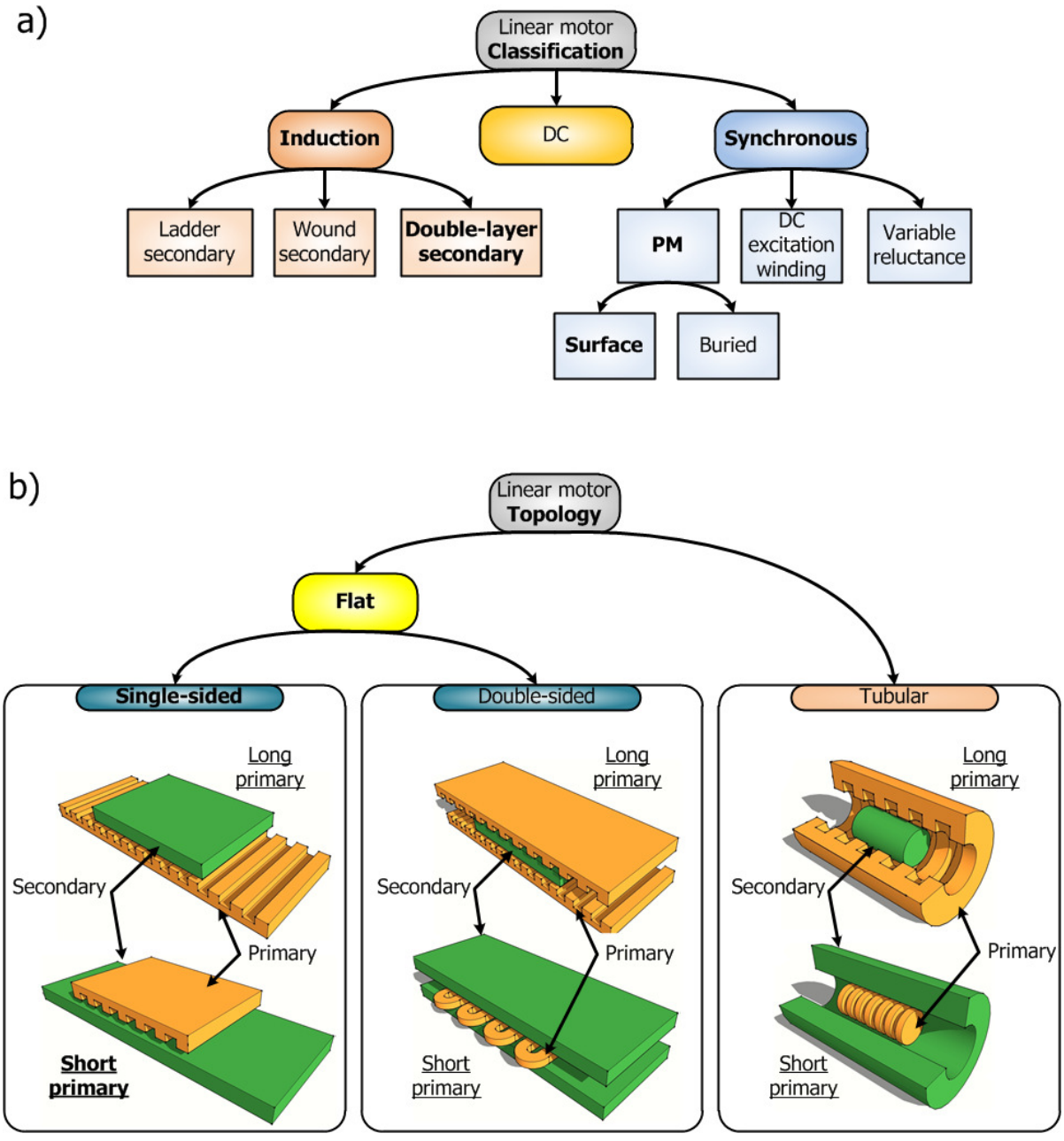


Figure 1.1: Linear motor a) classifications and b) topologies.

Figure 1.1b introduces the possible topologies for linear motors. The topology can be splitted in two geometric structures, which are: tubular or flat. Then, each structure can be built in long primary or in short primary topology.

For the flat geometry, the primaries can be either single-sided or assembled with two primaries in parallel (double-sided). Typically, the flat single-sided linear motor has a secondary with two layers. The first layer is a high-conductive and non-ferromagnetic plate (copper or aluminium) or permanent magnets (PM), and the second layer is a solid or laminated ferromagnetic yoke [2]. The secondary of a PM linear synchronous motor (PMLSM) with an *Hallbach* array does not require any ferromagnetic yoke [12]. The flat double-sided linear induction motor (LIM) has only the high-conductive plate, since the magnetic flux generated by the "top" primary is closed up by the core of the "bottom" primary [2]. Conversely, the secondary of the flat double-sided PMLSM has the permanent magnets mounted on a yoke [12]. The main advantages of double-sided linear motors are: the thrust force is four times greater than a flat single-sided linear motor and the normal attractive force between primary and secondary can be eliminated [2][12].

According to the topology, the definitions of long and short primaries are described below:

- Long primary: The electrical supplied part (primary) is longer in comparison with the secondary. Such configuration allows a passive and lightweight moving part (secondary).
- Short primary: The primary (winding), which produces the travelling wave, is shorter (or equal) than the secondary. Normally, the short primary configuration uses the primary as moving part, and uses the secondary as guide-way. The short primary has a better efficiency than a long primary, due to the lower copper losses.

In general, the long primary machine behavior is equivalent to a rotary machine, when the primary length has the same number of poles or is greater than the secondary. Nevertheless, the short primary machines are sensitive to edge effects, which reduce the thrust performance [3]. The impacts of the edge effects are negligible for low speed applications [2][13][14].

The rotary motors and linear motors can be divided in three main groups: induction motors, synchronous motors and DC motors, as shown in Figure 1.1a. The linear motors marked in bold are described below:

- LSM: The LSM is a motor in which the linear motion is produced in synchronism with the travelling magnetic field in the air-gap. The thrust force is generated by interaction of the travelling magnetic field (generated by the primary) and the magnetic field produced by the PM (or DC excitation winding), or by the permeance variation due to salient poles in both sides. The thrust density of the LSM is higher than the LIM. By using PM there is no need of transferring energy to the secondary.
- LIM: The LIM is a motor in which the excitation is induced by the primary (winding) in a conduction layer or ladder or windings (secondary). The primary produces a travelling magnetic field in the air-gap, inducing voltage in the secondary if there is a slip. The electromagnetic thrust force is produced by the interaction between travelling magnetic field and the induced secondary currents. The secondary or primary cannot move at the same speed of the travelling magnetic field because it would have no speed difference (slip), thus no thrust force. The LIM construction is very simple, as result it is less expensive than the PMLSM.

## 1.2. Material handling applications using linear drives

The high demands on material handling and transportation applications, which require flexible machines, short machine cycle times, high dynamic and linear movement are increasing steadily. In face of that, the linear motors are a suitable solution to these demands, since the linear motion and thrust force generation is direct, not requiring any mechanical transmission component subject to elasticity and wear. Thereby, they are found nowadays in many material handling markets, such as sealed environments for production of solar cells, LCD glass transportation, wood processing, loading gantry systems, packaging systems, machine tools, container transport, pharmaceutical production and food and beverage processing/filling.

### 1.2.1 Material handling applications using linear drives treated in the literature

In the last years, several papers about linear motors in material handling applications have been reported. The first ideas started with LIM, as in [15]. The given literature uses a short primary LIM with double-layer secondary to investigate its feasibility in material handling applications. The mover (primary) was intended to transport materials between three major cells in a prototype. The cells consist in load/unload cell, manufacturing cell and turning cell. The power supply is stationary, and it uses a cable run to the power transfer. Therefore, it decreases the vehicle degree of independency.

In [16], a hybrid system which uses a long primary transverse flux and longitudinal LIM, was investigated for a high speed and high acceleration material transport system. The longitudinal LIM is operated within straight primary units and the transverse flux LIM within curvilinear primary units. An oversized inverter must be used, due to the long primary topology (large reactive power) and the lower efficiency LIM. The drive control between both motors was not investigated.

In [17], a short primary LIM is proposed for LCD glass transportation. To keep the transportation without friction between wheels and track, the vehicle is magnetically levitated by electromagnets and PM, as depicted in Figure 1.2. The short primary is installed under the vehicle, thus the power is delivered by a contactless power supply (CPS). The position control is made by an

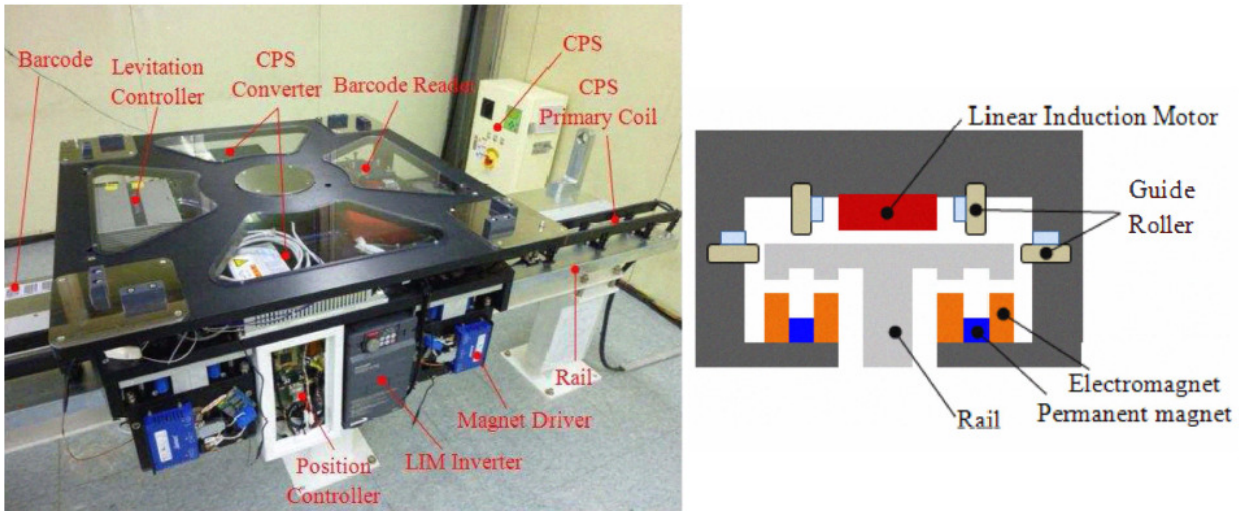


Figure 1.2: LCD glass transportation with a short primary LIM [17].

optical barcode reader. As the air-gap for the LIM must be small, the electromagnets are controller to maintain it constant. Such system reduces the generation of particles because it operates completely contactless.

Figure 1.3 shows another material handling application, where a sealed environment (high vacuum) is necessary for solar-cell fabrication [18]. There, one long primary PMLSM is driven with high accuracy (200µm). The primary segments were placed outside the vacuum environment, where in order to use convection to effectively dissipate the heat. Only the secondary transports the product within the sealed ambient.

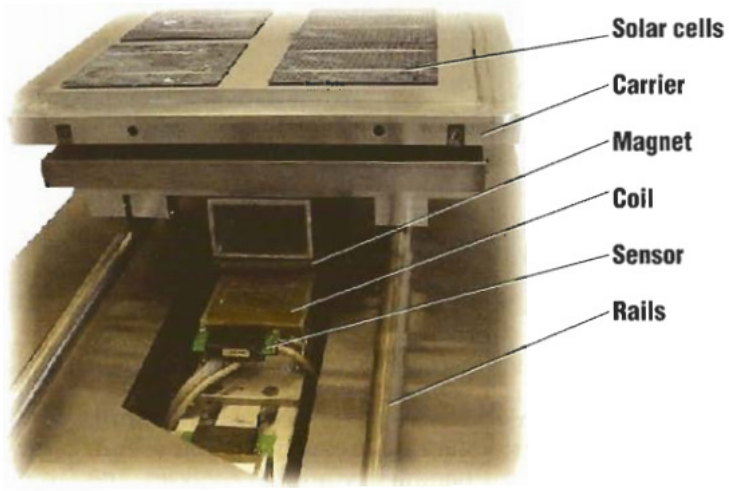


Figure 1.3: PMLSM for solar-cell fabrication [18].

One company which develops a commercial modular material handling system is the *MagneMotion* [19]. They use modules with 0.5m to 1m long which contain one or more primary blocks and inverters. All modules are connected in chain using RS-422 serial interface, and they are controlled by personal computers (PC) or power line carriers (PLC) by Ethernet. The transport system is based on PMLSM with passive vehicles (magnet array). Several vehicles can travel simultaneously in both directions above each module, as illustrated in Figure 1.4.

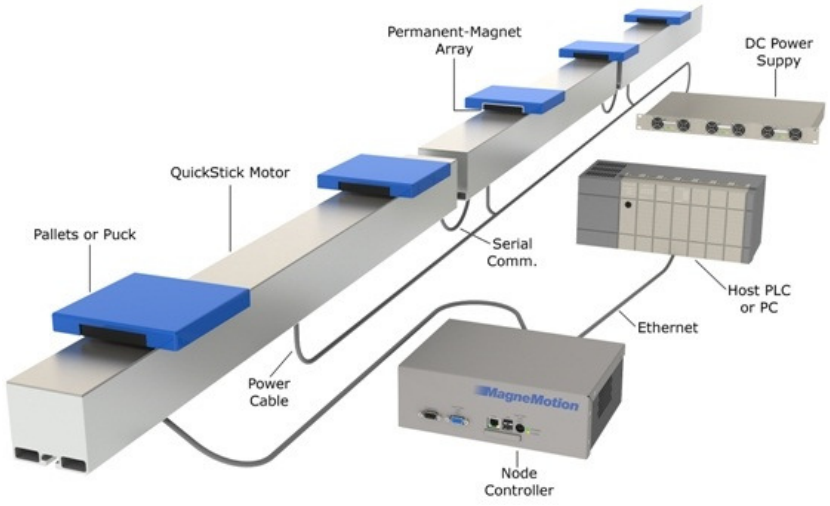


Figure 1.4: *MagneMotion* modules with passive vehicles [19].

### 1.2.2 Proposed industrial material handling system

In applications like industrial material handling systems, there are typically two different sections: 1.) sections where the work piece should only be transported and 2.) sections where the work piece is sequentially processed with high accuracy. Conventionally, the work piece is fastened within the processing station and released after the processing. As a result, the manufacturing time is significantly increased.

Figure 1.5 shows a simple example of combined transportation and processing of work pieces with a linear drive system. There, two sections can be distinguished. The first section is the processing station (P1…P4), where high thrust force and high precision are demanded, and the second section is the transporting zone where the vehicle moves forward with lower acceleration. In such flexible chain process with linear drives, the work piece is adjusted at the beginning of the process and released only at the end; that means there is no fastening or releasing of the work piece from the vehicle. Many benefits are achieved by having linear drives, such as: reduced manufacturing time, high dynamic, high precision (few µm), high productivity and reduced maintenance cost [20].

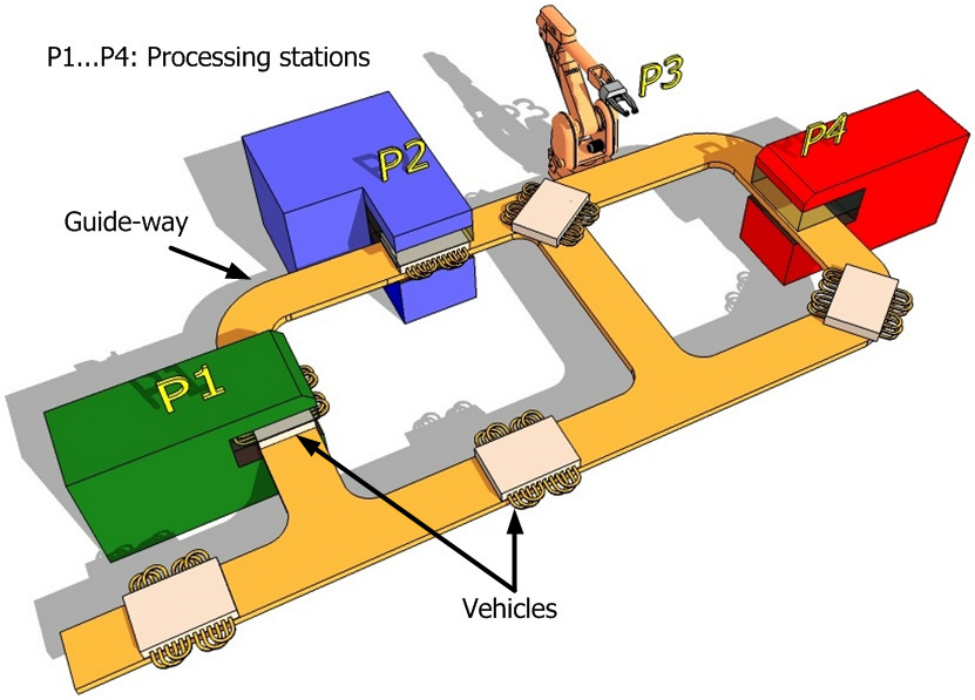


Figure 1.5: Simple example of combined transportation and processing of work pieces with a linear drive system.

Combined transportation and processing of work pieces using linear drive systems, as depicted in Figure 1.5, requires the following properties:

- On the guide-way (track) several vehicles must travel with a high degree of independency (all the vehicles can start and brake without dynamic restriction).
- Each vehicle has to be controlled very precisely by using a position sensor, when the vehicle operates within the processing section. Unlike the processing section, the sensorless motion control or one sensor with less accuracy may be used within the transporting section, in order to reduce the costs.

- The guide-way must allow for horizontal and vertical curves and for closed paths.

Regarding to the features of the material handling application, like: number of vehicles, track length, maximum speed and acceleration, sealed environment (vacuum), scalability and cost, the suitable linear drive topology (e.g. short or long primary) may be discussed. Therefore, the long and short primary topologies used to fulfill the system depicted in Figure 1.5 are presented and discussed in the following subsection.

### 1.2.3 Long primary topology (active track and passive vehicles)

Usually, when we think about linear motors, probably the first thing that comes in mind is the primary moving one load along a passive track. But recent development in data communication and logic controllers revealed new application areas. One type of such application is the long primary linear motor concept.

For the long primary configuration, the primary remains static as a track and the secondary is the work piece carrier. Hence, we have an active track (primary) with passive and lightweight vehicles (secondary), avoiding brushes and cables to transfer energy and information to the moving part and with the possibility to reach a high dynamic. In applications with very long active tracks, the primaries are arranged in several electrical independent segments, in order to reduce the reactive power of the dedicated inverter and save energy (only the segments where the vehicle is located are switched on, all the other are turned off) [20]. Furthermore, in short active track applications with multiples carries, the active track is also divided in many segments, since the desired number of vehicles depends on the size of the long primary (for individual vehicle motion control). The lowest possible number of segments per vehicle are two, considering that two segments are activated during the transition [21].

The position measurement is made by installing a scale at the passive vehicle and a stationary position sensor only within the processing station, so that, depending on the length to be acquired, the control system to be implemented is very complex (segmented position sensors) [22].

Under the application condition, that the vehicle must have a high dynamic inside the processing station, the flat single-sided PMLSM provides a good and feasible solution. Therefore, the moving secondary is a plate with a permanent magnet array. In single-sided PMLSM, the attractive force between the primary and secondary is very high, being necessary a robust mechanical structure. However, the double-sided topology can be used to fulfill the high acceleration requirement, without the strengthening of the mechanical structure.

For material handling application with long primary topology, there are two alternatives to supply each primary segment. The first option is multiplexing of inverters, which feed the primaries, by mechanical or electronic switches [20]. Such concept can reduce the number of inverters (two inverters per vehicle), but it seems not to be a good option, since the complexity and cost rise together with the track size [20][21]. The second alternative is to feed each primary segment with a dedicated inverter, so that a large number of primary segments imply a large number of inverters.

The physical distribution of the components for the second alternative produces another two possibilities. They are listed below:

- Long primary topology with centralized controllers: The inverters and controllers are accommodated together in a cabinet with all auxiliary components, and each inverter feeds one primary segment. Furthermore, each vehicle has its own vehicle controller. Then, all segments are connected by shielded motor cables [22].
- Long primary topology with distributed controllers: the inverters and controllers can be placed near each segment along the track with a common DC-link, reducing the cable installation costs [23]. Moreover, each primary segment has one vehicle controller.

#### 1.2.3.1 Long primary topology with centralized controllers

According to the previous subsection, the long primary topology with centralized controllers has one vehicle controller (VC) assigned to each vehicle, as depicted in Figure 1.6. The VC receives feedback data (current, speed and position) from the active inverter which feeds the respective segment. Then, the received data are processed by the VC control algorithm, and the switching time information is transmitted back to the inverter through an inverter-bus. The inverter-bus provides communication between each VC and each inverter inside one control cycle [21]. All inverters are connected at the same DC-link, and they are installed with the VCs within a cabinet, as illustrated in Figure 1.6. The motion controller (MC) is composed by industrial PC or PLCs which control the actual position of the vehicle.

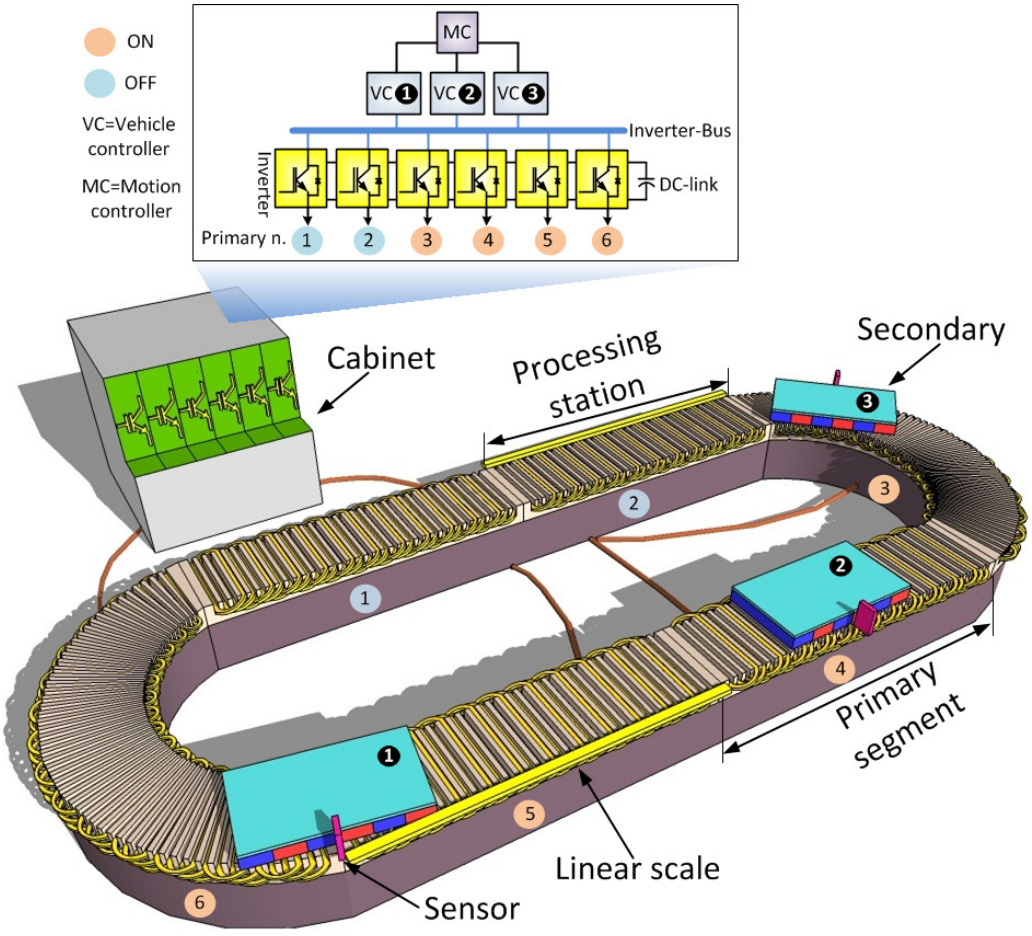


Figure 1.6: Long primary topology with centralized controllers.

For such topology, one control cycle must be smaller than $T_s$<125µs and it should be splitted in some intervals, which are equivalent to each controlled vehicle [21]. In one vehicle interval, two primary segments can be activated and controlled simultaneously. Since a good dynamic is demanded for such application, the number of travelling vehicles is limited, due to the reduction of these time intervals, which affords an increasing of the bandwidth. [20][21]. Such inverter-bus bandwidth limitation is the bottleneck point to increase the scale of the system. Figure 1.6 shows that the motor cable connection (cabinet ⇔ motor) could increase the overall costs for large applications with several segments. Altogether, the given topology is recommended for material handling system with low traffic density (low number of vehicle per track length).

#### 1.2.3.2 Long primary topology with distributed controllers

For industrial material handling application which requires a high traffic density, the long primary topology with distributed controllers is a suitable solution. The inverter-bus bandwidth limitation for centralized controllers is settled by placing the VC and inverter inside a module. Therefore, the module is responsible to supply the primary segment.

Figure 1.7 shows a system with three passive vehicles, six segments and six modules. The travelling vehicle is commanded directly by the module, since one VC is attributed to one inverter, as shown in Figure 1.7. In case of the vehicle be moving between two segments, the data (speed, position and current) are transmitted synchronously to the adjacent VC (inside the next module)

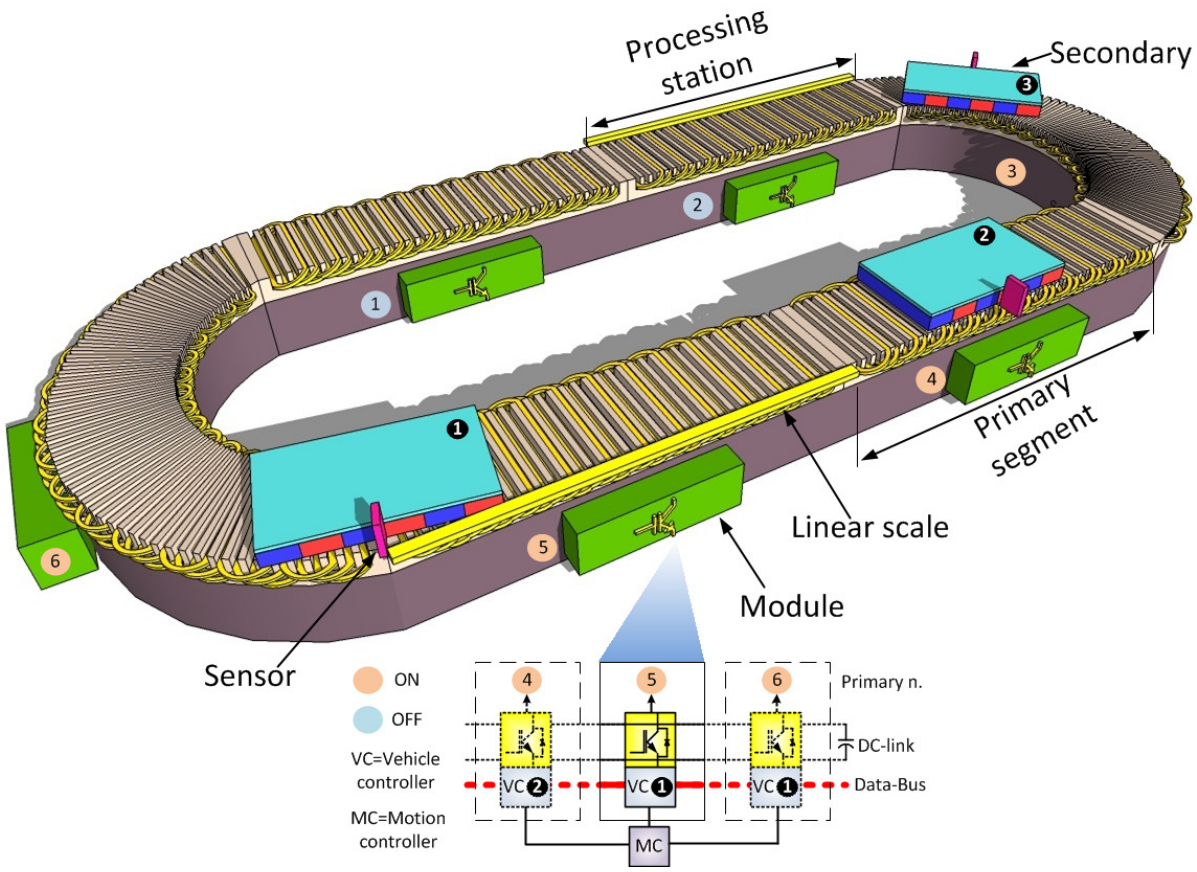


Figure 1.7: Long primary topology with distributed controllers.

using a high speed point-to-point communication, e.g. SPI or MSBSP [23]. The point-to-point communication connection is represented in Figure 1.7 as "data-bus".

Moreover, the motion controller (PLC or PC) is connected to each module by a physical industrial field bus interface, e.g. *EtherCAT* [23]. The MC generates the reference position and receives the actual position from all vehicles. Such a topology has a high degree of scalability, and future expansions can be easily implemented increasing the number of modules and primary segments. On the other hand, the implementation costs rise with the number of the segments and modules for a very large system. In order to minimize the end cost, a low cost intelligent power module (IPM) with no isolation between it and the VC, and current sensing with shunt resistors can be employed[20][23].

### 1.2.4 Short primary topology (passive track and active vehicles)

The short primary topology uses the three-phase winding mounted on the moving part (active vehicle) to produce the travelling magnetic field, and the secondary is the passive part, which is utilized as guide-way. The energy has to be transmitted to the vehicle, since the primary part must be supplied. Exact commutation of motor current, speed control and positioning require a linear measuring sensor which is typically attached to the active vehicle. Generally, in industrial application with very short track (e.g. machine tools), the power supply and the actual position are transferred and acquired from the moving primary by using a drag-chain or sliding contacts. The same drag-chain is also used to place the cables, which are used to read the actual position information. The inverter and controllers are located in a stationary cabinet near to the vehicle. The utilization of a drag-chain is improper for the system presented in Figure 1.5, where the vehicles should move along a track with closed paths and sharp curves.

Considering a material handling application with linear drives that is characterized by a very long track, low density of vehicles and moderate dynamic, the short primary topology affords a very simple track construction, allowing also sharp horizontal and vertical curves and causing lower implementation cost for the track than the long primary topology presented in the previous subsections. The limitations of the short primary topology are given mainly by the power supply system (energy must be transferred to the moving windings) and the significantly reduced dynamic (acceleration), due to a heavier vehicle than with the long primary topology. On the other hand, the system is more flexible in case of vehicle failure, since it can be easily removed, and the system can continue the work normally.

To fulfill the application requirement of transfer energy without contact, the vehicle should be supplied by using a contactless energy transmission, thereby the VC and all necessary converters are installed on-board the vehicle [24], as shown in Figure 1.8.

In order to improve the dynamic, to allow individual motion control for several vehicles (in case of all vehicles accelerate at the same time) and to absorb the generated braking energy, each vehicle is fed by an on-board ultracapacitor energy storage system. Together, both energy sources will increase the overall efficiency of the system. Moreover, it can reduce the size and cost of the contactless system, but weight, volume and complexity increases as well. In summary, the ultracapacitor storage system is used to increase the available peak power, and to absorb the

generated braking energy. At last, just one contactless energy system is responsible to supply energy to all vehicles, as depicted in Figure 1.8.

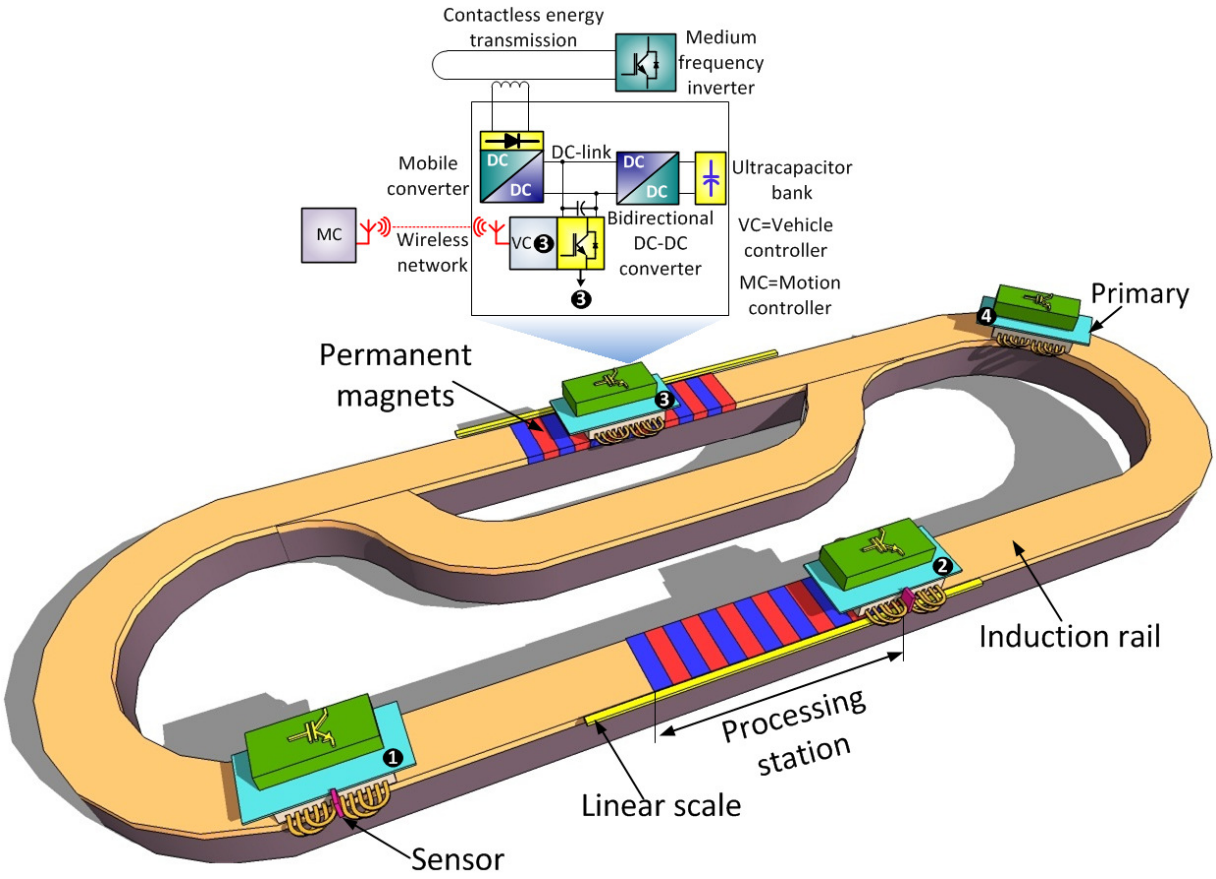


Figure 1.8: Short primary topology with contactless energy transmission.

This short primary topology has some advantages in comparison with the long primary topology, such as:

- The number of inverters and VS units is equal to the number of vehicles plus a stationary medium frequency inverter. Therefore, the number of vehicles is not limited as with the long primary topology (two primary segments for one vehicle).
- Reduced reactive power in the on-board inverter.
- The short primary has a better efficiency.
- The position sensor is attached to the active vehicle, thus one sensor per vehicle is necessary, and the acquired actual position is processed on-board of the active vehicle, making it simpler than the long primary topology.

The central MC produces the reference position to coordinate all active vehicles, and get the actual position data transmitted by the VC. To fulfill this communication demand, a wireless network should be utilized, since no contact is demanded.

Figure 1.8 outlines two sections. The first section is a station where the work pieces are processed. While processing, high thrust force and precision are necessary. The second section is outside the processing station. There, a lower thrust force is sufficient to keep the active vehicle moving with a low acceleration towards the next processing station. As a result, the passive track

will consist of two different section types: high thrust force sections using stationary permanent magnets (flat single-sided PMLSM) and low thrust force sections using an induction rail (flat single-sided LIM). The induction rail is composed of two layers: copper and back iron. Surely, the cost of the track can be reduced by saving the stationary permanent magnets outside the processing station.

Table 1.1 shows a comparison between the above described topologies. The optimal topology, i.e. long or short primary linear motor, depends on the requirements of the application.

Table 1.1 Comparison between short primary and long primary (distributed and centralized controllers) topologies.

| | | **Short primary** | **Long primary with centralized controller** | **Long primary with distributed controllers** |
|---|---|---|---|---|
| Power Supply | | One inverter per vehicle | Two inverter for one vehicle | Two inverter for one vehicle |
| | | Complex due to two energy sources (contactless system and ultracapacitors) | High number of inverters | |
| | | Better efficiency, heavy vehicle | Lower efficiency, big reactive power, light vehicle | |
| Control | | One controller per vehicle | One controller per vehicle | One controller per primary segment |
| | | Simple position measurement | Complex position measurement | |
| Costs | Track length | Expensive contactless system, cheaper secondary | Several primary segments and inverters | Several primary segments, inverters and controllers |
| | Number of Vehicles | Expensive on-board ultracapacitors | Two primary segments for one vehicle | Two primary segments for one vehicle |
| | Position sensor | One sensor per vehicle | The sensor depends on the length of the processing station (segmented measuring) | |
| Dynamic | | Moderated | High | High |
| Number of vehicles | | "Unlimited", expensive vehicle | Limited by the bandwidth and number of segments | Limited by the number of segments |
| Scalability | | Good | Medium | Very good |
| Primary | Force | High force | Medium force | Medium force |
| | Duty cycle | 100% | <100% depends on the traffic density | <100% depends on the traffic density |
| **Recommended application** | | **Very long track with low traffic density** | **Medium track with low traffic density** | **Long track with high traffic density** |

Very good Good Fair Poor Very Poor

## 1.3. Objectives and expected contributions

The interest to apply the linear drives in industrial manufacturing application increases, since they offer some benefits compared to the traditional rotary motors. Different material handling applications dictate different types of linear drives, so that the primary topology can be either long or short, as described in Table 1.1. Such versatility inspires us engineers to adapt the primary topology to specific needs. The long primary topology with distributed controllers can be utilized for long track applications. The short primary topology, however, offers the possibility to reduce the overall costs for an application with very long track and low density of vehicles by minimizing the number of vehicle controller, inverters and position sensors, and by using induction rail instead of permanent magnets outside the processing station. The dynamic of the short primary linear motor may be increased remarkably with the use of on-board ultracapacitors, achieving the dynamic level of the long primary linear motor with passive vehicles.

The principal purpose of this thesis is to design and implement a material handling and processing prototype, employing a short primary linear drive equipped with on-board energy storage (active vehicle with passive track), as explained in subsection 1.2.4. To set up this prototype, each vehicle will be fed by a contactless energy transmission system. The passive track comprises stationary permanent magnets (PMLSM) at the processing section, and an induction rail (LIM) at the transporting section. The position, speed, current control and energy management of the ultracapacitors will be developed and executed by an on-board control unit. Furthermore, outside the processing station the sensorless speed control will also be investigated.

In manufacturing applications, benefits like high productivity and precision are expected if the short primary linear motor topology is utilized. Although the long primary topology is preferred for long tracks material handling applications, the implemented prototype can lead to further considerations to find a reliable and feasible solution in a longer perspective.

## 1.4. Thesis outline

The contents of this thesis are organized as follows:

- In the first chapter, the background of this work is presented: where and why linear motors are used and what kind of advantages and drawbacks they have in comparison with rotary motors. Thereafter, three types of linear motor topologies are introduced and compared. Finally, an overview of the chosen topology is presented.
- Chapter 2 gives basic concepts of the contactless energy transmission. Subsequently, it introduces the on-board energy storage system and its design. The non-isolated bidirectional DC-DC converter topology and many operating modes are depicted. This topology is especially preferred for its high efficiency, simplicity and small weight and volume. The control strategy for the ultracapacitor energy management and the small signal ac model expressions under different conditions are derived and discussed. At last, the system power flow experiments are presented to verify the design results.
- Chapter 3 shows the development and design of the mechanical structure, where both types of secondaries are installed, and the linear motor selection. Moreover, the power

supply with the on-board inverter and control unit are discussed in details. Finally, the utilized data transfer method is described.

- The mathematical model for both linear motors (synchronous and induction) is explained in detail in chapter 4. The model was based on the rotating *AB*- reference frame. The given reference frame rotates with the secondary flux vector, so that its position is identical to the position of the secondary flux. Hence, the developed model is utilized for the field oriented control (FOC) which controls the thrust force with high dynamic.
- Chapter 5 presents the control design, the transition control strategy and the experimental test results for the developed system and the vehicle motion control strategy for the transition area between the permanent magnet (PMLSM) and the induction rail (LIM).
- Along the transporting section, sensorless methods should be used for estimation of the angular position of the secondary. The transition control strategy between the sensor based to sensorless control is depicted in chapter 6. The speed and flux estimators are based on rotating induction machines. Then, this control strategy is experimentally verified, discussed and presented.
- In chapter 7, conclusions and the future work are summarized.

The thesis is supplemented by the appendices.

# 2. Energy Supply Systems

In order to allow individual motion control for several vehicles, each vehicle should be fed by an on-board ultracapacitor energy storage system. Moreover, an inductive energy transmission is used to fulfill the application requirement of transfer energy without contact. One bidirectional converter is used to connect the storage system to the DC-link, making it responsible to manage the current flow (charge and discharge of the ultracapacitor). This chapter discusses each component utilized to provide energy to the material handling and processing system with active vehicle and passive track as proposed in chapter 1.

## 2.1. Contactless energy transmission

To transfer energy to the vehicle either a sliding contact like a pantograph or cable run or a contactless inductive energy transmission can be used. As described in the chapter 1, the vehicle must travel long distances and closed paths, thus the cable run is not applicable. Furthermore, in many industrial production environments, sliding contacts should be avoided.

Contactless energy transmission systems are widely recognized as an efficient method to transfer power through a magnetic field [25][26][27]. In addition, these systems offer typically 85-90% of efficiency, they are unaffected by dirt and humidity, and allow transferring power from a few mW up to hundred kW [27][28]. As a result, a commercially available contactless energy transmission system [29] will be applied in our experimental prototype.

Figure 2.1 shows a block diagram overview of a contactless energy transmission system. Essentially, a contactless energy transmission system can be divided in two parts: the stationary stage and the mobile stage.

The stationary stage has a conductor loop (line cable) installed along the path which is supplied by middle (or high) frequency alternating currents (or voltages), produced by a stationary inverter. The stationary frequency inverter (DC/AC resonant inverter) converts the three-phase line input into a medium frequency output. The mobile stage is not connected electrically with the primary, and it is composed by a moving pick-up coil used to extract power. Usually, the secondary output power is regulated through a dedicated converter and control unit to meet the requirements specified by the load. The electric power can be transferred to a single pick-up or multiples pick-ups from the same primary conductor [29][30], as depicted in Figure 2.1. Therefore, the contactless energy transmission used for long distances consists generally of a stationary resonant inverter and a large air-gap sliding transformer (pick-up).

The secondary pick-up winding used in the system, usually consists of a ferrite core and Litz coils. It can have different mechanical construction designs such as: u-shape and flat cores as illustrated in Figure 2.2. The flat core pick-up usually is utilized in floor conveyor systems and has a low electromagnetic coupling. Conversely, the u-shape pick-up has an efficient electromagnetic coupling and high performance, even with small pick-up construction sizes [29][30].

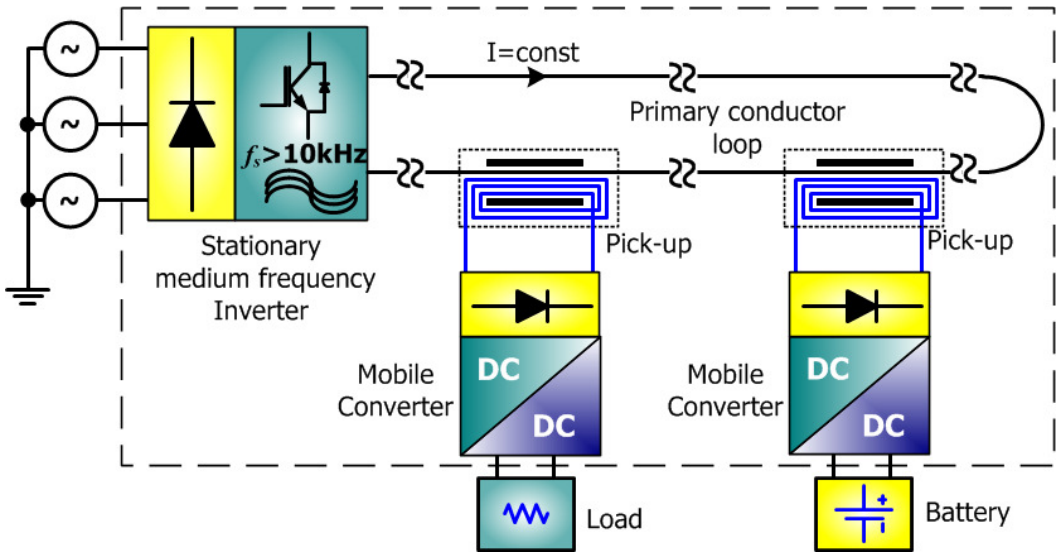


Figure 2.1: Contactless energy transmission system overview.

The pick-up has been identified as the most important component of this system [31], because the primary and the secondary must be tightly magnetically coupled. Generally, to reduce the secondary leakage inductance and improve the magnetic coupling, the pick-up should have a long and narrow design [31]. The system is similar to a conventional single phase transformer but with a large air-gap. Due to the large air-gap between primary and secondary, the primary and secondary leakage inductances are large, the main inductance is small and the magnetizing current is large (producing large conducting losses).


Figure 2.2: MOVITRANS a) THM10E flat b) THM10C U-shaped pick-up units from SEW Eurodrive [29].

The medium frequency inverter contains a compensation network, which transforms the generated square wave voltage into a constant sinusoidal alternating current. Furthermore, since the largest part of the circulating current is reactive, it is necessary to tune the resonant circuit using a resonant capacitor. The resonant capacitor will set the resonant frequency to the value of the switching frequency and will provide the excitation current to the primary conductor loop, thus only the real power will be supplied by the converter. As a result, the compensation network reduces the output harmonics and compensates the reactive power of the primary stage [27][29][32].

The stray inductance compensation can be made either by series or by parallel resonant capacitor placed at the primary and/or secondary. As described above the primary compensation is

used to minimize the reactive power, whereas the secondary compensation is utilized in order to improve the power transfer capability [32].

The parallel primary compensation is used in applications that require large primary current i.e. application with concentrated primary coils [33][34]. The series primary compensation is utilized to reduce the primary voltage to manageable levels. One example of the primary series compensation is for mining application, which has a very long primary conductor loop [35].

The series secondary compensation provides a constant output voltage, being well suited to supply variable speed AC drives [36]. On the other hand, parallel secondary compensation yields a constant output current, being suitable for applications such as battery charging [32][37]. Finally, the chosen compensation topology depends on the required load characteristics.

The medium frequency inverter generates a fixed frequency, aiming to minimize the weight and volume of the secondary pick-up, to increase the transferred power and to reduce the audible noise [38]. To decouple the loads in case of multiple pick-ups (see Figure 2.1), a primary constant current is required[29][32].

The primary conductor loop consists of two long insulated cables. The electromagnetic emission can be minimized by a close spacing between the outgoing and return cables [31]. Moreover, the line cables are made of Litz wire to reduce eddy currents and losses, and they are inserted in nonconducting supports [29][31], as depicted in Figure 2.3.

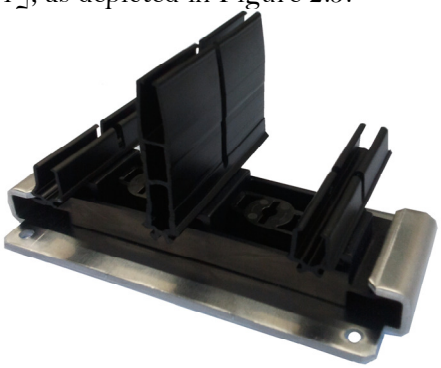

Figure 2.3: MOVITRANS TIS10A profile supports of nonconducting material from SEW Eurodrive.

The mobile converter converts the current from the pick-up into DC voltage, thus providing energy to the active vehicle. In general, the secondary converter consists of a passive bridge and a Boost converter [29][30][31][39].

With the advantages mentioned above, the contactless energy transmission provides a good solution in application of short primary linear drive with very long track. But it keeps the drawback of limited peak power in case of many vehicles accelerating at the same time. One possible solution to overcome its drawback is the use of an ultracapacitor energy storage system. This be described in the following section.

An overview of the topology is given in Figure 2.4.

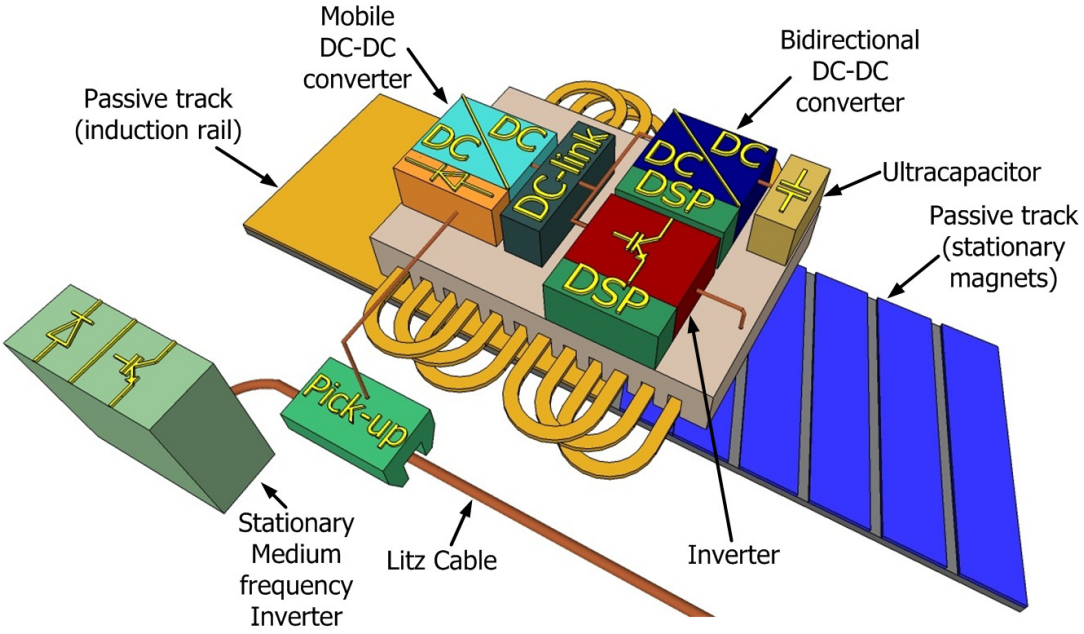


Figure 2.4: Active vehicle fed by a contactless energy transmission and an ultracapacitor energy storage system.

### 2.1.1 Contactless energy transmission system components design

The contactless energy transmission system, which is utilized in the experimental setup, is a commercial/industrial equipment available from *SEW Eurodrive*. The system is composed by a stationary converter, a transformer module, a U-shaped pick-up, a mobile converter and installation equipments (Litz cables, profile support and installation plates). The contactless energy transmission system specifications are shown in Table 2.1.

Table 2.1 Specifications of the contactless energy transmission [29].

| **Stationary converter** | | **Mobile DC-DC converter** | |
|---|---|---|---|
| Rated power | 4kW | Rated power | up to1.8kW |
| Switching frequency | 25kHz | Specific energy | 3.63Wh/kg |
| Line input voltage | 380-500Vac | Voltage output | 500Vdc+24Vdc |
| **U-Shaped pick-up** | | **Line Cable** | |
| Rated Power | 800W | Length | 7m |
| Peak Power | 900W | Wire | Litz, 8mm² |
| Resonant capacitor | 1x4µF;1x8µF;1x16µF | Liner cable current | 60A |

The structure of the experimental system which was built at our institute is described in details in chapter 3.

## 2.2. Ultracapacitor

If a voltage is applied across two electrodes immersed in a nonconducting fluid, there is no current flowing and a static electric field is developed due to the accumulation of charges at both electrodes, thus energy is stored in the electrostatic field. This passive electrical component is called capacitor [40].

The first device that stored energy in the electric double-layer interface, known as ultracapacitor, was developed and patented in 1966 by *Standard Oil of Ohio* (SOHIO) [41]. The ultracapacitor construction is composed by a "sandwich" with two metal-foils electrodes that allows a voltage to be applied across the cell. These metal-foils electrodes are coated with two double-layers of activated carbon with high surface area and porosity (one at each electrode), and they are immersed in an aqueous or organic electrolyte salt solution, as shown in Figure 2.5. An ion-permeable separator (i.e. glass paper) is situated between the electrode interfaces, in order to avoid an electrical contact, but still allows charged ions to travel between both electrodes through the separator. Therefore, the stored electrical charge in an ultracapacitor is similar to the conventional capacitors, with the difference that the charges accumulate at the two double-layers of the activated carbon [42].

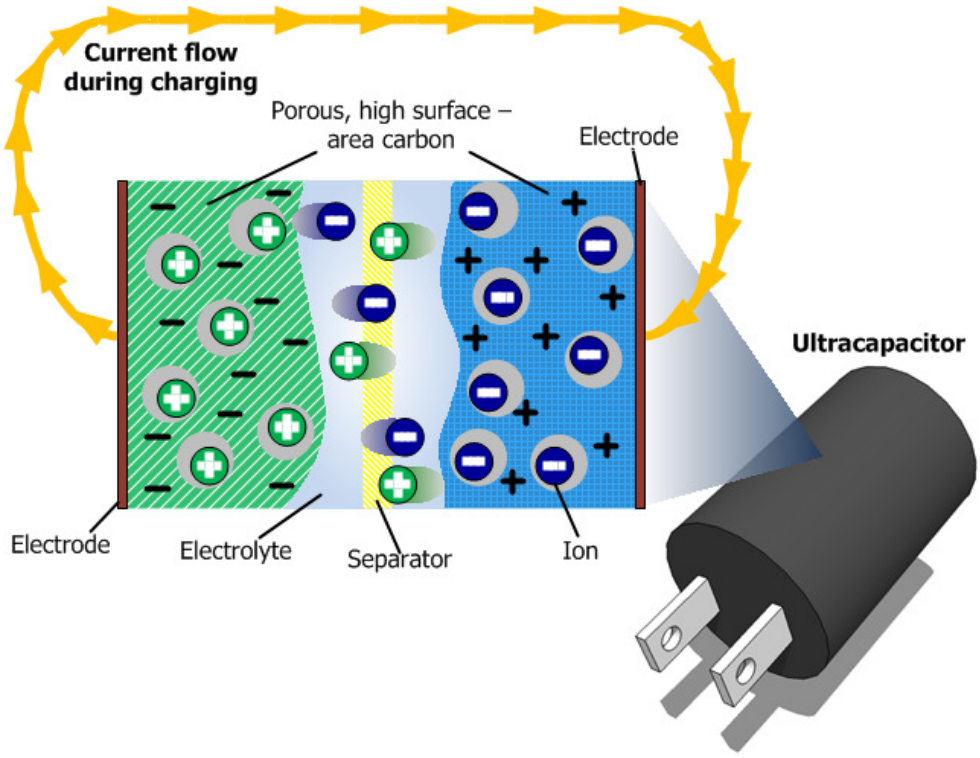


Figure 2.5: Internal structure and ion charges distribution of an ultracapacitor.

The electric propriety of an ultracapacitor is strongly dependent on the porosity of the activated carbon and on the molecular size of the electrolyte ion [41]. The activated carbon layers have specific surface area of 1000 to 2200 $m^2/g$ and a physical separation distance in order of few nanometers [43]. Therefore, the ultracapacitors can achieve a high capacitance value, making it able

to store a high value of energy in comparison to a conventional capacitor with the same volume and mass.

Generally, the ultracapacitor voltage rating is lower than a conventional capacitor. The voltage rating for ultracapacitors with aqueous electrolyte is typically 0.9V and with organic electrolyte is 2.7V. Organic electrolyte ultracapacitors have higher specific energy but higher resistance than aqueous types. Low conductivity of organic electrolyte ultracapacitor results in higher equivalent series resistance (ESR), but this issue is overcome by other manufacturing techniques [41].

Ultracapacitors have higher energy density and power density and both parameters discern a storage system as shown in Figure 2.6. The energy density represents the amount of energy stored per mass unit (Wh/kg) or per volume unit (Wh/m3) and the power density depicts the speed that some amount of energy can be transferred per unit of mass (W/kg) [44]. In terms of energy and power density, the ultracapacitor can be placed between batteries and conventional capacitors as shown in Figure 2.6 [45][46]. On the one hand the conventional capacitor can deliver a bigger amount of energy in few milliseconds. Conversely, the batteries represent a better relation between cost and energy storage, but it is able to store and deliver energy slower than an ultracapacitor.

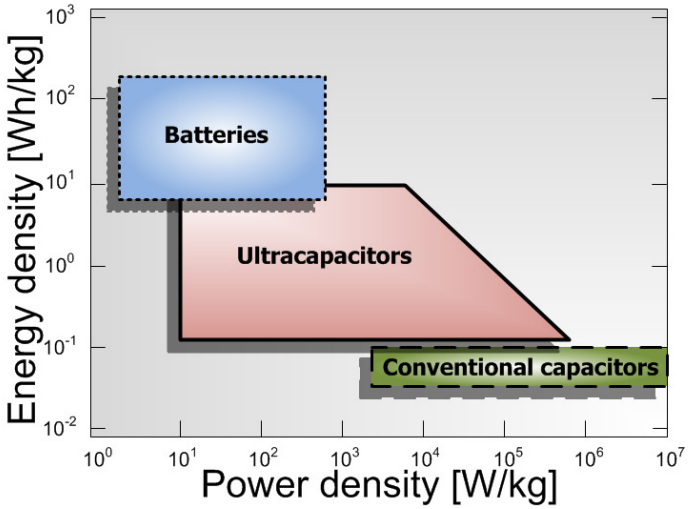


Figure 2.6: Ragone chart showing energy density vs. power density.

The benefits of using ultracapacitors are listed below [44][45]:

- Long life cycle, which makes the device environmentally friendly.
- They can be repetitively hard charged and deep discharged.
- Since they can be fully charged from a deep discharge within a few seconds, it turns a promising for use in regenerative braking systems.
- Low ESR, hence high efficiency and low heating levels.
- High output power.
- High specific power.
- No memory effect.

The drawbacks are [44][45]:

- Serial connections are needed to achieve higher voltages.
- High short circuit current caused by the very low ESR.

- High cost per watt.

Because of the advantages described above, these components cover a wide field of power electronics applications, especially in applications where the high power peak and hybrid electric systems are necessary.

For the proposed application of short primary linear drive, the use of on-board energy storage with ultracapacitor will surely increase the peak power available for the active vehicle, solving the limited peak power problem of the contactless energy transmission (in case of all vehicles accelerate at the same time).

### 2.2.1 Modeling of an ultracapacitor

As the charge storing mechanism of an ultracapacitor is different from the conventional capacitor, generally the traditional capacitors models are inadequate. Many different models have been proposed for the ultracapacitor, but in the special case, where the ultracapacitor is used in a system where it is slowly discharged (over few seconds), the simplified equivalent circuit depicted in Figure 2.7 can be used [47][48].

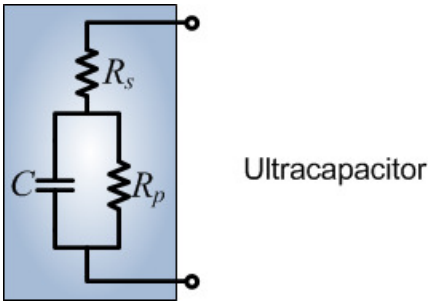


Figure 2.7: Ultracapacitor equivalent circuit.

Figure 2.7 shows an equivalent circuit which it is composed by three ideal circuit elements, a capacitance *C*, a series resistor and a parallel resistor. During the ultracapacitor charging and discharging, the series resistance components contribute to the energy losses and reduce the terminal output voltage. The parallel resistance represents the current leakage effect, thus its impact in long term period is the dropping of the storage energy level [47][48].

To reach higher voltage rating with an ultracapacitor, many cells should be connected in series; hence a common current flow through all cells. Avoiding the risk of one cell be overcharged (exceeding its voltage limit), active or a passive balancing circuit to regulate the cell voltage is employed. The passive circuit consists in a resistor connected in parallel with the cell's terminal making a voltage divider. The active balancing circuit is built using an electronic circuit connected in parallel with each cell. The active balancing circuit is designed to "trigger" at the specific cell voltage and upon the "trigger" will work to reduce the voltage level on the cell below the threshold voltage [49].

The ultracapacitor can be dimensioned by the peak power of the system or by maximum generated energy that would be absorbed during the braking at maximum speed. Normally, the accelerating procedure is more rigorous than the braking procedure in consequence of the mechanical

losses. In this case, the ultracapacitor should guarantee that it delivers the required peak power, thus the capacitance under constant power discharge is determined by equation (2.1).

$$C_{UC} = \frac{2Pt_{UC}}{\left|V_{UCi}^{\ 2} - V_{UCf}^{\ 2}\right|} \tag{2.1}$$

where: $C_{UC}$ is the ultracapacitor capacitance,
$t_{UC}$ is the discharge time,
$V_{UCf}$ is the final voltage,
$P$ is the constant power,
$V_{UCi}$ is the initial voltage.

Similarly, the maximum average delivered current $I_{UCmax}$ occurs at the final voltage, as shown in Figure 2.8. Then, the maximum current is given by (2.2).

$$I_{UC\max} = \frac{P}{\sqrt{V_{UCf}^{\ 2} - \frac{2Pt_{UC}}{C_{UC}}}} \tag{2.2}$$

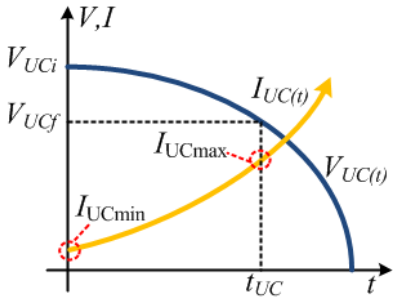


Figure 2.8: Ultracapacitor voltage and current functions for a constant power discharge.

The purpose of sizing an ultracapacitor bank (several ultracapacitors connected in series) is to minimize the mass and the volume carried by the active vehicle. The performance of an ultracapacitor can be characterized by its terminal voltage during the charge/discharge with different current rates.

### 2.2.2 Ultracapacitor bank design

The ultracapacitor bank can be designed in such way that its storage capability should be large enough to deliver the peak power required during the acceleration, to absorb the generated braking energy during the braking when the vehicle moves at the maximum speed and to keep the vehicle travelling with constant speed outside the processing station (transporting section). Based on the contactless energy transmission rated power (4kW), the ultracapacitor power energy was designed for our experimental setup. That means the ultracapacitor must be able to deliver 4kW for one second (4kJ).

The active vehicle weighs around 54kg, thus its kinetic energy at 3.6m/s (maximum speed) is about 350 Joules. The generated amount of energy must be absorbed by the ultracapacitor.

The ultracapacitor final voltage $V_{UCf}$ was chosen through the real voltage gain of the designed bidirectional DC-DC converter (see appendix A.1.5) which will be described in the next subsection. Now, taking the equation (2.1) and considering $P$=4kW, $t_{UC}$=1s, $V_{UCf}$=80V and $V_{UCi}$=140V, respectively the calculated ultracapacitor capacitance will be approximately 0.6 Farads. However, the

ultracapacitor bank was implemented with 10 series-connected ultracapacitor packs (BPAK0058 from *Maxwell Technologies*). These packs are composed by six cells (2.5V each) in series. One pack has 58F, an ESR of 19mΩ and a voltage rating of 15V [50]. This results in an ultracapacitor bank with 5.8 Farads, an equivalent series resistance of 190mΩ, and a total voltage of 150V (limited per software to 145V). The ultracapacitor voltage is allowed to drop from 140Vdc to 80Vdc, enabling us to deliver 38.2kJ of useful energy. This amount of energy permits us to take 4kW during 9.5 seconds, which is more than "enough power" for a good acceleration in our implemented experimental setup. Figure 2.9 illustrates one BPAK0058 ultracapacitor pack and Table 2.2 its specifications.


Figure 2.9: Ultracapacitor pack BPAK0058 from *Maxwell Technologies*.

Table 2.2 Specifications of the BPAK0058 ultracapacitor pack [50].

| Capacitance | 58F | Weight | 560g |
|---|---|---|---|
| ESR | 19mΩ | Pack voltage | 15V |
| Specific power | 3000W/kg | Specific energy | 3.63Wh/kg |
| Maximum peak current, 1s | 80A | Rated current | 20A |
| Balancing | Active | Leakage current | 1mA |
| Isolation Voltage | 1.100V | Volume | 0.566L |

The braking energy resulting from one braking at maximum speed (3.6m/s) corresponds to 0.57% of ultracapacitor maximum energy level. Therefore, if the ultracapacitor is fully charged (140V) the vehicle can stop few times (neglecting the losses) until the ultracapacitor overvoltage protection operates at 145 V.

## 2.3. Bidirectional DC-DC converter

The bidirectional DC-DC converter with an energy storage component has become a promising choice for many power-related systems, including Kinetic Energy Recovery Systems (KERS), hybrid vehicle, fuel cell vehicle and so on [45][46]. It will reduce the cost and improve the overall efficiency

of the system. Therefore, to store and deliver the ultracapacitor energy a mobile DC-DC converter should be designed and implemented.

The suitable power converter topology is directly depended of the overall system efficiency, voltage gain, complexity, mass, volume, cost and ease of control. Thus, the simple non-isolated bidirectional DC-DC converter (Figure 2.10) topology is selected to connect the ultracapacitor bank to the high voltage DC-link. This topology has the advantages of a reduced number of IGBTs, fewer passive components and a simple circuit.

Figure 2.10 shows the bidirectional DC-DC converter, in which the ultracapacitor is represented by a voltage source and its ESR. This topology establishes the controlled bidirectional power transfer between both sources as long as the ultracapacitor voltage is smaller than the contactless energy transmission output voltage. If this condition is not kept, a current will flow through the anti-parallel diode of T1.

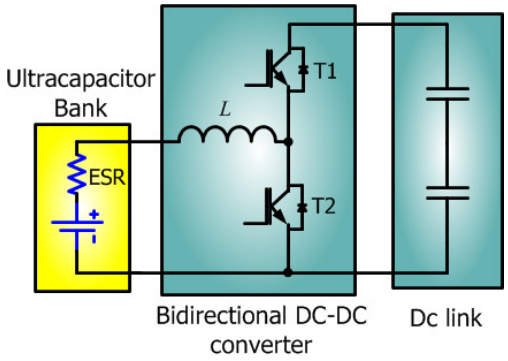


Figure 2.10: Bidirectional DC-DC converter equivalent circuit.

The bidirectional DC-DC converter works in two ways: two-quadrant operation and Buck mode. During the two-quadrant operation (Figure 2.11a), the converter is used to step-up (boost mode) the ultracapacitor voltage, therefore the output voltage is greater than the input voltage. The IGBTs T1 and T2 are complementary switched ON and OFF at a controlled duty cycle, maintaining the DC-link voltage at the rated value. When T1 is OFF and T2 ON, energy is taken from the ultracapacitor and stored in the inductor *L*. When T1 is switched ON and T2 OFF, the energy stored in *L* is transferred to the DC-link. During the Buck mode (Figure 2.11b), the converter charges the ultracapacitor with energy from the contactless energy transmission system, stepping down the DC-link voltage. That operation is accomplished with a controlled operation on T1 and T2 is kept always OFF. When T1 is switched ON, the energy goes from the DC-link to the ultracapacitor, and *L* stores part of this energy. When T1 is switched OFF, the remaining energy stored in *L* is transferred to ultracapacitor, through the anti-parallel diode of T2.

The advantages to work with complementary switching of T1 and T2 during the two-quadrant operation are: the converter operates always in continuous-conduction and during the braking the generated energy is directly absorbed by the ultracapacitor. The Buck mode is only utilized when the ultracapacitor has low energy level or it is discharged. Therefore, the bidirectional DC–DC converter should operate in suitable mode according to the condition of the ultracapacitor bank and the DC-link voltage.

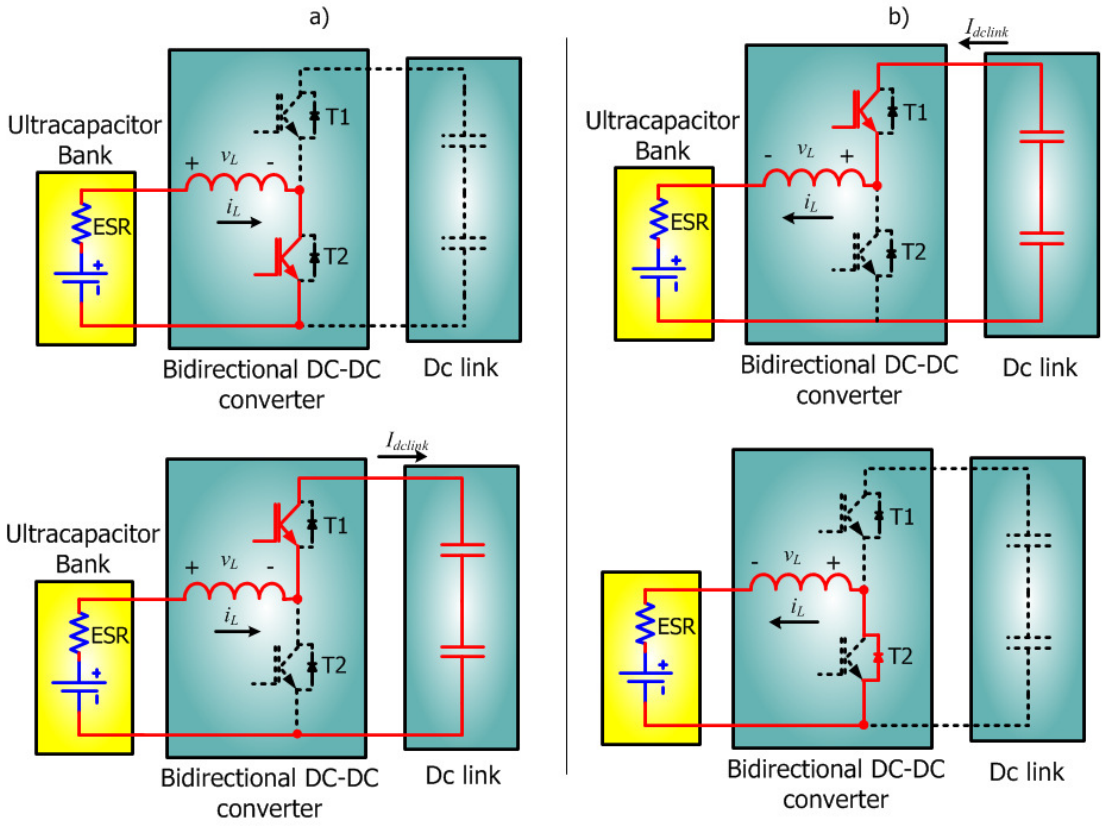


Figure 2.11: a) Two-quadrant operation b) Buck operation.

In the two-quadrant operation (boost mode), if the converter works in steady state the time integral of the inductor voltage over on time period must be zero.

$$V_{UC}t_{on} + (V_{UC} - V_{dclink})t_{off} = 0 \tag{2.3}$$

where: $V_{UC}$ is the average ultracapacitor voltage,

$V_{dclink}$ is the DC-link voltage,

$t_{on}$ is the conduction period,

$t_{off}$ is the switch off period.

The conduction period of the IGBT T2 is:

$$t_{on} = \frac{(V_{dclink} - V_{UC})t_{off}}{V_{UC}} \tag{2.4}$$

Dividing both sides in (2.4) by the switching period $T_s$, and rearranging terms we get (2.5):

$$\frac{V_{dclink}}{V_{UC}} = \frac{1}{\underbrace{(1-\lambda)}_{\lambda'}} \tag{2.5}$$

where: $\lambda = t_{on}/T_s$ is the duty cycle for DC model.

The ultracapacitor state (charging or discharging) during the two-quadrant operation (boost mode) can be easily controlled by changing the duty cycle. Assuming a circuit without losses the average inductor current $I_L$ is:

$$I_L = \frac{I_{dclink}}{(1-\lambda)} \tag{2.6}$$

where: $I_{dclink}$ is average DC-link current.

In the Buck mode, if the converter works in continuous-conduction operation the duty cycle is (appendix A.1):

$$\lambda = \frac{V_{UC}}{V_{dclink}} \tag{2.7}$$

Similarly, the current $I_L$ is:

$$I_L = \frac{I_{dclink}}{\lambda} \tag{2.8}$$

The value of $L$ to design the converter is based in the equation (appendix A.1) at the boundary condition. Thus $L$ is:

$$L_{\min} = \frac{1}{2}\frac{\left(V_{dclink} - V_{UCf}\right)V_{UCf}T_s}{I_{UCmax}V_{dclink}} \tag{2.9}$$

Therefore, if $L$ calculated in (2.9) is used, the converter will operate at the edge of continuous mode. Otherwise, the conduction will be discontinuous. For this reason, the value of the inductor should be bigger or equal than the value found in (2.9) [51].

### 2.3.1 Bidirectional DC-DC converter components design

The converter was designed and tested to deliver up to 4kW. According to this power rate, the Bidirectional DC-DC converter components were selected and assembled.

- Inductor design

To design the inductor it was considered that the application requires 4kW of power, a constant switching frequency of 15 kHz, a DC-link voltage of 500V and the ultracapacitor voltage operating with a wide range from 140V to 80V, hence these conditions define the inductor $L_{\min}$ from the equation (2.9).

$$L_{\min} = \frac{1}{2}\frac{\left(V_{dclink} - V_{UCf}\right)V_{UCf}T_s}{I_{UCmax}V_{dclink}} \simeq 0.045mH \tag{2.10}$$

The inductor must be bigger than the value determined in (2.10) to work in continuous-conduction operation mode, since the use of the above calculated value would result in a current ripple of 100% (boundary condition). In order to keep a low current ripple and avoid the overheating of the ultracapacitor bank, the final assembled inductor has 0.82mH (see equation A.5). The final inductor has 36 turns of two parallels Litz wire with section area of 4.8cm² to avoid the skin effect and a N27 ferrite core from *EPCOS* (PM114/93) [52] with 3.8mm of air-gap.

- DC-link capacitor design

From the expression (2.5), the duty cycle for the worst case (minimum ultracapacitor terminal voltage) is:

$$\lambda = 1 - \frac{V_{UCf}}{V_{dclink}} = 0.84 \tag{2.11}$$

In order to assure a high level of energy, it is adopted a DC-link voltage ripple of $\Delta V_{dclink}$=0.5%. Therefore, the minimum DC-link capacitor $C_{dclink}$ is given according to equation (appendix A.9):

$$C_{dclink} = \frac{I_{dclink}\lambda}{\Delta V_{dclink} f_s} \simeq 180\mu F \tag{2.12}$$

The designed DC-DC board has two electrolytic capacitors of 680µF/400V from *EPCOS* (B43511) with a equivalent series resistance of 190mΩ [53] connected in series as DC-link. In total, the equivalent DC-link capacitance is 680µF due to two series DC-link capacitors from the inverter board which are connected in parallel with the DC-DC board.

## 2.4. Basic operation mode of the system

The ultracapacitor bank cannot be employed alone as the system energy storage due to its low-energy density. Hybridizing them (ultracapacitor + contactless energy transmission) together we can take the advantage of both sources increasing the efficiency of the system. The output from the bidirectional DC-DC converter and the contactless energy transmission are connected in parallel at the DC-link. Therefore, the operation of the system can be divided into five basic distinct operation regimes. Figure 2.12 shows these basic operating modes.

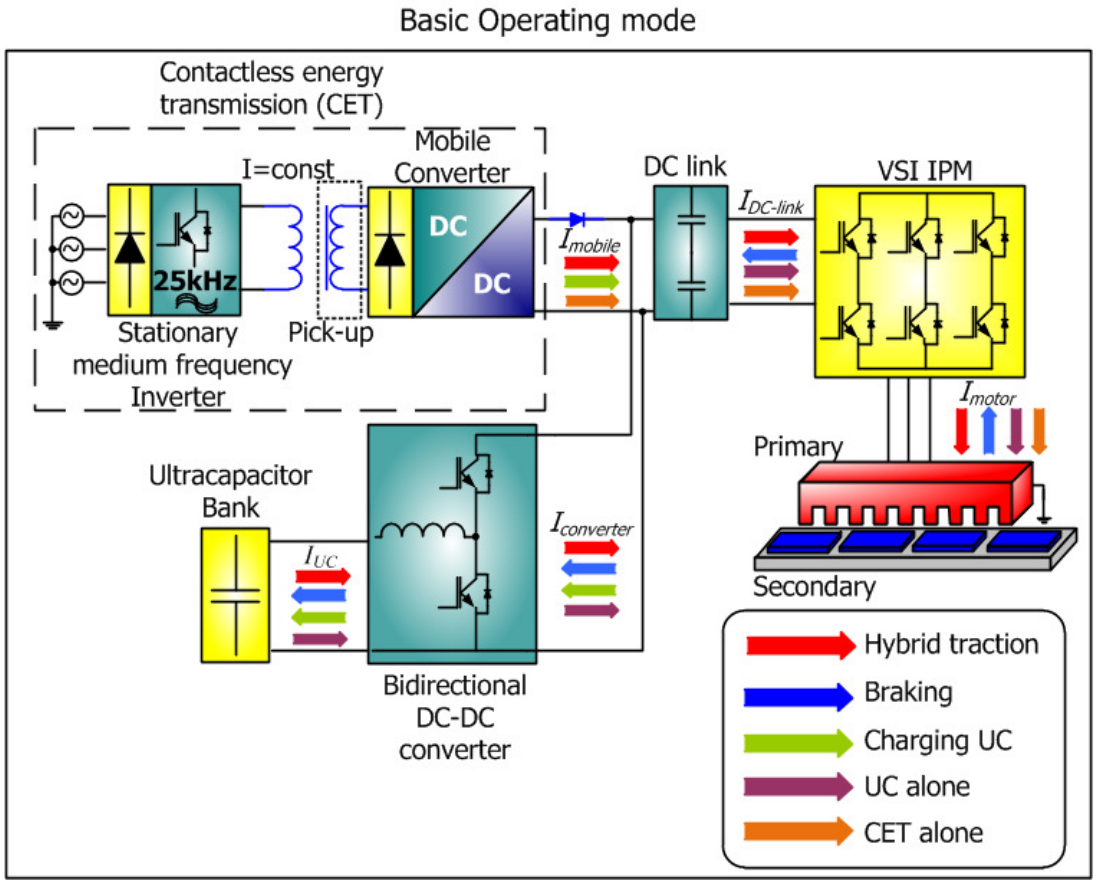


Figure 2.12: Basic Operating modes of the bidirectional DC-DC converter.

Figure 2.12 shows that the contactless energy transmission system is used to charge the ultracapacitor bank and to supply the active vehicle. The basic modes described in Figure 2.12 are explained as follows:

- Ultracapacitor bank stand-alone mode

  The ultracapacitor is able to feed alone the linear motor, however if this mode is utilized the ultracapacitor would be quickly discharged, disabling the capability to supply the required peak power. Therefore, the ultracapacitor alone can be used to propel the vehicle for a short time only. One example of this mode is in case of power outage.
- Hybrid traction mode

  Hybrid traction mode is used when the active vehicle is in acceleration or steady state. If the total required thrust power becomes greater than the power that the contactless energy transmission can deliver, the ultracapacitor provides peak power to the linear motor. So, the total power is shared between both systems and several vehicles can be started at the same time. Another advantage of the hybrid traction is that it can reduce the size and cost of the contactless power system, but still needs further detailed investigations.
- Contactless energy transmission stand-alone mode

  The contactless energy transmission stand-alone mode is used, when it is capable to produce sufficient power to meet the demanded power.
- Charging mode

  The mode of the ultracapacitor charging from contactless energy transmission system is used when the ultracapacitor voltage is below 80 V, in order to maintain the high energy level for power peak operation.
- Braking mode

  During deceleration (regenerative braking) the generated braking energy is recovered, charging the ultracapacitor.

## 2.5. Control strategy

A control strategy is required, to regulate peak power capability of the ultracapacitor, due to its limited energy capacity. The variables, such as ultracapacitor voltage and DC-link voltage, are used in the control strategy.

The energy stored in one ultracapacitor is proportional to the square of its terminal voltage and this value gives a good indication of the remaining charge which is controlled by the pulse-width modulation (PWM) switching applied to the bidirectional DC-DC converter.

It was assumed that the ultracapacitor will supply energy to the system (feeding the linear motor) only when the output voltage of the mobile converter is lower than an operating point. Figure 2.13 shows the mobile converter voltage output for different levels of output current ($I_{mobile}$). In Figure 2.13, it is shown the operating point where the bidirectional DC-DC converter is activated. From this point and beyond, the system works in the hybrid traction mode. In case of braking mode, the ultracapacitor will absorb the energy when the DC-link voltage rises more than 5% ($V_{dclink}$=525V) of the operating point value.

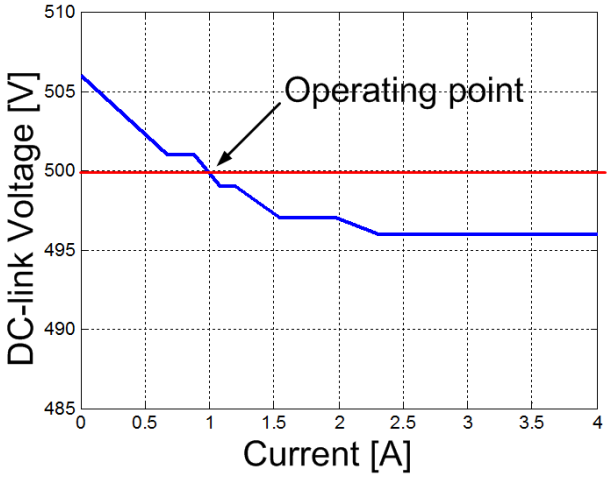


Figure 2.13: Mobile converter voltage output for different levels of output current ($I_{mobile}$).

The bidirectional DC-DC converter control is based on a TMS320F2812 Digital Signal Processor from *Texas Instruments*, which executes an algorithm based on the block diagram depicted in Figure 2.14. The A/D converter module from the DSP acquires parameters such as: ultracapacitor terminal voltage, DC-link voltage and inductor current (see Figure 2.14). The output of the current PI controllers (DC-link voltage control: $V_{dclink}^{*}$ Ultracapacitor current control: $V_{UC}^{*}$) are used to feed the modulator block, that generates two complementary PWM signals. Finally, the two PWM signals are delivered to a IGBT's driver. To generate these signals, a PWM module included in the DSP is used. All the operations depicted in Figure 2.14 have to be controlled by the DSP, which discriminates and takes the suitable decisions for each situation.

The discriminator block defines when the bidirectional DC-DC converter works under Buck mode, two-quadrant operation mode, or it is turned OFF. It has as inputs three variables: the actual ultracapacitor voltage ($V_{dclink}$), the actual DC-link voltage ($V_{UC}$) and a variable called *Flag*. The *Flag* indicates when the ultracapacitor should be charged (*Flag*=1). The *Flag* locks the converter for buck operation until the ultracapacitor be fully charged. After the ultracapacitor be fully charged ($V_{UC}$≥140V) the *Flag* is changed to zero (*Flag*=0), enabling the two-quadrant operation.

The control strategy for *Flag*=0 and charged ultracapacitor ($V_{UC}$≥80V) is described as follows:

- Under low DC-link voltage condition ($V_{dclink}$ <500V)

  If the DC-link voltage is lower than 500V, then it starts the two-quadrant operation to feed the motor.

- Under high DC-link voltage condition ($V_{dclink}$ >525V)

  If the DC-link voltage is higher than 525V, it tests first if the ultracapacitor voltage is below the overvoltage condition ($V_{UC}$≤145V), if yes, it starts the two-quadrant operation absorbing the braking energy. In case of overvoltage condition, the converter is turned OFF.

- DC-link voltage between ($500V<V_{dclink}<525V$)

  If the DC-link voltage is $500V<V_{dclink}<525V$, only the contactless energy transmission will supply the system, thus the bidirectional DC-DC converter is turned OFF.

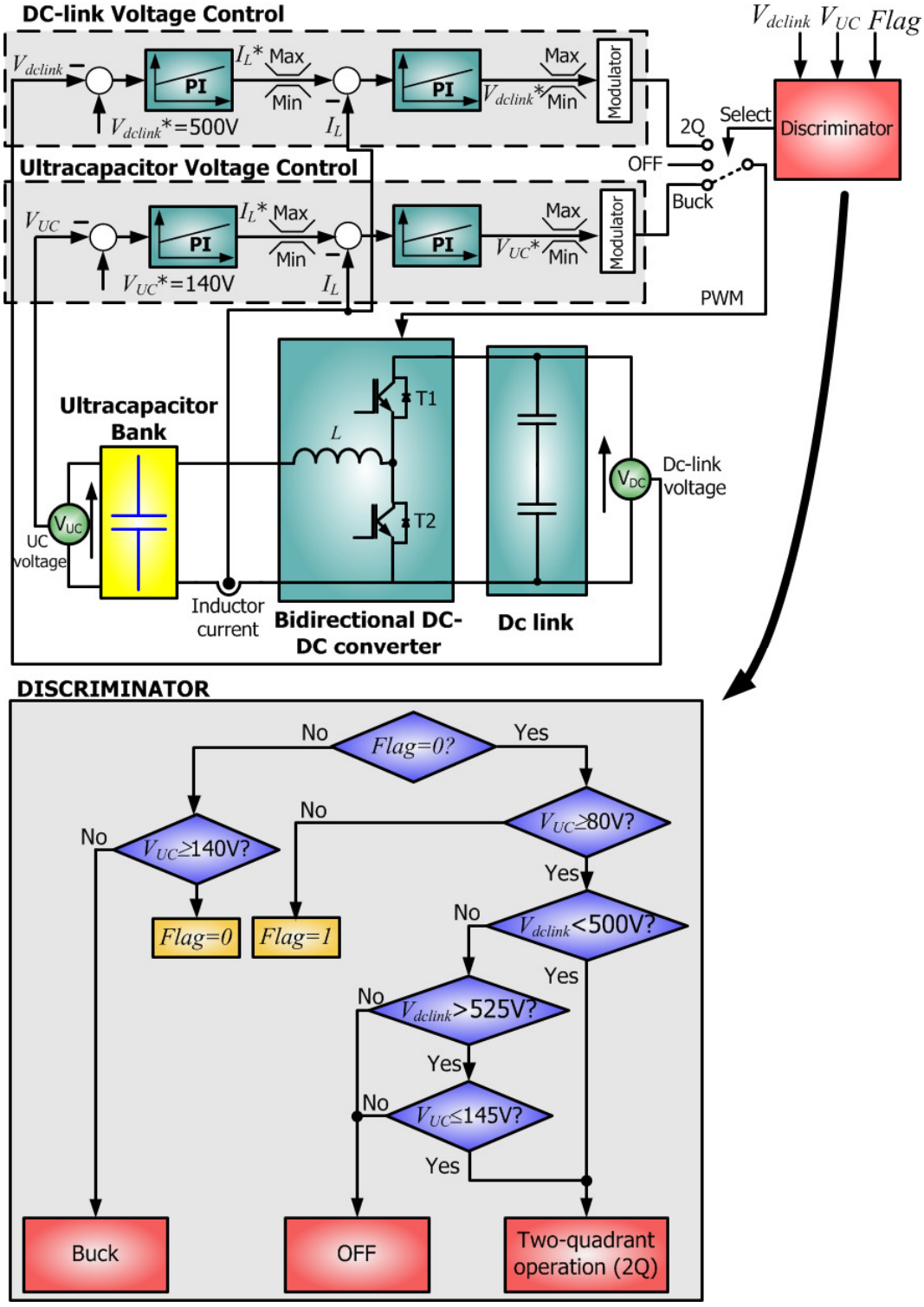


Figure 2.14: Bidirectional DC-DC converter software block diagram.

### 2.5.1 Average current-mode control design

The cascade control structure for each converter depicted in the block diagram (Figure 2.15) is a classical superimposed method of average current-mode control loop to control a DC converter, since a good performance in single loop (peak current-mode control) control is very difficult to achieve [54][55]. The loops can be tuned step by step, limiting the reference values for the control loop. The controllers were discretized by using the Tustin linear transformation (see equation 2.13), with a sampling time two times bigger than the switching frequency ($T_s$=15 kHz), thus $T_{sample}$≈33.3 μs.

$$s = \frac{2\left(1-z^{-1}\right)}{T_{sample}\left(1+z^{-1}\right)} \tag{2.13}$$

### 2.5.2 Buck mode

The small signal model transfer functions for the Buck operation are described by the equations (appendix A.41, A.45 and A.46). Figure 2.15 shows a simplified inner current control loop using a PI controller for the Buck operation. There, the PI controller adjusts the duty cycle ($\lambda$) and the inductor current ($I_L$), to cancel the error between the reference value and the acquired value. The control time delay is modeled as a first-order lag element with a time constant $T_D$=2$T_{sample}$=$T_s$ [56].

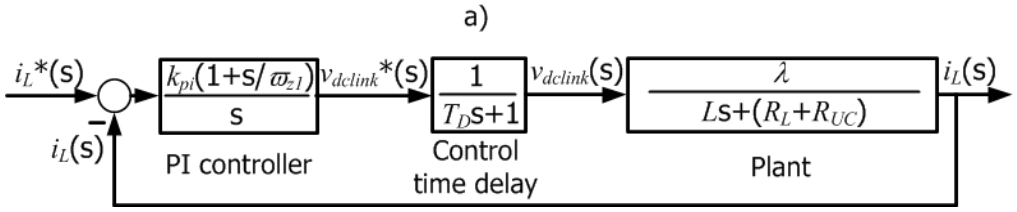


Figure 2.15: Simplified inner current control loop for Buck operation.

The open-loop transfer function for the system depicted above is:

$$F_o(s) = \frac{k_{pi}(1+ s/\varpi_{z1})}{s} \frac{1}{T_D s+1} \frac{\lambda}{Ls+\left(R_L+R_{UC}\right)} \tag{2.14}$$

where: $R_L$ is the inductor resistance (103mΩ),

$R_{UC}$ is equivalent series resistance of ultracapacitor bank (190mΩ).

The Bode diagram of the open-loop transfer function $F_o(s)$ is shown in Figure 2.16. The pole placement of the PI current compensator was designed using the criteria from the references [57][58]. Then, the zero $\varpi_{z1}$ is set above the pole of the plant to increase the phase margin around the zero crossover frequency, an integrator is added to get a high gain and the gain $k_{pi}$ is set to the zero crossover frequency be one decade below the switching frequency (1.5kHz).

The closed-loop current transfer function is:

$$F_w(s) = \frac{1}{1+\frac{1}{F_o(s)}} \tag{2.15}$$

In a multi-loop control system, the inner loop must have a bigger zero crossover frequency than the outer loop, to get the benefits of this kind of control [54][55][58]. The simplified outer voltage control loop block diagram using the output impedance (equation A.46) is shown in Figure 2.17.

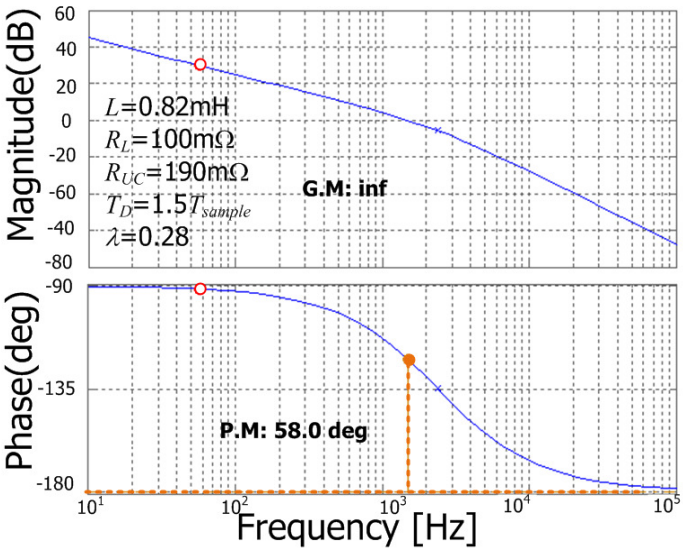


Figure 2.16: Bode diagram of the open-loop inner current control loop for Buck operation.

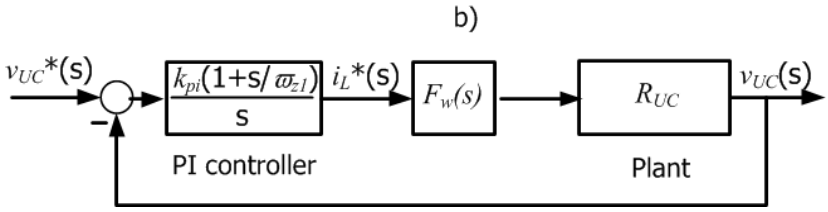


Figure 2.17: Simplified outer voltage control loop for Buck operation.

The Bode diagram of the open-loop transfer function for the simplified outer voltage control is show in Figure 2.18. For the PI controller pole placement, zero $\varpi_{z1}$ is set above the complex poles, and the gain $k_{pi}$ is set to a zero crossover frequency slower than the inner current control loop (15Hz).

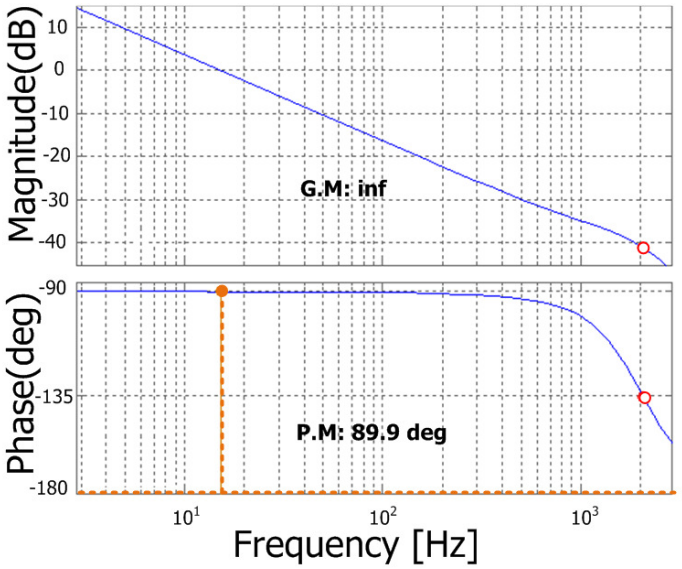


Figure 2.18: Bode diagram of the open-loop outer voltage control loop for Buck operation.

### 2.5.3 Two-quadrant operation (Boost mode)

The PI controller parameters for the Boost operation are tuned similar to the Buck controller. Roughly, there is no difference between both controllers, as shown in Figure 2.19a and 2.19b. The Bode diagrams of the inner current and the outer voltage control loops for the two-quadrant operation (Boost mode) are shown in Figures 2.20a and 2.20b.

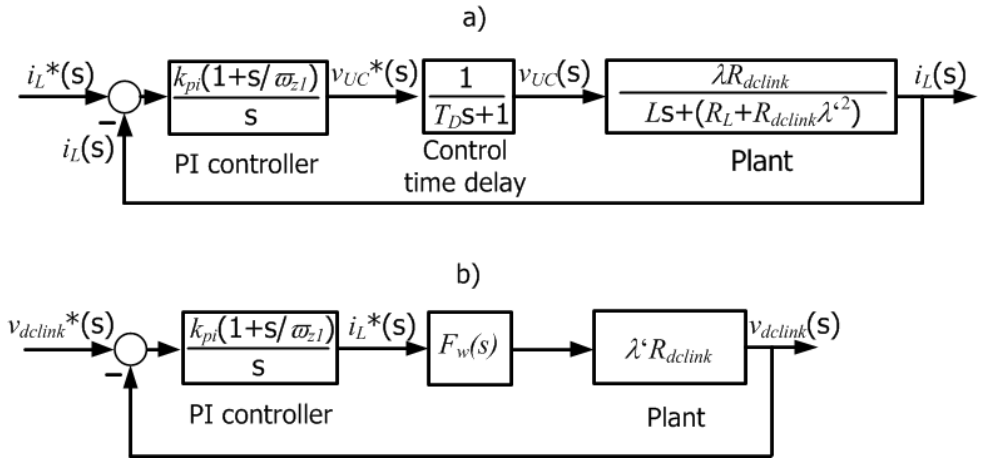


Figure 2.19: Simplified a) inner current b) outer voltage control loops for two-quadrant operation (Boost mode).

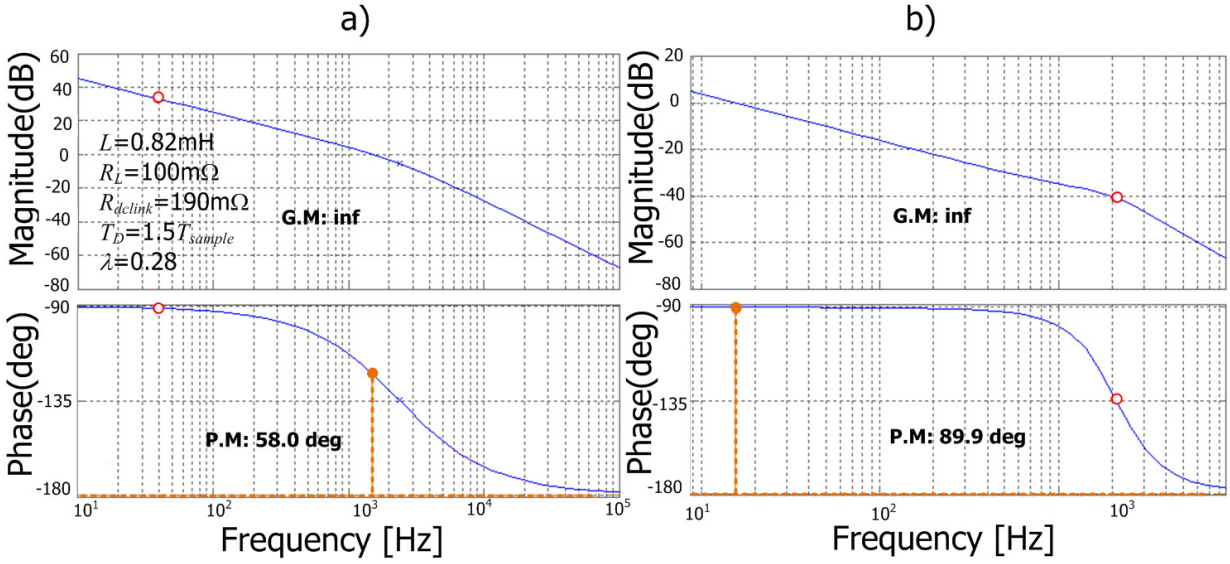


Figure 2.20: Bode diagram of the a) inner current b) outer voltage control loops for the two-quadrant operation (Boost mode).

## 2.6. Bidirectional DC-DC Board and test results

### 2.6.1 Bidirectional DC-DC Board

Figure 2.21 shows the hardware test setup. The bidirectional DC-DC converter prototype consists of a IGBT module (SKM75GB123) with up to 1200V/75A from *Semikron* [59], a inductor

coil, DC-link capacitors, a shared air-cooled heat sink (DC-DC converter + inverter), a dual IGBT driver (SKHI 22 A/B H4) from *Semikron* [60] and a DSP board.

The board has a dimension of 224mmx192mm and can achieve up to 4kW of power with 15 kHz of switching frequency. Three *LEM* hall sensors (2x voltage transducer LV 25-P [61] and 1x current transducer LA-25NP [62]) were used to decouple the measured signals. The output signals were analogically amplified, filtered and connected to the A/D pins of the DSP board. The outputs of the on-board inverter, the mobile DC-DC converter and the bidirectional DC-DC converter are connected in parallel at the high-voltage (500V) side.

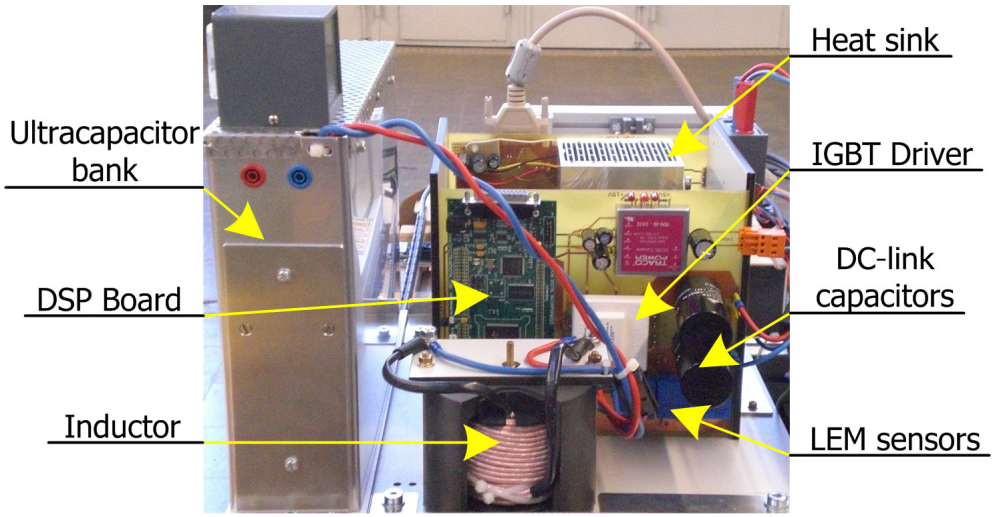


Figure 2.21: Bidirectional DC-DC converter prototype.

The stray inductance between the DC-link and converter may produce voltage overshoot due to the high *di/dt* during the switching. As consequence a snubber circuit should be installed directly at the IGBT module terminals and DC-link terminals avoiding the damage of the device. After several experimental tests using different snubber circuit configurations, one RCD-clamp snubber (see Figure 2.22) appropriated for high current IGBT applications [63] was installed in the IGBT module screws.

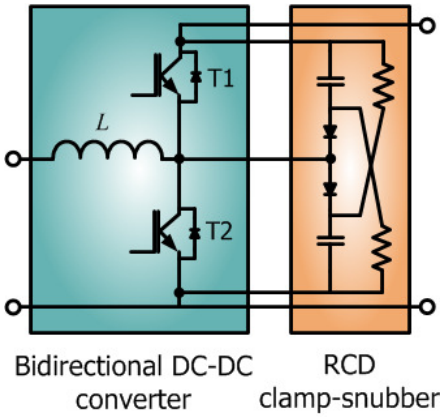


Figure 2.22: RCD clamp-snubber connected to the IGBT module screws.

### 2.6.2 Test results

With the hardware prototype mentioned above and both energy sources connected, the bidirectional current flow control strategy will be presented in this subsection. The experimental tests consist of Buck mode operation, vehicle travelling on the stationary magnets and vehicle travelling on the induction rail.

#### 2.6.2.1 Converter charging the ultracapacitor (Buck mode)

The next oscillogram shows the results when the bidirectional DC-DC converter works in charging mode. This experimental test allows to evaluate the ultracapacitor charging time. The Figure 2.23 displays the ultracapacitor terminal voltage and current.

The experiment results showed that the charging time is around 80 seconds with a limited maximum current of $I_{UC}$=5A, since the output current of the mobile converter was limited in 1A. The zoom-in depicted in Figure 2.23 shows the effect of the ESR of the ultracapacitor bank during the charge, so that the measured terminal voltage is a little less when the charging mode is stopped.

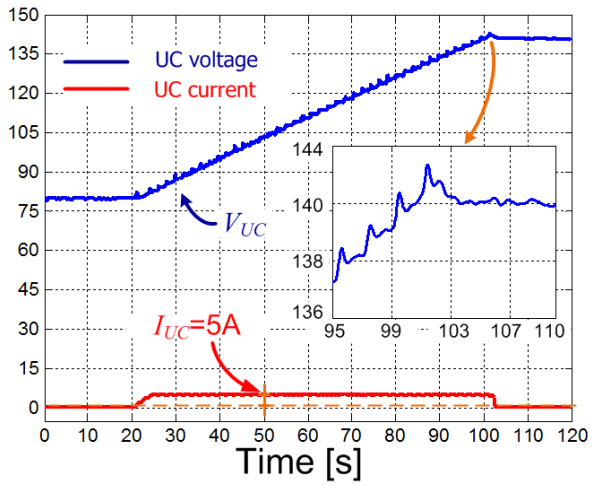


Figure 2.23: Test result of the bidirectional DC-DC converter charging the ultracapacitor bank.

#### 2.6.2.2 Active vehicle travelling on the stationary magnets

At first, the test was carried out with the active vehicle travelling on the stationary magnets (synchronous operation). In this experimental test, the vehicle was controlled to move forward 50cm in 1.0 second, to stop and return to the original position. The experimental test shows the current and voltage waveforms variations during the acceleration and the regenerative braking. The results are depicted from Figure 2.24a to Figure 2.24c, displaying the (a) reference and measured position, (b) ultracapacitor voltage and current and (c) Mobile converter current and DC-link voltage.

During the acceleration, the mobile converter feeds (positive current) the moving primary, as shown in Figure 2.24c. Afterwards, the active vehicle is smoothly stopped (see Figure 2.24a), and then the ultracapacitor is charged by the braking energy (negative current). This regenerative braking process takes 0.31 seconds and the current $I_{UC}$ goes from 0 to −12.9 A.

The voltage rise was around 0.45 V during the driving interval, as depicted in Figure 2.24b. The DC-link voltage was kept constant at its rated value during the drive cycle. The test results show

very good agreement, which means that the mobile converter delivered the peak energy and the ultracapacitor absorbed energy as expected.

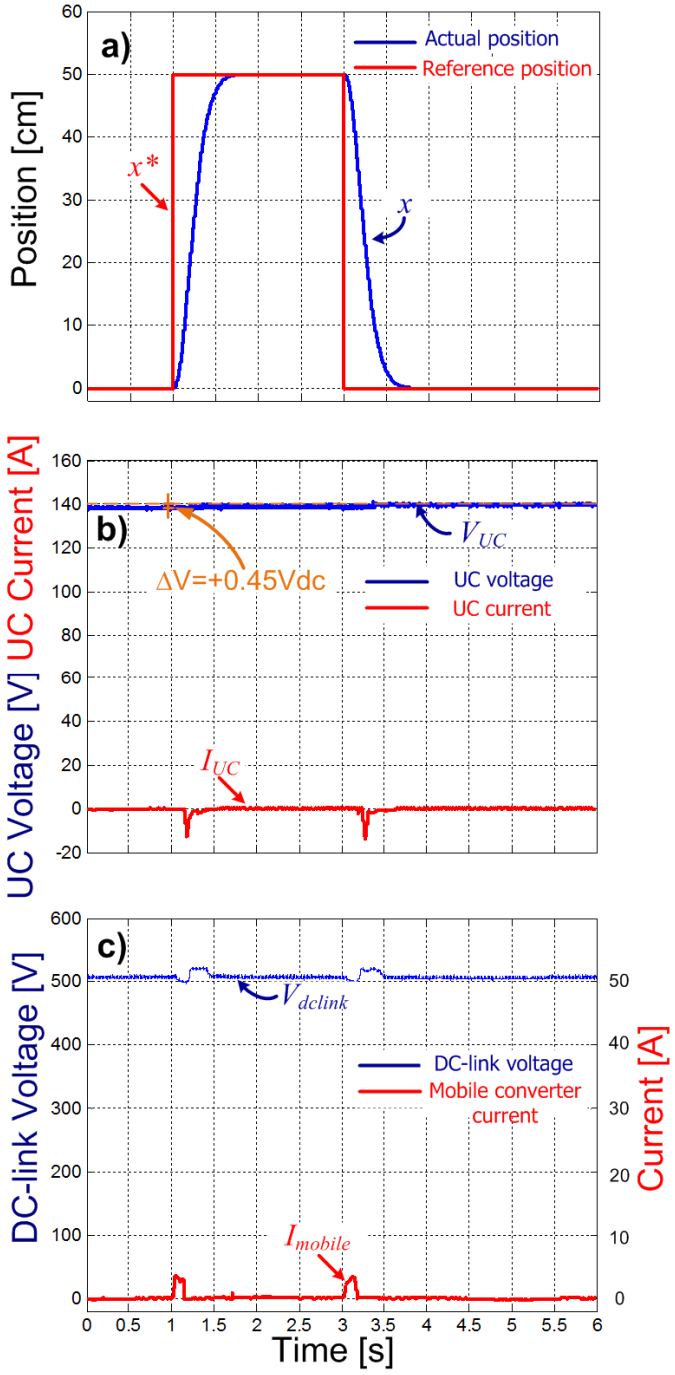


Figure 2.24: Test results for the PMLSM: a) reference and measured position; b) ultracapacitor voltage and current; c) Mobile converter current and DC-link voltage.

### 2.6.2.3 Active vehicle travelling on the induction rail

For the active vehicle travelling on the induction rail the same position conditions from the subsection 2.6.2.2 were carried out. This experimental test shows the bidirectional DC-DC converter

behavior for a load with high power demand. The waveforms results are illustrated in Figure 2.25a to Figure 2.25c, displaying the (a) reference and measured position, (b) ultracapacitor voltage and current and (c) mobile converter current and DC-link voltage.

In this test result, the demanded current was shared by the ultracapacitor bank and the mobile converter. Figure 2.25b shows that the ultracapacitor discharges when the vehicle is moving. Also it

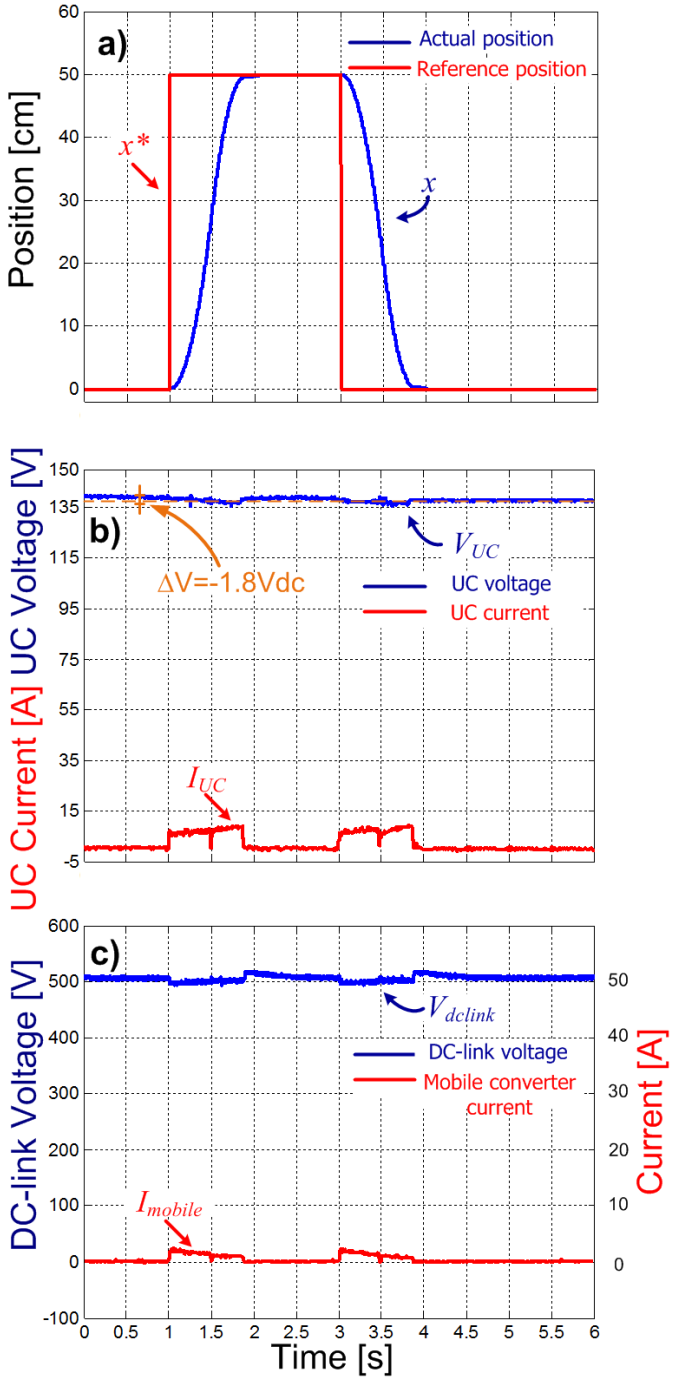


Figure 2.25: Test results for LIM: a) reference and measured position; b) ultracapacitor voltage and current; c) mobile converter current and DC-link voltage.

can be seen that the output current of the mobile converter after the initial peak was kept at 1A and the output voltage was fixed at 500V. As a rule, the energy efficiency of the linear induction motor is low due to the large air-gap. Therefore, the generated braking energy is small in comparison with the losses, thus both sources deliver even more energy to stop the active vehicle. The ultracapacitor voltage $V_{UC}$ drop was around 1.8V at the end of the drive cycle, due to the high power required by the linear motor. Moreover, at the end of the braking period a small elevation above the DC-link voltage level can be observed in the waveform, as shown in Figure 2.25c. In summary, the use of on-board energy storage in order to supply the vehicles is very practicable.

# 3. Experimental Setup

The laboratory prototype of a short primary linear drive with an on-board energy storage device was constructed for experiments, based on the proposed system presented in chapter 1. The system employs one track divided in two sections and one active vehicle, which represents a material handling system with two sections: transporting and processing. The control unit and the ultracapacitor energy storage system are on-board of the vehicle. The experimental setup is an integration of commercial equipments and boards developed at the laboratory, and it will be presented and displayed in the following.

## 3.1. Linear motor

The chosen linear motor is a convection-cooled synchronous motor from *Baumüller*. The primary core of type LSE10G1008 was mounted under the active vehicle as illustrated in Figure 3.1. The primary comprises of a laminated iron stack and a distributed three-phase winding. The primary is also fully laminated with carbon fiber allowing the motor to reach high stiffness and good heat dissipation [64]. Table 3.1 shows the construction dimensions and information of the primary core.

Table 3.1 Primary core dimensions and information [64].

| | | | |
|---|---|---|---|
| Dimensions | 326x105x42mm | Number of poles ($2p$) | 8 |
| Weight | 7.8kg | Pole pitch ($\tau$) | 36mm |
| Phase Resistance ($R_1$) | 3.9Ω | Motor voltage 3~ | 380V |
| Maximum Synchronous speed ($v_{1max}$) | 3.6m/s | Cooling type | Natural cooling |

The secondary part within the processing section employs skewed permanent magnet segments of type LSM10. The segment has a galvanized back iron with 8mm thickness, and the array of four magnets pieces with 4mm thickness bonded on the surface of the back iron. Although, the LSM10-1015 segment has only four magnets pieces, the long passive track was arranged using eleven segments one next to another, resulting in a secondary track with around 1.6 meters and 44 poles. For the transporting section, the secondary part is an induction rail. The induction rail has two layers: one copper layer and one back iron layer, and it was constructed screwing both sheets together in the edge. Finally, both secondaries were installed between the guidance profiles.

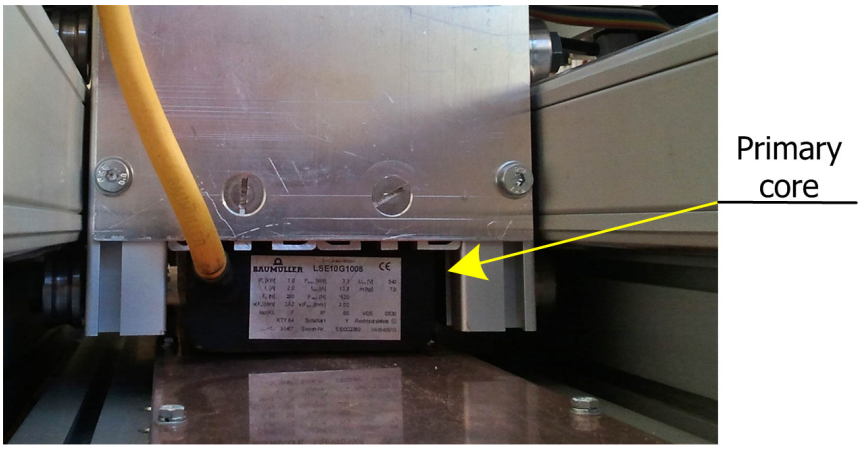


Figure 3.1: Primary core mounted under the active vehicle.

Figure 3.2 displays the border between the transporting section (induction rail) and the processing section (stationary magnets). At the transition area, the value of reluctance force of the magnets becomes very high when the vehicle is leaving the permanent magnet section and entering the induction rail section.


Figure 3.2: Border between the transporting section (induction rail) and the processing section (stationary magnets).

Considering that we have different sections, the linear motor can operate as synchronous or as induction machine. Therefore, the linear motor parameters are splitted for induction operation and for synchronous operation as shown in Table 3.2. The datasheet parameters [64] are not valid in the designed experimental setup, due to the large air-gap ($\gamma_s$>0.6mm) at the processing section. Thereby, the parameters for synchronous and induction operations were experimentally acquired.

## 3.2. Mechanical structure

The mechanical structure was built using a commercial aluminum profile system from *MiniTec*. According to the proposed system of a material handling system, the track was divided in two sections. The track has 3.3 meters, and each secondary section has the length shown in Table 3.2.

Table 3.2 Motor parameters for different sections.

| | | | |
|---|---|---|---|
| **Synchronous operation** | | | |
| Nominal current ($I_{sn}$) | 3.0 A | Force constant ($k_{sf}$) | 83.05N/A |
| Peak current ($I_{smax}$) | 8.0A | Air-gap ($\gamma_s$) | 2mm |
| Nominal thrust force ($F_{sn}$) | 250N | Peak thrust force ($F_{smax}$) | 664N |
| Phase inductance ($L_{s1}$) | 31.8mH | Secondary length ($l_s$) | 1584mm |
| **Induction operation** | | | |
| Nominal current ($I_{in}$) | 4.18A | Force constant ($k_{if}$) | 44.24N/A |
| Secondary Resistance ($R_2$) | 16.94Ω | Air-gap ($\gamma_i$) | 1mm |
| Primary inductance ($L_{i1}$) | 99mH | Magnetizing self-inductance ($M$) | 67mH |
| Secondary inductance ($L_{i2}$) | 81mH | Secondary length ($l_i$) | 1584mm |

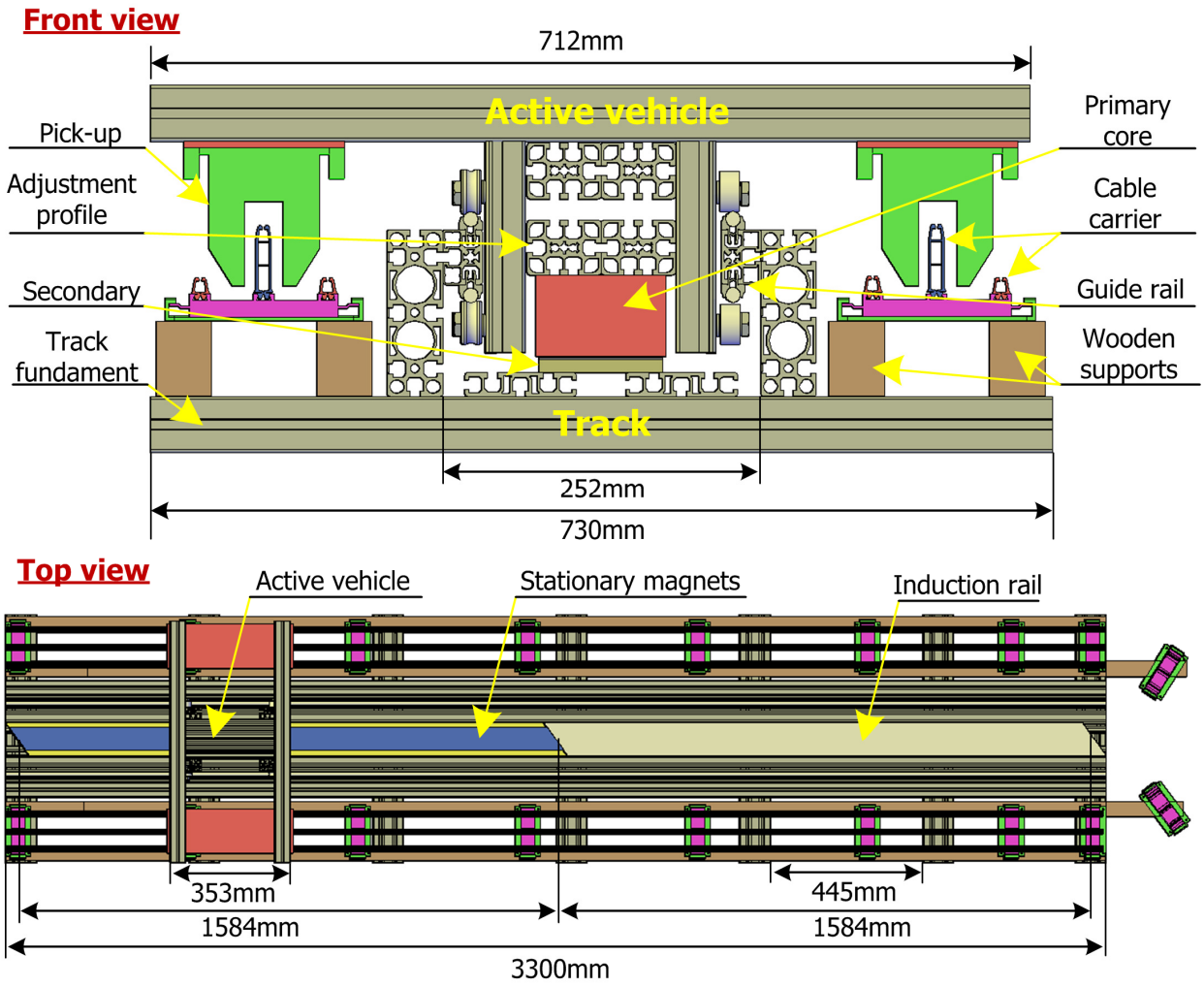


Figure 3.3: Mechanical construction of the active vehicle and the track.

The active vehicle moves along a linear guide rail, thus the air-gap is kept constant between the vehicle and the track. The vehicle has a four wheels system, which allows it to move only in the horizontal axis. The active vehicle was design thinking to use less material, aiming to be as light as possible and to provide free space for the natural cooling. All the on-board components were equally distributed to keep the balance, so that each pick-up was fixed at the two extremity of the vehicle, as shown in Figure 3.3. The adjustment profile is used to regulate the air-gap length.

To achieve the electromagnetic best coupling, the maximum distance between the line cable and the pick must be 19mm [65]. Therefore, two wooden supports are installed below the cable profile carrier as shown the Figure 3.3. Furthermore, it is recommended a free space within a radius of 5cm around the line cable, so that the wooden supports guarantee also the free space using no ferromagnetic or electrically conductive material components, avoiding induced current at the aluminium profile. The Table 3.2 displays two different lengths for the air-gap. The air-gap at the permanent magnet side was increased in comparison with the recommended by the datasheet, to reduce the very high attractive force, which could slowly slide down the adjustment profile. At the induction rail side, the attractive force is smaller. Moreover, the air-gap of a linear induction motor must be adjusted as small as possible, to achieve a better efficiency [2][3]. The parameters of the mechanical structure and the implemented experimental setup are shown in Table 3.3 and Figure 3.4.

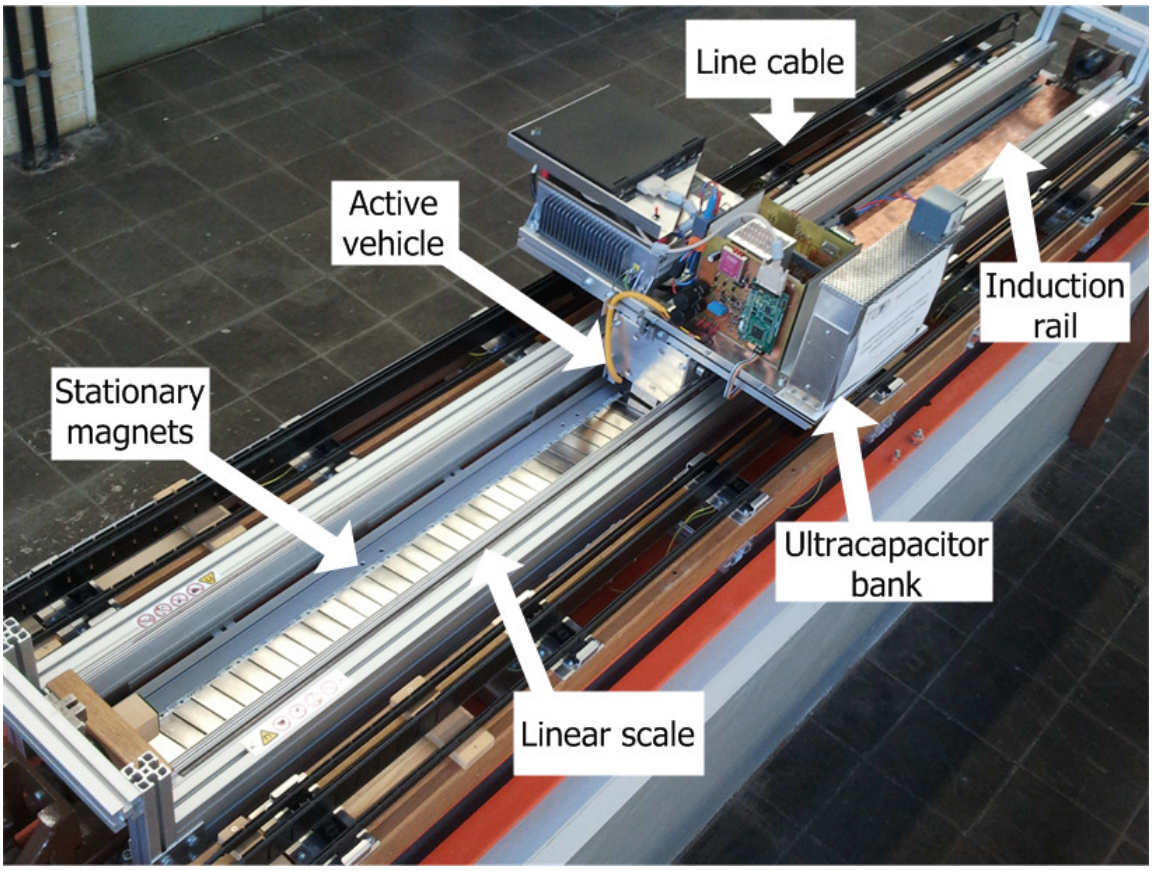


Figure 3.4: Implemented experimental setup.

Table 3.3 Mechanical structure parameters.

| | | | |
|---|---|---|---|
| Track length | 3300mm | Vehicle length | 353mm |
| Track width | 730mm | Vehicle width | 712mm |
| Active vehicle weight (vehicle + on-board devices) | 53.7kg | Vehicle weight (mechanical structure) | 9.8kg |

## 3.3. Position sensor

At the station where the materials are processed a high accuracy (few µm) is demanded. It was used a linear measuring system (ELS 29-nl-SST03-01) composed by a linear magnetic scale with fixed pole pitch (1mm) and an anisotropic magneto-resistive incremental encoder from *Sensitec*. As discussed in chapter 1 to reduce the costs, one position sensor with less accuracy or sensorless estimation could be applied for the motion control, when the vehicle is travelling outside the processing station. However, in this experimental setup a 3m-long linear magnetic scale was installed along the whole guidance profile.

The incremental encoder was attached at the active vehicle, to inform the actual position for orientation of the rotating *AB*- or *dq*- reference frame and to calculate the real speed value. With a resolution of 200 increments per mm (5µm), the position sensor produces an electrical output signal of two sequences of pulses (A/B) which have a variable frequency and are phase shifted by 90° with one another. These signals are transmitted over RS485 lines to the inverter board. At the board, the signals are connected to the quadrature-encoder pulse (QEP) pins of the DSP, which decodes these signals. Figure 3.5 shows the installation of the position sensor module at the active vehicle with a distance between the sensor head and the scale surface of 0.5mm.

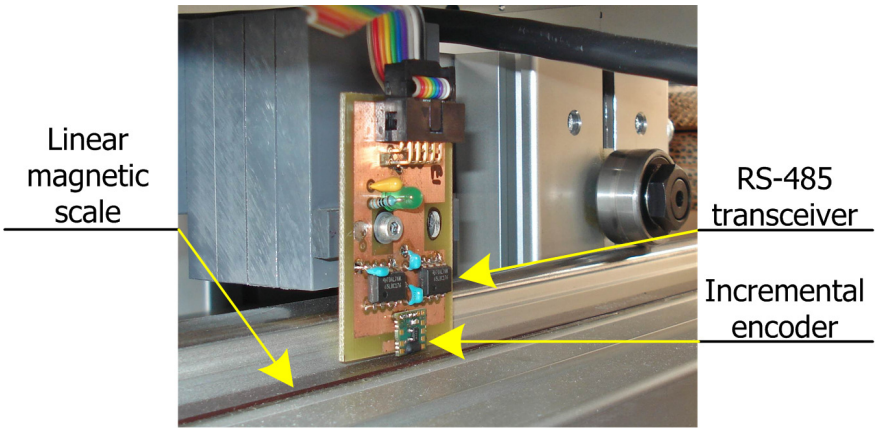


Figure 3.5: Incremental encoder attached at the active vehicle.

The given sensor module has a low cost and has a good accuracy, and is a good solution for linear motor applications using active vehicles on passive track.

## 3.4. Force sensor

The force parameters described in Table 3.2 were experimentally acquired for the synchronous operation and induction operation. The force measurement was carried out by using a compact force sensor KD40s from *ME-Meßsysteme* [66]. The sensor was constructed to cover a range of ±1000N with 0.1% of accuracy. The output of the force sensor is an analog signal that was amplified by a precise bridge amplifier GSV-1A from the same company [67]. Moreover, the amplified voltage signal (±10V and 10mV→1N) was read by using a standard multimeter. The force sensor was fixed between the vehicle and the aluminium profile (by an adjustable rod) in such way that the vehicle remained at stand still during the experimental tests. The adjustable rod allows us to make the measurement for different vehicle positions with a step of 2mm and a maximum range of 140mm. Figure 3.6 shows the experimental setup prepared for a standstill force test.

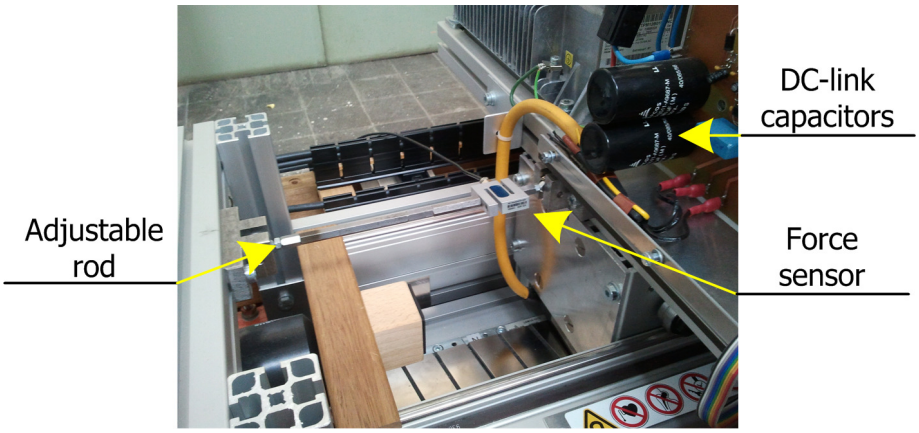


Figure 3.6: Experimental setup with the force sensor.

## 3.5. Power supply

For the topology with short primary linear motor, explained in chapter 2, the power source to feed one active vehicle is composed by one contactless system together with the ultracapacitor energy storage system. As a rule, supposing a real industrial application with several vehicles, it would be necessary one ultracapacitor storage system and one three-phase inverter on-board of each vehicle. Hence, just one contactless energy system is responsible to supply energy to all the travelling vehicles. The DC 24V supply output of the mobile DC-DC converter is used to supply sensors and auxiliary circuits of the on-board inverter and bidirectional DC-DC converter boards.

The contactless energy system is connected at the three-phase voltage through line-fuses, which protect the system against over current. One main switch is used to turn ON/OFF the stationary inverter. One AC line filter was placed between the stationary inverter and the line-fuses to attenuate the high-frequency electrical noise generated by the fast switching voltages of the stationary inverter. The given contactless energy transmission system can supply a maximum track length of 200m [29]. If a longer track is required, the material handling track can be divided into several sections of 200m, so that each section will be fed by one contactless energy system. The stationary converter was set for a constant current output (60A), as a result of the two connected pick-ups. Figure 3.7 displays the stationary converter and the mobile power supply described above. The

depicted transformer module converts the output voltage from the stationary converter into a constant sinusoidal AC current [29]. The resonating capacitor used to compensate the line inductance is placed within the module.

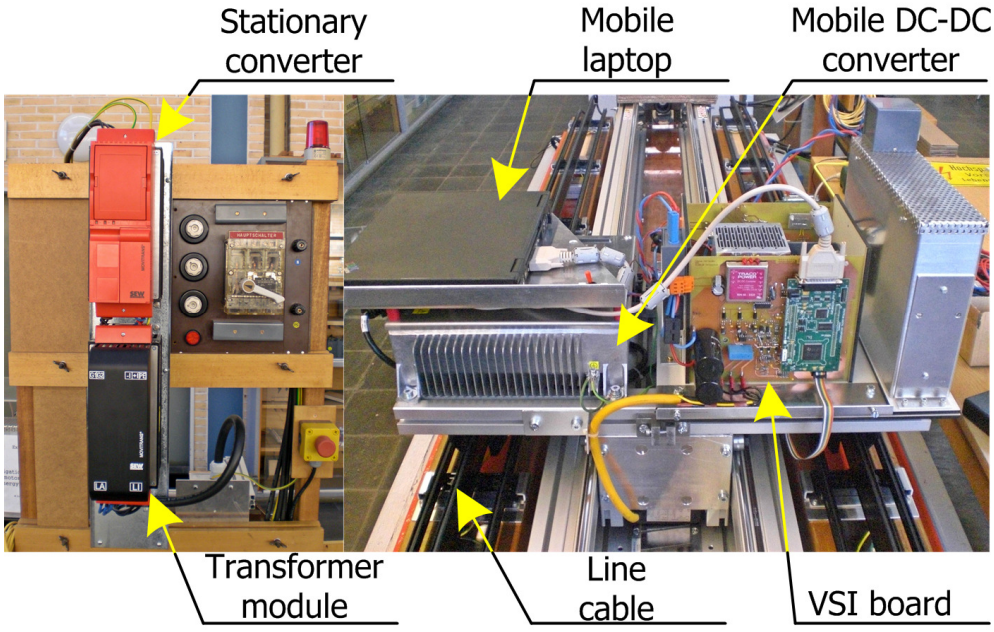


Figure 3.7: Stationary and mobile power supply of the experimental prototype.

## 3.6. On-board voltage source inverter (VSI)

The on-board VSI is implemented by an IPM with a switching frequency of 10 kHz. The VSI board was designed and implemented in the Institute's laboratory. The board has one IPM from *Mitsubishi* [68], current measurement (33mΩ/5W shunt resistors), amplifiers circuits, over-current protection circuits, DC-link capacitors, one electronic DC-DC power supply with ±15V and 5V outputs, RS-485 receivers and one DSP controller board. The shunt resistors for current measurement were placed near to the IGBT emitter legs (NU, NV, NW IPM pins), reducing the effect of its stray inductances [68].

The VSI board can reach a power range of up to 3.7kW. The IPM has integrated six IGBTs with up to 1200V/25A, and it has advantages such as: integrated gate driver circuits, under-voltage protection circuit and over-current fault generator [68]. Hence, it represents a low-cost solution for linear motor drive applications [69].

The over-current detection is based on two analog comparators (to detect positive and negative currents) connected to each inverter leg, as shown in Figure 3.8. In case of an over-current situation, the resistor shunt voltage will exceed the pre-adjusted (±20A→0.66V) threshold voltage value. Afterwards, the analog comparator output will trigger the clock pin of a D flip-flop, changing the voltage level of the Q output pin. The Q output pin feed back to the overvoltage detecting terminal (Cin) of the IPM, thus the IPM will turn off immediately. In the mean time, an active-low fault signal is also generated by the IPM, warning the DSP through the power drive protection interrupt (PDPINT) pin, which will activate the software protection. After an over-current situation, the circuit must be reseted manually. An undesired fault condition due to noise will be suppressed by a

low pass filter with 1.5us time constant connected at the comparator input terminal, as depicted in Figure 3.8. The current output signals coming from the voltage drop across the shunt resistors are analogically amplified, filtered and connected to the ADC pins of the DSP board.

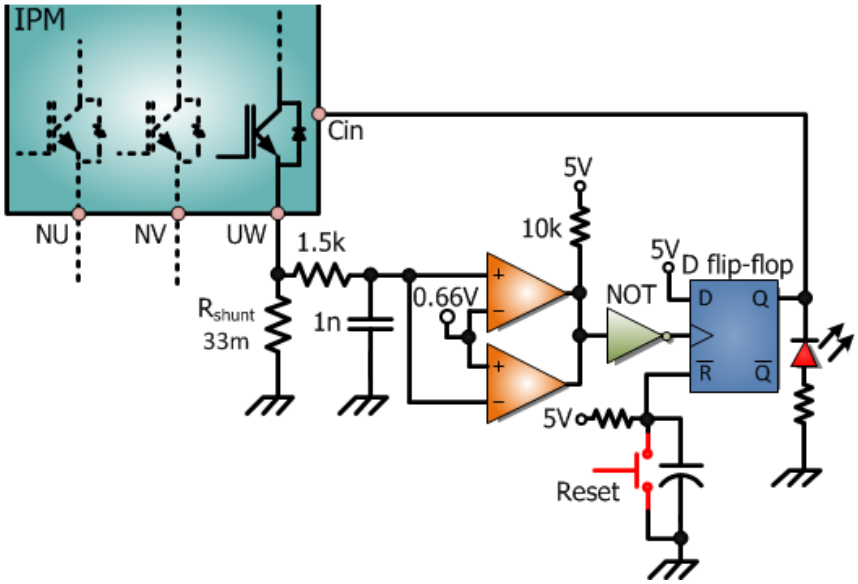


Figure 3.8: Over-current protection circuit for one leg.

Due to the parasitic inductance from the current path (e.g. DC-link connection) a low inductance snubber capacitor (Metalized Polypropylene) was mounted directly on the IPM terminals (positive and negative). This snubber works as a low-pass filter and reduces the high-voltage spikes across the IGBTs [70].

All the board connections were placed as close as possible each to other and the cables were twisted to reduce even more the stray inductance. The DC-link capacitors are two aluminium-electrolytic capacitors in series (see Figure 3.7), and they have the same characteristics as the DC-link capacitors utilized in the bidirectional DC-DC converter board, as discussed in subsection 2.3.1.

The board has the same dimensions of the bidirectional DC-DC converter board (224mmx192mm). The IPM module shares the air-cooled heat sink with the DC-DC converter, as illustrated in Figure 3.7. The heat sink was designed, so that the junction temperature of the IGBTs and anti-parallel diodes from both modules (IPM + DC-DC converter IGBT module) does not reach more than 125°C.

## 3.7. Control unit

The main controller board is based on the DSP TMS320F2812 from *Texas Instrument*, working at 150MHz clock frequency. The given DSP was shipped on a development board (eZDSPF2812) from *Spectrum digital* [71]. This development board provides an easy and fast platform for evaluation. Furthermore, the Input / Output (I/O) pins are distributed in an industrial standard connector. Since the numbers of available physical pins are limited, it is necessary to multiplex the I/O interface pins, as illustrated in Figure 3.9 [72]

The DSP board communicates with a computer via a standard parallel port. The code development was carried out through an application called *Code Composer Studio* (CCS) from *Texas*

*Instrument*. Through the use of CCS and its integrated compiler, programming both in C/C++ code or the native assembly language is supported. The given DSP has a 32-Bit fixed-point arithmetic unit. Some difficulties with the code writing using a fixed-point algorithm were overcome by the use of a virtual floating point engine. Therefore, trigonometric function routines (e.g. $\alpha\beta$- to $dq$-reference frame transformation) could be easily implemented and executed. The development board comprises a JTAG module, which permits the CCS to access the registers of the DSP while in running mode. The JTAG is a debugging interface for embedded systems.

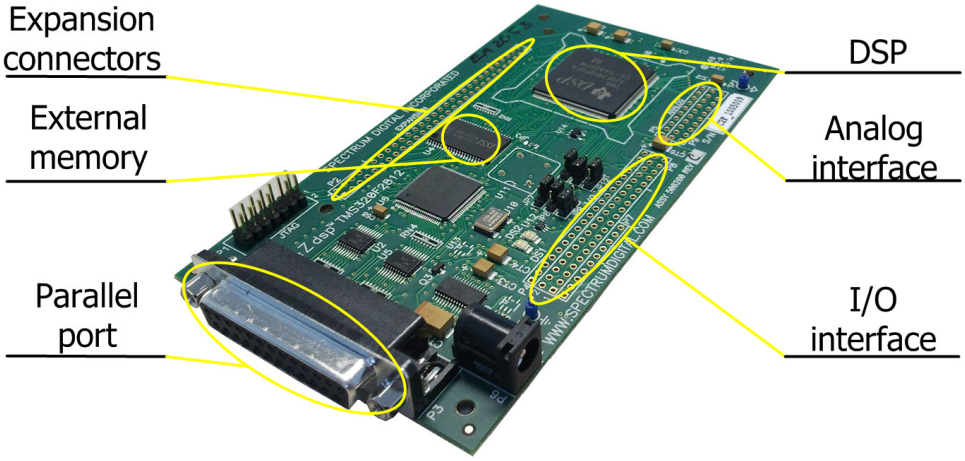


Figure 3.9: Photo of the eZDSPF2812 development board.

There are two identical event manager modules (EVM) on-board the F2812 DSP. The event manager contains the following components:

- Two general-purpose timers.
- Three compare units.
- PWM modules including the dead-time generation.
- Three capture units.
- QEP units.
- Interrupt service logic.

Thus, the EVM is the most important peripheral for a digital motor control. Each EVM is individually programmable and works in parallel [72].

The general-purpose timer is a simply timer with a 16-Bit counter, which may be configured to count up, down, or continuously. Furthermore, it defines an interrupt service routine at a predefined value, i.e. period match, under/overflows and compare interrupt. The general-purpose timer has also a watchdog timer, which monitors software and hardware operations, increasing the reliability of the system. The watchdog generates a system reset in case of CPU disruption.

The DSP has 16 channels for PWM and ADC. Each PWM module contains a pulse pattern generator for symmetric (triangle) and asymmetric (saw-tooth) PWM waveforms generation. The PWM signal is generated by setting a timer to repeat a counting period continuously. It always compares the timer counter value with the compare value, thus if a match occurs the PWM pin output is toggled. The PWM output pin toggles again, if the timer period value is reached.

The ADC channels have a resolution of 12-Bit with a maximum sampling frequency of 25 MHz, which means that the ADC generates a 12-Bit integer number for every conversion. Additionally,

two channels can be simultaneously sampled by a dual sample and hold unit. More DSP characteristics can be found in Table 3.4.

Table 3.4 CPU and DSP development board characteristics

| **TMS320F2812 CPU** | | | |
|---|---|---|---|
| Clock speed | 150MHz | Pipeline level | 8 |
| Input/ Output pins | Up to 56 | Signal levels | [0, 3V] |
| QEP | 2-channels | Timers | 3, 32-bit + 1 watchdog |
| On-chip Memory | 128k words on chip Flash | PWM | 16-channels |
| | 18 K words on chip RAM | | |
| ADC | 16-channels, 12-Bit resolution | ADC sample rate | 25MHz |
| SPI | 1 | UART | 2 |
| CAN | 1 | CAP | 6-channels |
| **eZDSPF2812 board** | | | |
| Expansion connectors | 2 | External Memory | 64K words on-board RAM |
| JTAG interface | 1 | Voltage supply | 5V |

At last, the DSP is responsible to generate the space vector (SV) modulation, to compensate the required IPM dead-time (3.3μs), to control the position and speed and to control the required current for the linear motor. So, the proposed material handling system uses two on-board DSPs controllers (VSI and bidirectional DC-DC converter). For a real industrial manufacturing application, only one DSP would be a suitable solution. It can control both the motor side inverter (VSI) and the bidirectional DC/DC converter, since the DSP has 16 PWM and ADC channels. The on-board VSI with all the above mentioned components is displayed in Figure 3.7.

## 3.8. Data transfer

As it can be seen in Figure 3.7, all the basic components are on-board the active vehicle. Therefore, the experimental prototype must be monitored and operated by sending the information without contact. The data transfer is utilized to send the new position reference, to acquire the experimental results, to debug and to download and to upload the DSP program code. The experimental setup contains a stationary central motion controller PC and a mobile PC (laptop). The

stationary PC and the laptop utilized in the experimental setup are commercial standard computers with an integrated wireless network interface.

The communication between the central motion controller PC and the laptop was implemented by a wireless network. The position sensing was completely done on-board (DSP controller) the active vehicle. Only the reference position value is transmitted from the stationary PC to the laptop transported by the active vehicle, as illustrated in Figure 3.7. One parallel cable connects the on-board VSI DSP to the mobile laptop. As the active vehicle can achieve high accelerations, a solid state hard-disk on the mobile laptop was installed. Solid state hard-disks are reliable for such application, since the device does not contain any spinning disks and movable read/write heads, thus a lack of moving parts virtually eliminates mechanical breakdowns.

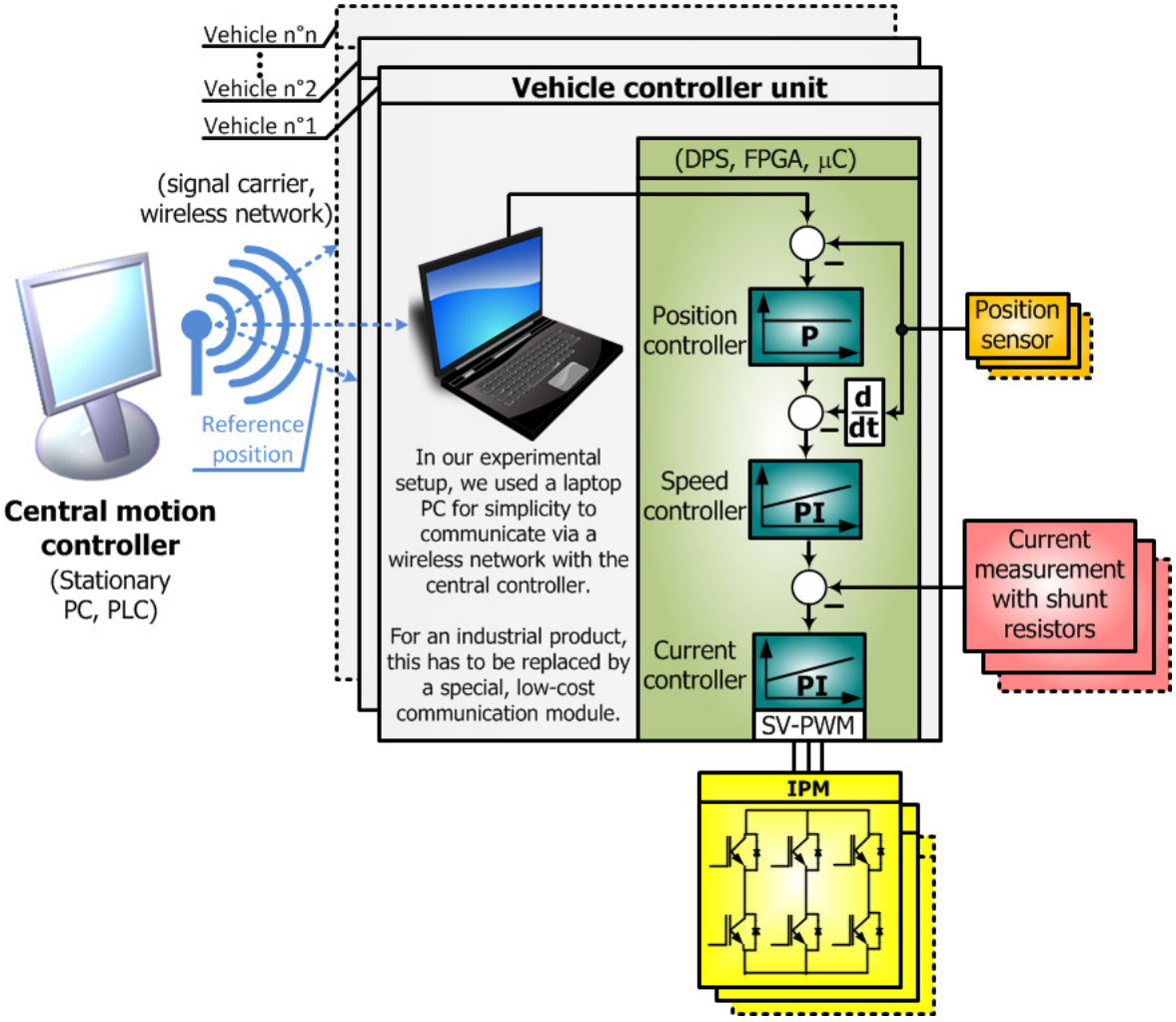


Figure 3.10: Structure example of data transfer for short primary topology.

In summary, the mobile laptop has the main duty to acquire the reference position signal from the stationary PC and send it to the on-board VSI DSP. However, the stationary PC works also as a user interface and supports some software programs used to debug the running program and to analyze experimental data. The software programs are described below:

- The CCS is responsible to compile, program and debug of the on-board DSP.

- The *MATLAB* was used to analyze the downloaded data during the tests.

For a real industrial application, the moving laptop could be replaced by an embedded computer, e.g. [73][74][75]. As a result, the embedded computer may communicate with the on-board DSP by SPI [69] or UART, remaining the wireless communication with the central motion controller.

Another possibility of data transmission is to use the primary conductor loop as a signal carrier. This concept of integrated data transfer ensures to be immune to an environment with high interference and can achieve data rate up to 187.5kBit/s [30][76]. The data transfer uses a significantly higher frequency, thus a clear differentiation between data signals and the power transfer is granted [30][76]. The reference position data are received by one on-board data pick-up. Then, the data are directly transmitted to the DSP without an intermediary embedded computer or a PLC. Figure 3.10 shows a structure example of data transfer for short primary topology with multiple vehicles.

# 4. Mathematical Model

This chapter presents the mathematical model for linear induction motor and the permanent magnet linear synchronous motor. Each machine is employed in the experimental prototype. These mathematical models are necessary to implement the field oriented control, and they will be presented in the following sections. Accurate estimated linear motor parameters have been assumed in both models.

## 4.1. Assumptions

The principle of operation of a linear motor can be compared to the principle of a rotary. In order to simplify the investigations and assume that the rotary motor mathematical model and the linear motor mathematical model are analogous [2][8][14], the following assumptions are introduced:

- There are no impacts of all kind of boundary effects.
- Magnetic saturation, iron losses and space harmonics are neglected.
- A zero component in voltages and currents is neglected.
- Basically, space vectors can be represented in any reference frame. Here we use the in rotating *AB*- reference frame.
- As space harmonics are neglected, there is no cogging force.
- The primary is equipped with symmetrical three-phase windings.
- The primary is supplied by controlled currents.

## 4.2. Rotating *AB*- reference frame

The operation of a three-phase AC machine is described by its voltage equations and inductances. The basic motor equations which describe the behavior of such machines have time variable coefficients, becoming a complex solution. In order to study such differential equations without time and position dependencies, it is necessary to change to a time invariant equation-system and to fix the reference frame in an arbitrary axis [56][77]. The well-known methods to derive these equations are based on the Clark and Park transformations [56]. By using these transformations, the number of variables decreases from three to two as no zero component is considered. Moreover, in steady state all variables are constant [56][77]. Such methods are widely implemented in control algorithms on DSP, FPGA and microcontrollers. The above mentioned transformations are detailed presented in appendix B.1. and B.2.

In this thesis, all space vectors are expressed in the rotating *AB*- reference frame either for synchronous or induction motor operation, as shown in Figure 4.1. The rotating reference frame is oriented towards (or aligned with) the secondary flux vector, which is called field orientation. In other words, the secondary flux has a component only in the *A*-axis, but there is no component in the *B*-axis.

For the induction motor operation, the synchronous speed $v_{syn}$ can be expressed by the mechanical speed $v_m$ and the slip speed $v_2$, as follows:

$$v_{syn} = v_m + v_2 \tag{4.1}$$

And obviously,

$$\beta_k = \beta_m + \beta_2 \tag{4.2}$$

where: $\beta_2$ is slip angle,

$\beta_m$ is the measured mechanical angle $\beta_{mech}$ multiplied by the number of pole pairs.

$\beta_k$ is the angular position of the secondary flux.

The angles (- and the speeds as their derivatives-) are arbitrary functions of the time. The measured mechanical angle $\beta_m$ is given by:

$$\beta_m = \frac{\pi}{\tau} x \tag{4.3}$$

where: $x$ is the acquired position.

While the secondary flux linkage $\Psi_2$ for the induction motor operation is produced by induced currents on the secondary, the secondary flux for synchronous motor operation is generated by stationary magnets $\Psi_{pm}$. There, the secondary flux is electrically fixed to the secondary and rotates with the electrical secondary speed, as displayed in Figure 4.1.

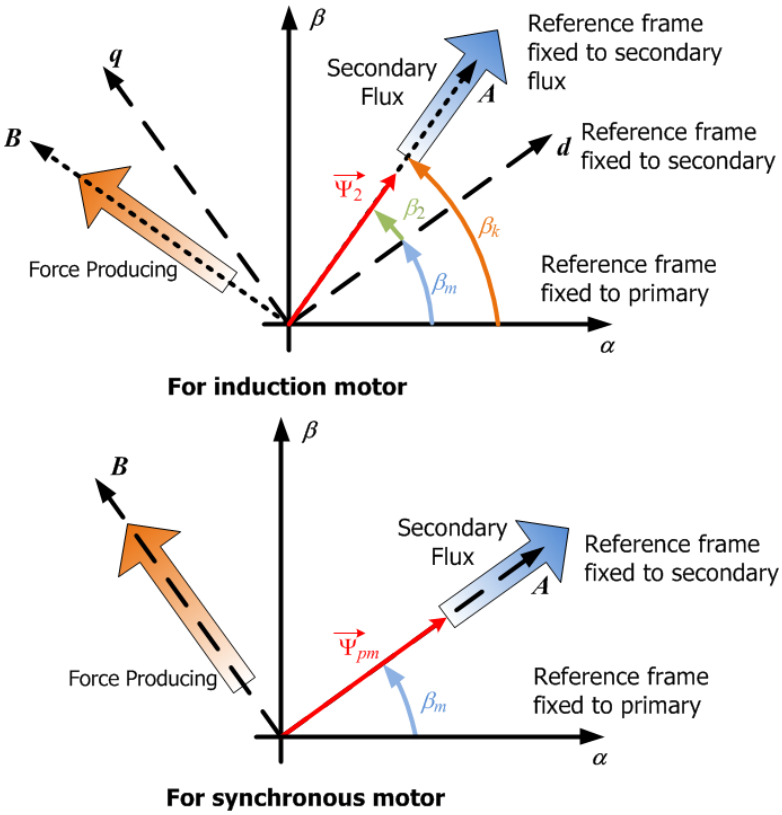


Figure 4.1: Rotating *AB*- reference frame for induction and synchronous motor operation

As the slip speed for synchronous motor operation is zero, the synchronous speed of the primary $v_{syn}$ and the mechanical speed $v_m$ have the same value in steady state. As a result, the synchronous speed and angular position of the secondary flux $\beta_k$ are given in (4.4) and (4.5).

$$v_{syn} = v_m \tag{4.4}$$

$$\beta_k = \beta_m \tag{4.5}$$

## 4.3. Dynamic model of the LIM

The mathematical model outlines the thrust force production in a linear motor. For the experimental setup, it is utilized a short primary linear drive with combined operation mode (induction or synchronous) in different sections, thus the three-phase distributed windings are placed in the primary core slots and each secondary (induction rail or PM) is fixed to a back iron, as illustrated in Figure 4.2.

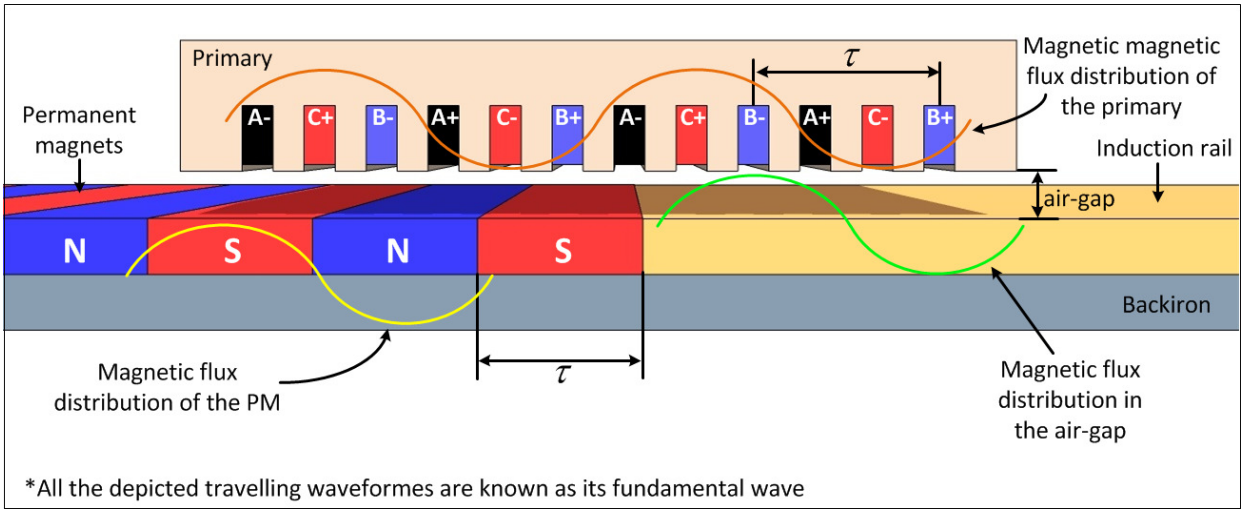


Figure 4.2: Magnetic flux distribution for a short primary linear drive using induction or synchronous operation in different sections.

For the induction motor, which is shown in the right half of Fig. 4.2, the three-phase motor model is equivalent to a three-phase transformer model, thus the electric model equations are very similar. The secondary is equivalent to a three-phase symmetrical winding and its parameters are transferred to the primary. Moreover, only the fundamental sinusoidal spatial field (flux) distribution is considered, as shown in Figure 4.2.

Therefore, the primary phase voltage equations of the LIM are given as follows:

$$\begin{aligned} u_{1a} &= R_1 i_{1a} + \frac{d\Psi_{1a}}{dt} \\ u_{1b} &= R_1 i_{1b} + \frac{d\Psi_{1b}}{dt} \\ u_{1c} &= R_1 i_{1c} + \frac{d\Psi_{1c}}{dt} \end{aligned} \tag{4.6}$$

where: $\Psi_1$ is the primary flux,
$i_1$ is the primary phase current,
$R_1$ is the primary resistance,
$u_1$ is the primary phase voltage.

and the "*a*,*b*,*c*" subscripts denote the quantities in the stationary three-phase (abc) reference frame.

The secondary phase voltage equations are:

$$\begin{aligned} u_{2a} &= R_2 i_{2a} + \frac{d\Psi_{2a}}{dt} \\ u_{2b} &= R_2 i_{2b} + \frac{d\Psi_{2b}}{dt} \\ u_{2c} &= R_2 i_{2c} + \frac{d\Psi_{2c}}{dt} \end{aligned} \tag{4.7}$$

where: $u_2$ is the secondary phase voltage, which is zero for the induction rail,
$R_2$ is the secondary resistance,
$\Psi_2$ is the secondary flux,
$i_2$ is the secondary phase current.

By transforming the current space vector in the reference frame presented in the previous section, the current space vector is aligned with the secondary flux space vector then only two independent DC-current components of the actual three-phase currents are observed (see Figure B.2 in appendix). Such transformation simplifies the controller design [56][78]. The LIM voltage equations (4.6) and (4.7) in the rotating *AB*- reference frame are:

$$\begin{aligned} u_{1A} &= R_1 i_{1A} + \frac{d\Psi_{1A}}{dt} - \underbrace{\frac{\pi}{\tau} v_1}_{\omega_{syn}} \Psi_{1B} \\ u_{1B} &= R_1 i_{1B} + \frac{d\Psi_{1B}}{dt} + \underbrace{\frac{\pi}{\tau} v_1}_{\omega_{syn}} \Psi_{1A} \end{aligned} \tag{4.8}$$

$$\begin{aligned} u_{2A} &= R_2 i_{2A} + \frac{d\Psi_{2A}}{dt} - \underbrace{\frac{\pi}{\tau}(v_1 - v_m)}_{\omega_2} \Psi_{2B} \\ u_{2B} &= R_2 i_{2B} + \frac{d\Psi_{2B}}{dt} + \underbrace{\frac{\pi}{\tau}(v_1 - v_m)}_{\omega_2} \Psi_{2A} \end{aligned} \tag{4.9}$$

where: $\omega_{syn}$ is the synchronous angular speed,
$\omega_2$ is the slip angular speed,
and the subscripts "*A*, *B*" denote the quantities in the rotating *AB*- reference frame.

Like in a transformer, the primary and secondary are coupled by a magnetizing self-inductance *M*. The *AB*- flux linkages of the primary and secondary are given by:

$$\Psi_{1A} = L_{i1} i_{1A} + M i_{2A} \tag{4.10}$$

$$\Psi_{1B} = L_{i1} i_{1B} + M i_{2B}$$

$$\Psi_{2A} = M i_{1A} + L_{i2} i_{2A} \tag{4.11}$$

$$\Psi_{2B} = M i_{1B} + L_{i2} i_{2B}$$

where: $L_{i1}$ is the primary inductance for induction operation,
$L_{i2}$ the secondary inductance for induction operation,
and the subscript "i" denotes the induction operation.

From the equations (4.10) and (4.11) the currents can be rewritten as:

$$\begin{aligned} i_{1A} &= \frac{1}{\sigma L_{i1}}\Psi_{1A} - \frac{M}{\sigma L_{i1}L_{i2}}\Psi_{2A} \\ i_{1B} &= \frac{1}{\sigma L_{i1}}\Psi_{1B} - \frac{M}{\sigma L_{i1}L_{i2}}\Psi_{2B} \end{aligned} \tag{4.12}$$

$$\begin{aligned} i_{2A} &= \frac{-M}{\sigma L_{i1}L_{i2}}\Psi_{1A} + \frac{1}{\sigma L_{i2}}\Psi_{2A} \\ i_{2B} &= \frac{-M}{\sigma L_{i1}L_{i2}}\Psi_{1B} + \frac{1}{\sigma L_{i2}}\Psi_{2B} \end{aligned} \tag{4.13}$$

where: $\sigma$ is the Blondel's leakage factor.

$$\sigma = 1 - \frac{M^2}{L_{i1}L_{i2}} = \frac{L_{i1}L_{i2} - M^2}{L_{i1}L_{i2}} \tag{4.14}$$

In order to get the time behavior of the LIM, a differential equation is derived, which contains only the primary voltage and the flux linkages. Then, inserting (4.13) into (4.9) results in the following equations:

$$\begin{aligned} \frac{d\Psi_{2A}}{dt} &= \frac{R_2 M}{\sigma L_{i1}L_{i2}}\Psi_{1A} - \frac{R_2}{\sigma L_{i2}}\Psi_{2A} + \frac{\pi}{\tau}\left(\nu_{syn} - \nu_m\right)\Psi_{2B} + u_{2A} \\ \frac{d\Psi_{2B}}{dt} &= \frac{R_2 M}{\sigma L_{i1}L_{i2}}\Psi_{1B} - \frac{R_2}{\sigma L_{i2}}\Psi_{2B} - \frac{\pi}{\tau}\left(\nu_{syn} - \nu_m\right)\Psi_{2A} + u_{2B} \end{aligned} \tag{4.15}$$

With the derivative of equations (4.12), and inserting in (4.8) and (4.15) yields:

$$\begin{aligned} \frac{di_{1A}}{dt} &= \frac{1}{\sigma L_{i1}}\left(-R_1 i_{1A} + \frac{\pi}{\tau}\nu_{syn}\Psi_{1B} + u_{1A}\right) - \frac{M}{\sigma L_{i1}L_{i2}}\left(\frac{R_2 M}{\sigma L_{i1}L_{i2}}\Psi_{1A} - \frac{R_2}{\sigma L_{i2}}\Psi_{2A} + \frac{\pi}{\tau}\left(\nu_{syn} - \nu_m\right)\Psi_{2B} + u_{2A}\right) \\ \frac{di_{1B}}{dt} &= \frac{1}{\sigma L_{i1}}\left(-R_1 i_{1B} - \frac{\pi}{\tau}\nu_{syn}\Psi_{1A} + u_{1B}\right) - \frac{M}{\sigma L_{i1}L_{i2}}\left(\frac{R_2 M}{\sigma L_{i1}L_{i2}}\Psi_{1B} - \frac{R_2}{\sigma L_{i2}}\Psi_{2B} - \frac{\pi}{\tau}\left(\nu_{syn} - \nu_m\right)\Psi_{2A} + u_{2B}\right) \end{aligned} \tag{4.16}$$

Finally, inserting (4.12) into (4.16), we can find the differential equations of the primary currents. Then:

$$\begin{aligned} \frac{di_{1A}}{dt} &= \frac{1}{\sigma L_{i1}}u_{1A} - \frac{M}{\sigma L_{i1}L_{i2}}u_{2A} - \frac{1}{\sigma L_{i1}}\left(R_1 + \frac{R_2 M^2}{{L_{i2}}^2}\right)i_{1A} + \frac{R_2 M}{\sigma L_{i1}{L_{i2}}^2}\Psi_{2A} + \frac{\pi}{\tau}\nu_{syn} i_{1B} + \frac{M}{\sigma L_{i1}L_{i2}}\frac{\pi}{\tau}\nu_m\Psi_{2B} \\ \frac{di_{1B}}{dt} &= \frac{1}{\sigma L_{i1}}u_{1B} - \frac{M}{\sigma L_{i1}L_{i2}}u_{2B} - \frac{1}{\sigma L_{i1}}\left(R_1 + \frac{R_2 M^2}{{L_{i2}}^2}\right)i_{1B} + \frac{R_2 M}{\sigma L_{i1}{L_{i2}}^2}\Psi_{2B} - \frac{\pi}{\tau}\nu_{syn} i_{1A} - \frac{M}{\sigma L_{i1}L_{i2}}\frac{\pi}{\tau}\nu_m\Psi_{2A} \end{aligned} \tag{4.17}$$

### 4.3.1 Electromechanical thrust force equation of the LIM

The instantaneous input power for the induction $P_{in}$ operation is given by:

$$\begin{aligned} P_{in} &= \left(u_{1a}i_{1a} + u_{1b}i_{1b} + u_{1c}i_{1c} + u_{2a}i_{2a} + u_{2b}i_{2b} + u_{2c}i_{2c}\right) \\ &= \frac{3}{2}\left(i_{1A}u_{1A} + i_{1B}u_{1B} + i_{2A}u_{2A} + i_{2B}u_{2B}\right) \end{aligned} \tag{4.18}$$

where the secondary voltage is zero.

By substituting (4.8) and (4.9) into (4.18) we get (4.19):

$$P_{in} = \frac{3}{2}\left( \underbrace{\left(R_1\left(i_{1A}{}^2 + i_{1B}{}^2\right) + R_2\left(i_{2A}{}^2 + i_{2B}{}^2\right)\right)}_{P_{iohm}} + \underbrace{\left(\frac{d\Psi_{1A}}{dt}i_{1A} + \frac{d\Psi_{1B}}{dt}i_{1B} + \frac{d\Psi_{2A}}{dt}i_{2A} + \frac{d\Psi_{2B}}{dt}i_{2B}\right)}_{P_{imag}} + \underbrace{\left(v_1\frac{\pi}{\tau}\left(\Psi_{1A}i_{1B} - \Psi_{1B}i_{1A}\right) + \left(v_{syn} - v_m\right)\frac{\pi}{\tau}\left(\Psi_{2A}i_{2B} - \Psi_{2B}i_{2A}\right)\right)}_{P_{iem}} \right) \tag{4.19}$$

The equation (4.19) represents the electrical power into the terminals of LIM. Moreover, it can be divided into three parts: the power dissipated in the primary and secondary resistances $P_{iohm}$, the energy stored in the magnetic field $P_{imag}$ and the electromechanical output power being converter from electrical to mechanical form $P_{iem}$.

Using the flux linkage relationship in (4.10) and (4.11), we can show that:

$$\Psi_{1A}i_{1B} - \Psi_{1B}i_{1A} = -\left(\Psi_{2A}i_{2B} - \Psi_{2B}i_{2A}\right) \tag{4.20}$$

Therefore, $P_{iem}$ in (4.19) can also be expressed in the following forms:

$$P_{iem} = \frac{3}{2}\left(v_m\frac{\pi}{\tau}\left(\Psi_{1A}i_{1B} - \Psi_{1B}i_{1A}\right)\right) \tag{4.21}$$

Since $P_{iem}$ is the product of speed and thrust force, the thrust force of a three-phase LIM is given by:

$$\begin{aligned} F_{in} &= \frac{2p}{2}\frac{P_{em}}{v_m} \\ &= \frac{3}{2}\frac{2p}{2}\frac{\pi}{\tau}\left(\Psi_{1A}i_{1B} - \Psi_{1B}i_{1A}\right) \end{aligned} \tag{4.22}$$

where: $2p$ is the number of poles.

The motion equation can be expressed as:

$$m_v\frac{dv_m}{dt} = F_{in} - F_{friction} \tag{4.23}$$

where: $m_v$ is the total mass (active vehicle + load weight),

$F_{friction}$ is friction force.

## 4.4. LIM field oriented control

The FOC allows performing a fast and fully decoupled control of thrust force and secondary flux in LIM drives, as for DC-machines [78]. In order to obtain such decoupled control, the controllers maintain the secondary flux aligned with the *A*-axis then the *B*-axis component of the secondary flux $\Psi_{2B}$ would be zero, that is:

$$\Psi_{2B} = Mi_{1B} + L_{i2}i_{2B} = 0 \tag{4.24}$$

Then,

$$i_{2B} = -\frac{M}{L_{i2}} i_{1B} \tag{4.25}$$

As the secondary is a conduction copper plate ($u_{2A}$=$u_{2B}$=0) and inserting (4.9) into (4.11), the following equation is obtained:

$$\frac{L_{i2}}{R_2}\left( \frac{d\Psi_{2A}}{dt} - \frac{\pi}{\tau}\underbrace{\left(v_{syn} - v_m\right)}_{v_2}\Psi_{2B} \right) + \Psi_{2A} = Mi_{1A} \tag{4.26}$$

$$\frac{L_{i2}}{R_2}\left( \frac{d\Psi_{2B}}{dt} + \frac{\pi}{\tau}\underbrace{\left(v_{syn} - v_m\right)}_{v_2}\Psi_{2A} \right) + \Psi_{2B} = Mi_{1B} \tag{4.27}$$

With $\Psi_{2B}$=0, the equation (4.26) is rewritten as:

$$\frac{L_{i2}}{R_2}\frac{d\Psi_{2A}}{dt} + \Psi_{2A} = Mi_{1A} \tag{4.28}$$

If the LIM is in steady state and the secondary flux is held constant, the secondary flux is only linked to the primary current. Therefore:

$$\Psi_{2A} = Mi_{1A} \tag{4.29}$$

Taking the equation (4.27), the relationship between the slip speed $v_2$ and the ratio of the primary currents $i_{1A}$ and $i_{1B}$ is obtained, thus:

$$v_2 = \frac{\tau}{\pi} \underbrace{\frac{R_2}{L_{i2}}}_{\frac{1}{T_{secondary}}} \frac{i_{1b}}{i_{1A}} \tag{4.30}$$

where: $T_{secondary} = \frac{L_{i2}}{R_2}$ is the secondary time constant.

Once the slip speed $v_2$ is determined, the angular position of the secondary flux $\beta_k$ is simply equal to:

$$\beta_k = \beta_m + \frac{\pi}{\tau}\int v_2 dt \tag{4.31}$$

Or using (4.30), we get:

$$\beta_k = \beta_m + \int \frac{1}{T_{secondary}} \frac{i_{1b}}{i_{1A}} dt \tag{4.32}$$

As the secondary position is delivered by the encoder, the slip angle is determined using (4.32). Such method can be used at standstill and low speed. However, the FOC can lose its performance, since the secondary resistance is temperature dependent or the secondary inductance is magnetic saturation dependent, resulting in a wrong calculation of the slip angle [12][56][78]. For this thesis, the error $T_{secondary}$ is assumed to be small.

Equations (4.10) and (4.11) are substituted into (4.22) and the electromagnetic thrust force can be expressed as:

$$F_{in} = \frac{3}{2}\frac{2p}{2}\frac{\pi}{\tau} M\left(i_{2A}i_{1B} - i_{2B}i_{1A}\right) \tag{4.33}$$

Finally, using (4.25) and (4.11) into (4.33) the electromagnetic thrust force can be rewritten as follows:

$$F_{in} = \frac{3}{2}\frac{2p}{2}\frac{\pi}{\tau}\frac{M}{L_{i2}}\Psi_{2A} i_{1B} = k_{if} i_{1B} \tag{4.34}$$

where: $k_{if}$ is the thrust force constant for the LIM.

Then, the thrust force constant for the LIM $k_{if}$ is:

$$k_{if} = \frac{3}{2}\frac{2p}{2}\frac{\pi}{\tau}\frac{M}{L_{i2}}\Psi_{2A} \tag{4.35}$$

In (4.34), it can be seen that the thrust force depends on the component of the primary current orthogonal to the secondary flux. The secondary flux itself depends on the component of the primary current, which has the same direction as the secondary flux. The current $i_{1A}$ is called flux producing component and $i_{1B}$ is called the force producing component of current [2][56][78], as shown in Figure 4.1.

### 4.4.1 Determination of the LIM thrust force constant

In order to find the LIM thrust force constant used in the experimental setup, a standstill force test was carried out. The force sensor is described in section 3.4. To acquire the measured force, the vehicle position was changed into steps of 2mm and three steps (3A, 5A, 8A) in the current $i_{1B}$ were applied, keeping the secondary flux constant ($i_{1A}$=3.6A). Figure 4.3 shows the test results of the force measurement.

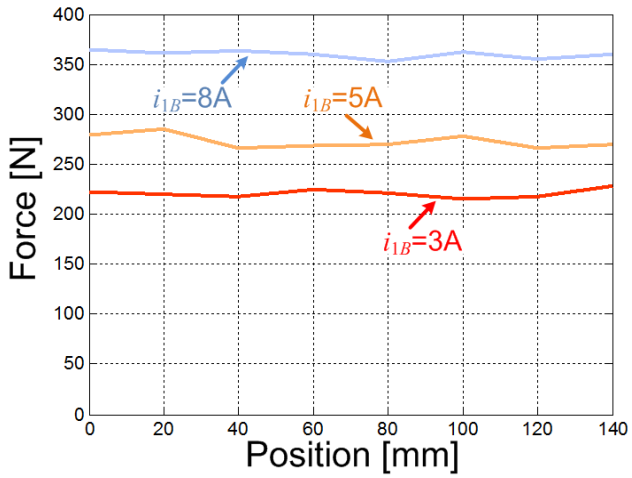


Figure 4.3: LIM test results of the standstill force measurement.

Based on the experimental results depicted in Figure 4.3, it was determined that the value of $k_{if}$ is 44.24N/A.

Summarizing, the main principle of the FOC for an LIM is to:

- Control $i_{1B}$ to produce the thrust force required by an outer speed control loop [78].
- Control $i_{1A}$ to set $\Psi_{2A}$ to a particular value. The flux controller can be omitted, if field-weakening operation is not required.

## 4.5. Dynamic model of the PMLSM

The PMLSM uses high-energy rare-earth permanent magnets, and is characterized by high thrust force density, higher efficiency, larger air-gap and rapid responses [12][79]. Its main disadvantage is the higher cost of the permanent magnets.

The short primary is utilized either by LIM or by PLMSM operation, but for the latter operation the secondary is composed by permanent magnets, as illustrated in the left half of Figure 4.2. For the PMLSM operation, the fields produced by the winding currents are assumed to be sinusoidally distributed in the air-gap. Likewise, the fundamental wave of the magnetic distribution of the PM is sinusoidal, as shown in Figure 4.2.

This assumption of sinusoidal distribution ignores the space harmonic, which may have secondary effects on the machine's behavior [79]. The primary phase voltage equations of the PMLSM are the same equations described in (4.6). Due to the stationary permanent magnets, the field magnetomotive force (MMF) is constant. Also there is no damper winding on the secondary part [79].

As the model of the LIM, the voltage equation can be expressed in rotating *AB*- reference frame in order to transform the time varying parameters into steady state constants, applying the linear transformation described in appendix B. Unlike the LIM, the reference frame is electrically fixed to the secondary, thus the flux produced by the stationary PM $\Psi_{pm}$ moves with synchronous speed aligned with the secondary, as shown in Figure 4.1.

Consequently, the relations between the rotating *AB*- and the *dq*- reference frames are presented in (4.36).

$$\begin{aligned} i_{1A} &= i_{1d}, i_{1B} = i_{1q} \\ u_{1A} &= u_{1d}, u_{1B} = u_{1q} \end{aligned} \tag{4.36}$$

All variables with subscripts "*d*, *q*" are used to the rotating *dq*- reference frame illustrated in Figure 4.1.

Considering (4.36), the voltage equations depicted in (4.8) are the general primary voltage equations of a three-phase AC machine in the rotating *AB*- reference frame, and they are valid also for the PMLSM. However, for the synchronous operation, the synchronous speed of the primary and the mechanical speed multiplied by the number of pole pairs are identical ($v_{syn}$=$v_m$).

Then, the equations (4.8) will be rewritten as follows:

$$\begin{aligned} u_{1A} &= R_1 i_{1A} + \frac{d\Psi_{1A}}{dt} - \underbrace{\frac{\pi}{\tau} v_m}_{\omega_{syn}} \Psi_{1B} \\ u_{1B} &= R_1 i_{1B} + \frac{d\Psi_{1B}}{dt} + \underbrace{\frac{\pi}{\tau} v_m}_{\omega_{syn}} \Psi_{1A} \end{aligned} \tag{4.37}$$

As the secondary flux $\Psi_{pm}$ generated by the permanent magnets is directly oriented to the *A*-axis, the secondary flux on the *B*-axis is zero. Therefore, the secondary linkage fluxes in the equations (4.37) are defined as:

$$\Psi_{1A} = L_{s1} i_{1A} + \Psi_{pm} \tag{4.38}$$

$$\Psi_{1B} = L_{s2} i_{1B} \tag{4.39}$$

where: $L_{s1}$ is the primary inductance for synchronous operation,

$L_{s2}$ the secondary inductance for synchronous operation,

and the subscript "s" denotes the synchronous operation.

From the equations (4.38) and (4.39) the currents can be calculated as:

$$i_{1A} = \frac{\left(\Psi_{1A} - \Psi_{pm}\right)}{L_{s1}} \tag{4.40}$$

$$i_{1B} = \frac{\Psi_{1B}}{L_{s2}} \tag{4.41}$$

In order to get differential equations of the PMLSM primary currents, we insert (4.38) and (4.39) into (4.37), then it results in the following equations:

$$\begin{aligned} \frac{di_{1A}}{dt} &= \frac{1}{L_{s1}} u_{1A} - \frac{R_1}{L_{s1}} i_{1A} + \frac{L_{s2}}{L_{s1}} \frac{\pi}{\tau} \nu_m i_{1B} \\ \frac{di_{1B}}{dt} &= \frac{1}{L_{s2}} u_{1B} - \frac{R_1}{L_{s2}} i_{1B} - \frac{L_{s1}}{L_{s2}} \frac{\pi}{\tau} \nu_m i_{1A} - \frac{1}{L_{s2}} \frac{\pi}{\tau} \nu_m \Psi_{pm} \end{aligned} \tag{4.42}$$

### 4.5.1 Electromechanical thrust force equation of the PMLSM

The expression for the electromechanical thrust force developed by the PMLSM can be obtained from the components of the instantaneous input power that is transferred across the air-gap. The instantaneous input power $P_{sn}$ for synchronous operation is given by:

$$\begin{aligned} P_{sn} &= \left(u_{1a} i_{1a} + u_{1b} i_{1b} + u_{1c} i_{1c}\right) \\ &= \frac{3}{2}\left(u_{1A} i_{1A} + u_{1B} i_{1B}\right) \end{aligned} \tag{4.43}$$

The power balance equation is obtained from (4.37), i.e:

$$P_{sn} = \frac{3}{2}\left( \underbrace{\left(R_1\left(i_{1A}{}^2 + i_{1B}{}^2\right)\right)}_{P_{sohm}} + \underbrace{\left(\frac{d\Psi_{1A}}{dt} i_{1A} + \frac{d\Psi_{1B}}{dt} i_{1B}\right)}_{P_{smag}} + \underbrace{\left(\nu_m \frac{\pi}{\tau}\left(\Psi_{1A} i_{1B} - \Psi_{1B} i_{1A}\right)\right)}_{P_{sem}} \right) \tag{4.44}$$

where: $P_{sohm}$ is ohmic losses of the PMLSM,

$P_{smag}$ is the rate of change in magnetic energy of the PMLSM,

$P_{sem}$ is the developed electromechanical output power of the PMLSM.

Dividing the electromechanical output power by mechanical speed $\nu_m$ of the secondary, we obtain the following expression for the electromechanical thrust force produced by a $2p$-pole PMLSM:

$$F_{sn} = \frac{2p}{2}\frac{P_{sem}}{v_m} = \frac{3}{2}\frac{2p}{2}\frac{\pi}{\tau}\left(\Psi_{1A} i_{1B} - \Psi_{1B} i_{1A}\right) \tag{4.45}$$

## 4.6. PMLSM Field oriented control

Unlike the LIM the PMLSM has a permanent and constant secondary flux with a certain preferred axis. With the simultaneous use of a position sensor, the secondary flux position can always be clearly identified, and field orientation is always guaranteed.

By substituting (4.38) and (4.39) into (4.45), the electromechanical thrust force $F_{sn}$ can be rewritten as:

$$F_{sn} = \frac{3}{2}\frac{2p}{2}\frac{\pi}{\tau}\left(\Psi_{pm} i_{1B} + \left(L_{s1} - L_{s2}\right) i_{1B} i_{1A}\right) \tag{4.46}$$

In (4.46), the electromechanical thrust force is separated into two components: a reluctance component and an excitation component. If the secondary phase inductance is bigger than the primary inductance ($L_{s2}$>$L_{s1}$), the second component contributes to a negative thrust force [77]. For a PLSM with no saliency, both secondary inductances are nearly identical ($L_{s2}$=$L_{s1}$). Therefore, the electromechanical is represented as follows:

$$F_{sn} = \frac{3}{2}\frac{2p}{2}\frac{\pi}{\tau}\Psi_{pm} i_{1B} = k_{sf} i_{1B} \tag{4.47}$$

where: $k_{sf}$ is the thrust force constant for the PMLSM and is given by:

$$k_{sf} = \frac{3}{2}\frac{2p}{2}\frac{\pi}{\tau}\Psi_{pm} \tag{4.48}$$

Due to constant secondary flux $\Psi_{pm}$, the thrust force in equation (4.47) is directly proportional to the *B*-axis current $i_{1B}$. Hence, the primary PMLSM current $i_1$ does not produce the secondary flux, as in the case of the LIM-FOC (Equation 4.34), but only produces the electromechanical thrust force and contains only the current component $i_{1B}$. Furthermore, for PMLSM a with negligible small saliency the primary current is controlled to obtain a right angle between the primary current and the secondary flux vector, in order to achieve the maximum thrust force. Therefore, the current component $i_{1A}$ will be set to zero, during the constant thrust force control [56][77].

### 4.6.1 Determination of the LIM thrust force constant

As the air-gap at the permanent magnet side was increased ($\gamma_s$=2mm) in comparison with the recommended by the datasheet ($\gamma_s$=0.6mm) (to reduce the very high attractive force, which could slowly slide down the adjustment profile), the thrust force constant for the PMLSM was determined, using same mechanical procedure presented in the section 4.4. The thrust force was measured for current steps of 3A, 5A, 8A in the *B*-axis current $i_{1B}$ and as mentioned above the current $i_{1A}$ was regulated to zero. Figure 4.4 shows the PMLSM test results of the standstill force measurement.

Based on the experimental results depicted in Figure 4.4, it was determined that the value of $k_{sf}$ is 83.05N/A.

In summary, the main principle of the FOC for a PMLSM is to:

- Control $i_{1A}$ to be zero and keep the angle between $i_{1B}$ and $\Psi_{pm}$ at 90 degrees, if the drive does not work in the field-weakening area [80].
- Control $i_{1B}$ to produce the thrust force required by an outer speed control loop [78].

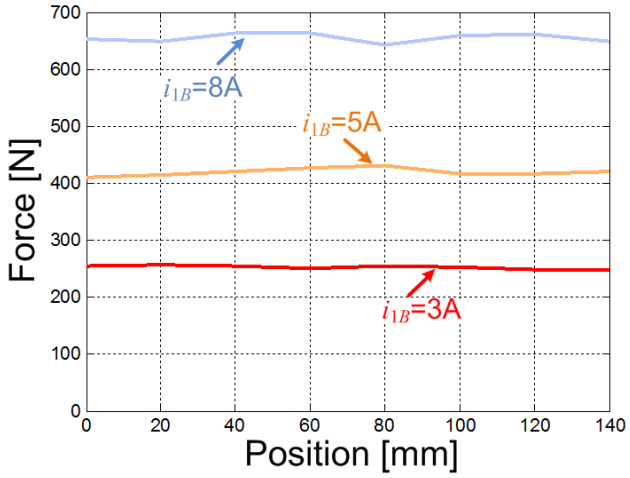


Figure 4.4: PMLSM test results of the standstill force measurement.

# 5. Transition Control Strategy

As depicted in Figure 1.8 (chapter 1, section 1.24), the short primary linear motor must be able to move between the two different sections. Thus, a suitable vehicle motion control strategy is required, in order to regulate the speed without jerks. This chapter will present the adopted transition control strategy, when the vehicle is leaving or entering a processing station. The implemented FOC algorithm for both operations is based on the mathematical models described in the previous chapter. For the position control, a magneto-resistive incremental encoder, which was mounted at the active vehicle, and a magnetic linear scale, which covers the whole passive track, were utilized. Furthermore, the experimental test results, displaying the transition between the stationary PMs and the induction rail, will be presented in the following.

## 5.1. Control design

Usually, the structure of the control loop plays a decisive role in the performance of a motor drive system. The cascade control, including several superimposed control loops for force producing current, speed and position is the traditional method used in servo motor control, and it is widely applied in the industry [2][12][56][78][80]. The cascade control has the following advantages:

- The faster inner loop compensates the effect of some disturbances, before they affect the outer loops.
- It can be combined with feed-forward control, to improve the time response and compensate disturbances.
- The reference value is limited in each loop, thus it suppresses possible oscillations and windup effects.
- The controller uses standard controllers (P, PI, and PID) and their parameters can be easily tuned.
- Simple procedures for diagnostic and test can be made just by opening of outer loops.

For material handling applications, the positioning of the work piece carrier is very important. The outermost control loop is the position controller and it controls the reference position $x^*$ transmitted by the motion controller. The output of the position controller is the speed reference $v_m^*$ of the speed control loop and its output is the thrust force reference current component $i_{1B}^*$. The current controller is the inner most and fastest loop. It controls the current components of flux $i_{1A}$ and thrust force $i_{1B}$. In addition, the current controllers should ensure an ideal coupling between the flux producing component and the thrust force producing component, especially in case of induction motor operation, where both components are strongly coupled [78][80].

During drive operation, the flux producing current $i_{1A}$ is kept constant ($i_{1A}>0$) when the active vehicle (primary) is traveling on the transporting section, and the thrust force is controlled by the current $i_{1B}$. On the other hand, when the active vehicle is within the processing section, the current $i_{1A}$ is controlled to zero ($i_{1A}=0$), since in constant thrust force operation, the secondary flux $\Psi_{pm}$

generated by the PM is constant, and only $i_{1B}$ controls the electromagnetic thrust force. Therefore, for the motion control of the linear motor, the primary current values and the position of the secondary flux are necessary. The VSI is responsible for supplying the linear machine's terminal with voltages, which were commanded by the current controllers.

### 5.1.1 Design of the current controllers for LIM operation

The space state representation of the LIM with the primary currents and secondary flux linkages components as state variables for LIM-FOC operation can be written as:

$$\begin{bmatrix} \frac{di_{1A}}{dt} \\ \frac{di_{1B}}{dt} \\ \frac{d\Psi_{2A}}{dt} \\ 0 \end{bmatrix} = A \begin{bmatrix} i_{1A} \\ i_{1B} \\ \Psi_{2A} \\ 0 \end{bmatrix} + \begin{bmatrix} \frac{1}{\sigma L_{i1}} & 0 \\ 0 & \frac{1}{\sigma L_{i1}} \\ 0 & 0 \\ 0 & 0 \end{bmatrix} \begin{bmatrix} u_{1A} \\ u_{1B} \\ 0 \\ 0 \end{bmatrix} \tag{5.1}$$

where

$$A = \begin{bmatrix} -\frac{1}{\sigma L_{i1}}\left(R_1 + \frac{R_2 M^2}{L_{i2}^2}\right) & \frac{\pi}{\tau} v_{syn} & \frac{1}{\sigma L_{i1}} \frac{R_2 M}{L_{i2}^2} & 0 \\ -\frac{\pi}{\tau} v_{syn} & -\frac{1}{\sigma L_{i1}}\left(R_1 + \frac{R_2 M^2}{L_{i2}^2}\right) & -\frac{1}{\sigma L_{i1}} \frac{M}{L_{i2}} \frac{\pi}{\tau} v_m & 0 \\ \frac{M R_2}{L_{i2}} & 0 & -\frac{R_2}{L_{i2}} & 0 \\ 0 & \frac{M R_2}{L_{i2}} & -\frac{\pi}{\tau} v_m & 0 \end{bmatrix}$$

From (5.1) we can take the differential equations of the primary circuit, then:

$$\frac{di_{1A}}{dt} = \frac{1}{\sigma L_{i1}} \left( u_{1A} - \left( R_1 + \frac{R_2 M^2}{L_{i2}^2} \right) i_{1A} + \underbrace{\left( \frac{\pi}{\tau} v_{syn} \sigma L_{i1} i_{1B} + \frac{R_2 M}{L_{i2}^2} \Psi_{2A} \right)}_{A_{LIM}} \right) \tag{5.2}$$

$$\frac{di_{1B}}{dt} = \frac{1}{\sigma L_{i1}} \left( u_{1B} - \left( R_1 + \frac{R_2 M^2}{L_{i2}^2} \right) i_{1B} - \underbrace{\left( \frac{\pi}{\tau} v_{syn} \sigma L_{i1} i_{1A} + \frac{M}{L_{i2}} \frac{\pi}{\tau} v_m \Psi_{2A} \right)}_{B_{LIM}} \right) \tag{5.3}$$

From the first two terms of the above equations, we can find out that the time constant of the primary current is $\frac{\sigma L_{i1}}{R_1 + \frac{R_2 M^2}{L_{i2}^2}}$ and the current controller can be designed by using this time constant.

The remaining terms ($A_{LIM}$ and $B_{LIM}$) in the differential equations (5.2) and (5.3) depict the additional coupling, i.e. the equation (5.1) contains values of the B-component and vice-versa. These

terms can be compensated to achieve a completely independent regulation, just by adding/subtracting (feed-forward) these terms to the output signals of the PI current controllers [78]. Also, the feed-forward control improves the dynamic response of the machine [78][81]. Since the speed changes are orders of magnitude slower than changes in currents, this is not a severe problem for the current control. However, it is reported in [82] that the coupling terms reduce the convergence speed of the estimation in sensorless estimation methods, so the feed-forward control will be implemented in this thesis for LIM-FOC operation.

The transfer function of the motor model is represented by simple linear first-order differential equations and they are presented in equation (5.4).

$$\frac{i_{1B}(s)}{u_{1B}{}^{*}(s)} = \frac{i_{1A}(s)}{u_{1A}{}^{*}(s)} = k_{LIM}\,\frac{1}{T_{LIM}s+1}$$
$$k_{LIM} = \frac{1}{R_1 + \frac{R_2 M^2}{L_{i2}{}^2}}, T_{LIM} = \frac{\sigma L_{i1}}{R_1 + \frac{R_2 M^2}{L_{i2}{}^2}} \tag{5.4}$$

where: $T_{LIM}$ is the time constant of the LIM current loop,
$k_{LIM}$ is the gain of the LIM current loop,
and the superscript "*" denotes the reference quantities.

The current control is performed by the comparison of the reference currents ($i_{1A}$*, $i_{1B}$*) with the acquired primary currents ($i_{1A}$, $i_{1B}$). Figure 5.1 illustrates the block diagram of the current control loop of the primary LIM, where the coupling terms are compensated. There, the inverter and the control time delays are modeled as a first-order lag element with a time constant of $T_D$=1.5$T_{sample}$ [56]. The secondary flux controller is omitted because the field-weakening operation is not required. Then, from (4.29) the value of $i_{1A}$ is selected.

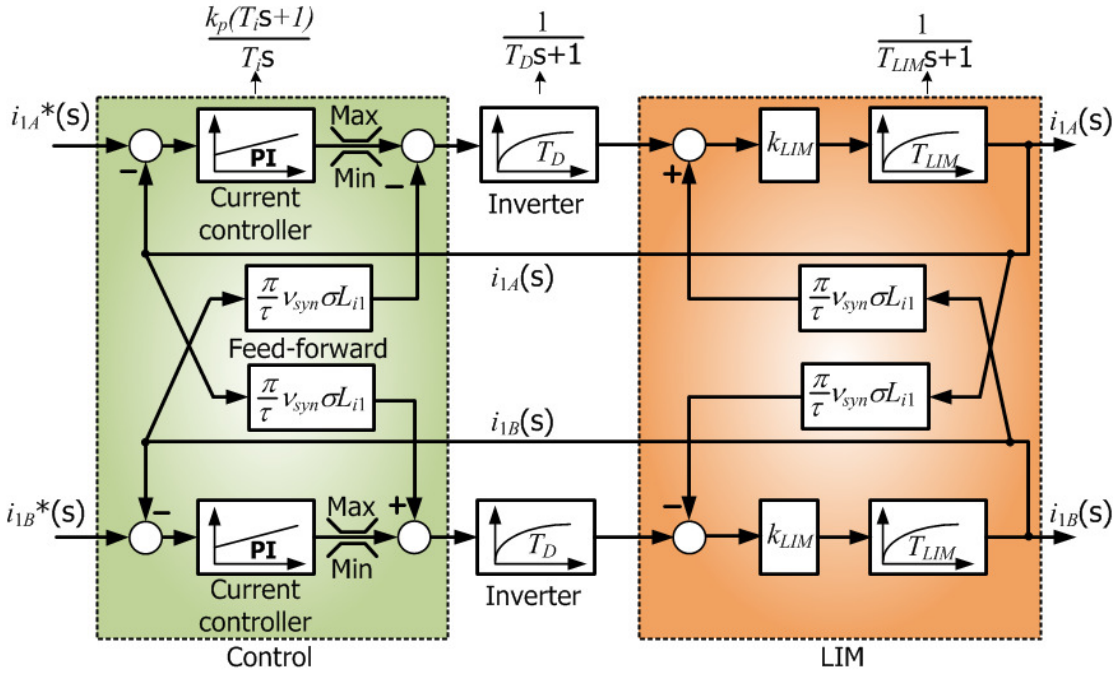


Figure 5.1: Block diagram of the current loop with feed-forward decoupling for LIM operation.

In (5.2) and (5.3), the second term of $A_{LIM}$ and $B_{LIM}$ are small compared to the first term, thus they could be neglected in practice [81]. If it is assumed that only the first terms of $A_{LIM}$ and $B_{LIM}$ are compensated by the feed-forward control, the current controller parameters can be determined by using the amplitude optimum method [56]. Then, the integral time $T_i$ and gain $k_p$ of the current PI controllers are:

$$T_i = T_{LIM} \tag{5.5}$$

$$k_p = \frac{1}{2T_D k_{LIM}} \tag{5.6}$$

After it had been compensated, the response function of the closed current loop is given approximately as a first-order lag element, as described below:

$$F_{W,current}(s) = \frac{1}{2T_D{}^2 s^2 + 2T_D + 1} \approx \frac{1}{2T_D s + 1} \tag{5.7}$$

To avoid oscillations caused by physical limitation of the VSI output voltage, an anti-windup PI current controller (according to appendix B.3 is used) [80]. As the primary phase voltage space vector $\vec{u}_1$ is composed by two different components $u_{1A}$ and $u_{1B}$, both are limited according to equation (5.8). Also in (5.8), the $u_{1B}$ is truncated and the flux producing voltage component $u_{1A}$ has priority.

$$\begin{aligned} u_{1A,\max} &= sign(u_{1A})\left|\vec{u}_1\right|_{\max} \\ u_{1B,\max} &= sign(u_{1B})\sqrt{\left|\vec{u}_1\right|_{\max}{}^2 - u_{1A}{}^2} \end{aligned} \tag{5.8}$$

where: $\left|\vec{u}_1\right|_{\max} = \frac{V_{dclink}}{\sqrt{3}}$ (see appendix B.4).

### 5.1.2 Design of the current controllers for PMLSM operation

Following the same procedure presented in the previous subsection and considering ($L_{s2}$=$L_{s1}$), the differential equations of the primary current (4.42) for PMLSM-FOC are rewritten as:

$$\frac{di_{1A}}{dt} = \frac{1}{L_{s1}}\left( u_{1A} - R_1 i_{1A} + \underbrace{\frac{\pi}{\tau} v_m L_{s1} i_{1B}}_{A_{PMLSM}} \right) \tag{5.9}$$

$$\frac{di_{1B}}{dt} = \frac{1}{L_{s2}}\left( u_{1B} - R_1 i_{1B} - \underbrace{\left( \frac{\pi}{\tau} v_m L_{s1} i_{1A} + \frac{\pi}{\tau} v_m \Psi_{pm} \right)}_{B_{PMLSM}} \right) \tag{5.10}$$

Both equations presented above, obviously pointed out that the PMLSM is coupled in the electrical states with the primary currents $i_{1A}$ and $i_{1B}$, as $v_m$ varies much slower than the currents, it can be treated as a linear system.

Using a similar control structure as in the case of the LIM, the PMLSM-FOC assures that the flux producing current component $i_{1A}$ stays very near to zero (constant thrust force operation), thus the left-side term of $B_{PMLSM}$ in (5.10) could be disregarded.

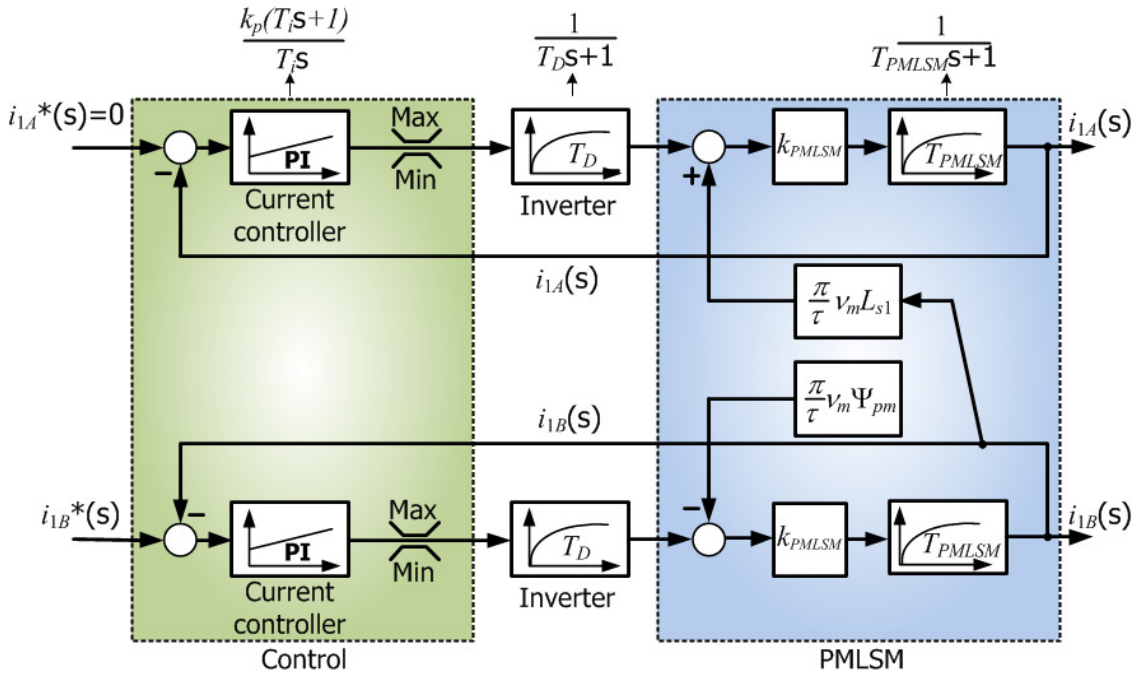


Figure 5.2: Block diagram of the current loop for PMLSM operation.

In (5.9), the term $A_{PMLSM}$ is the current cross coupling term which causes disturbances, when the machine is accelerating, and for better dynamic performance, it may be compensated. The right-side term in $B_{PMLSM}$ in (5.10) represents the induced electromagnetic field (EMF) and it is a slowly varying disturbance which is proportional to the speed and can be easy compensated by injecting an offset voltage (back EMF feed-forward) [56]. Whether feed-forward compensations are employed or not, the current control at high speed will not totally eliminate the disturbances, anyhow it improves the dynamic [21][83]. Figure 5.2 show the current control loop of the PMLSM using a PI controller, where the couplings terms are neglected.

For both primary currents, the controlled plant of a PMLSM with no saliency is represented by a first-order lag element. Hence:

$$\frac{i_{1B}(s)}{u_{1B}^*(s)} = \frac{i_{1A}(s)}{u_{1A}^*(s)} = k_{PMLSM} \frac{1}{T_{PMLSM} s+1}$$
$$k_{PMLSM} = \frac{1}{R_1}, T_{PMLSM} = \frac{L_{1s}}{R_1} = \frac{L_{2s}}{R_1} \tag{5.11}$$

where: $T_{PMLSM}$ is the time constant of the PMLSM current loop,

$k_{PMLSM}$ is the gain of the PMLSM current loop.

The processes to tune the PI controller parameters and to limit the VSI output voltage are the same as described in the previous subsection.

The obtained current PI controller parameters are given in (5.12) and (5.13).

$$T_i = T_{PMLSM} \tag{5.12}$$

$$k_p = \frac{1}{2T_D k_{PMLSM}} \tag{5.13}$$

### 5.1.3 Design of the speed controller for LIM operation

Starting with the inner current control loop, the superimposed control loop is the speed control. The block diagram of the speed control for LIM operation with the inner current control loop, which is modeled by the first-order equation (5.7), can be drawn as shown in the Figure 5.3. A position sensor was used to measure the position and then the speed is obtained by using derivative operations.

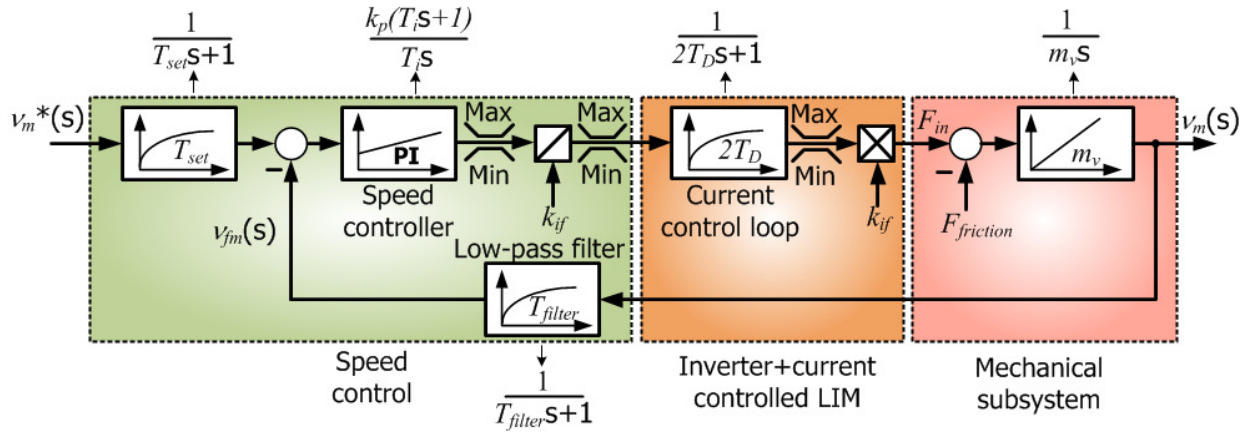


Figure 5.3: Block diagram of the speed loop for LIM operation.

The speed controller computes the difference between the reference speed $v_m^*$ and the speed feedback $v_{fm}$ generating an error, which is fed to a PI controller. Since the primary current $i_{1B}$ represents the LIM thrust force (equation 4.33) so that the speed PI controller output can be directly utilized as set point for the reference primary current $i_{1B}^*$.

From the block diagram of the speed control, the open-loop transfer function is:

$$F_{o,speed}(s) = \frac{k_p(T_i s+1)}{T_i s}\frac{1}{m_v s}\frac{1}{2T_D s+1}\frac{1}{T_{filter} s+1} \tag{5.14}$$

where: $T_{filter}$ is the low-pass feedback filter time constant.

The speed controller sees a pole ($2T_D$s+1) in the open-loop transfer function (Equation 5.14) that cannot be compensated by using the method presented before. Thereby, the symmetrical optimum method should be used to tune the speed PI controller parameters [56][84]. The speed feedback $v_{fm}$ is obtained at the output of the low-pass feedback filter block (see Figure 5.3), because it is essential to filter out the noise and the high-frequency content of actual mechanical speed $v_m$. The low-pass filter has a time constant of $T_{filter}$=12.5ms. For the feed-forward control, however, it is assumed that the speed measurement introduces no delays ($v_{fm}$= $v_m$).

The speed controller is an anti-windup PI compensator with current and thrust force limitation. Then, the integral time $T_i$ and gain $k_p$ of the speed PI controller are:

$$T_i = 4\left(2T_D + T_{filter}\right) \tag{5.15}$$

$$k_p = \frac{M_v}{2\left(2T_D + T_{filter}\right)} \tag{5.16}$$

To avoid a speed overshoot, a first-order low-pass reference filter with $T_{set}$=$T_i$ delay is used for the speed reference $v_m^*$, as shown in Figure 5.3. Finally, the designed speed PI controller together

with the mechanical transfer function can be modeled approximately as a first-order system, as depicted in (5.17).

$$F_{W,speed}(s) \approx \frac{1}{\underbrace{4\left(2T_D + T_{filter}\right)}_{T_{speed}} s + 1} \tag{5.17}$$

where: $T_{speed}$ is the equivalent time constant of the speed control loop.

### 5.1.4 Design of the speed controller for PMLSM operation

The block diagram of the speed control for PMLSM operation is similar to the speed control for LIM operation. The main difference is the thrust force constant $k_{if}$ and the limitations, since the PMLSM has a higher thrust force density. Hence, the block diagram is shown in Figure 5.4.

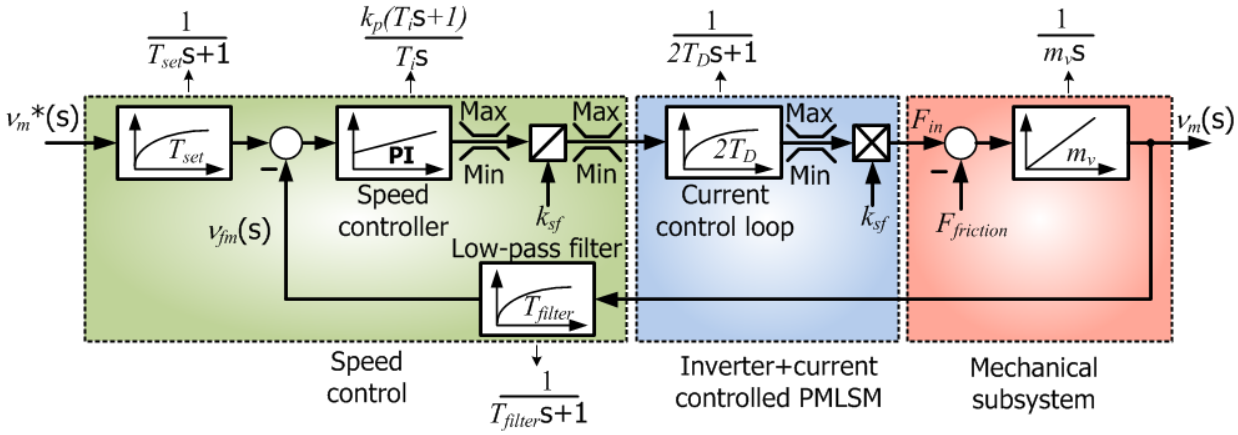


Figure 5.4: Block diagram of the speed loop for PMLSM operation.

With the structure above, the anti-windup PI controller parameters are tuned for symmetrical optimum, and they have the same parameters as presented in (5.15) and (5.16)

In each operation mode (LIM or PMLSM-FOC), the system has two controllers (speed and current) while just one position controller is used in both operation modes. The design of the position controller will be presented in the following.

### 5.1.5 Design of the position controller for both operations

In material handling systems, the electromagnetic thrust force is generated by the linear motor in order to control the position of the active vehicle. Moreover, within the processing section, the position overshoot is not allowed, since it could damage the material during the processing or result in collision of moving parts.

The outermost control loop in the cascade control is the position loop. It is responsible for controlling the reference position $x^*$ transmitted by the motion controller and calculating the reference speed $v_m^*$ which the system must assume in order to minimize the position error. From the point of view of the position controller, the speed controlled system looks approximately like a first-order system and an additional integrator. Furthermore, just a proportional controller is enough to control the vehicle position, since there is already an integrator in the control loop. The block diagram of the position control for both operations is shown in the Figure 5.5.

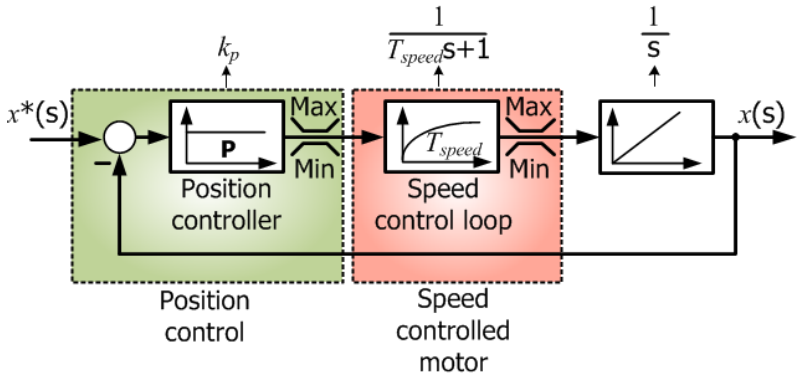


Figure 5.5: Block diagram of the position control loop for both operations.

The open-loop transfer function in the block diagram of the position control loop illustrated above is:

$$F_{o,speed}(s) = k_p \frac{1}{T_{speed}s+1}\frac{1}{s} \tag{5.18}$$

According to the amplitude optimum method, a unitary damping in the equivalent closed system is achieved when the gain $k_p$ of the position P controller is:

$$k_p = \frac{1}{4T_{speed}} \tag{5.19}$$

## 5.2. Transition control strategy

As explained in chapter 1, the passive track consists of two different section types (PM and induction rail), thus especially at the transition between synchronous and induction motor operation, a suitable transition control strategy is required to keep the speed constant.

### 5.2.1 Force generation when the vehicle is leaving a processing station

As shown in Figure 5.6, in the transition area a part of the primary acts like a synchronous and the other part as induction motor. Most of the phenomena which appear in such a situation in reality are not included in the classical and simple machine models used for control. As the primary winding is iron-cored, in reality there is a considerable reluctance force when only a part of the primary covers the magnets, as in Figure 5.6. This force exists without any current in a winding, but this is

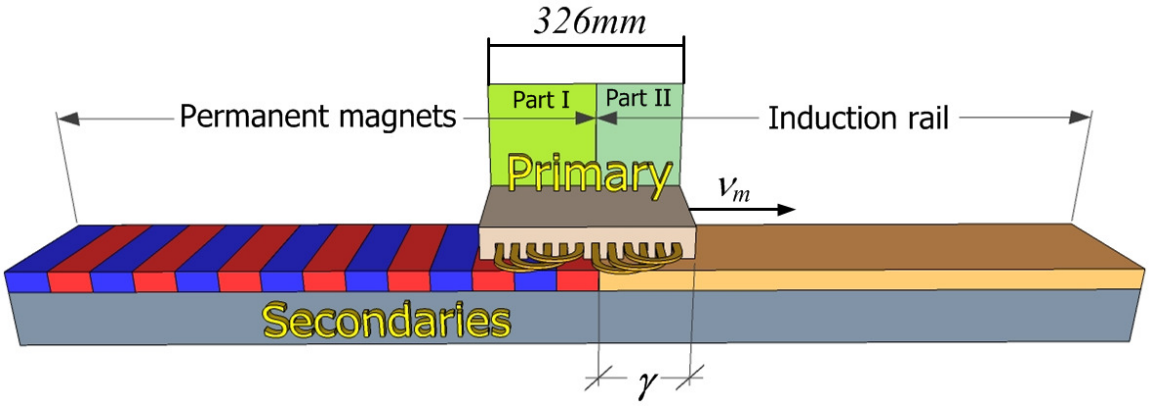


Figure 5.6: Transition area.

not reflected by the equations of the classical machine model. From this and many other reasons it is evident, that the classical machine models are not qualified to describe the situation shown in Figure 5.6. But as there are no analytical models (non- numerical models) for this situation available, the classical models are used here to give an approximate idea what might happen in this situation.

When the primary fully covers the magnets, then normal synchronous operation without any slip is applied in steady state, i.e. $\omega_2=\omega_{syn}-\omega_m=0$. Additionally, in synchronous operation the current component $i_{1A}$ is controlled to be zero ($i_{1A}=0$), whereas the current component $i_{1B}$ is controlled to generate the force $F_{sn}$ together with the permanent magnet flux $\Psi_{pm}$, as shown in Figure 5.7.

When the primary starts to leave the magnets, the amount of $\Psi_{pm}$ linked to the primary decreases, which decreases $F_{sn}$ accordingly. Additionally, the reluctance force due to the magnets and the primary's back iron builds up.

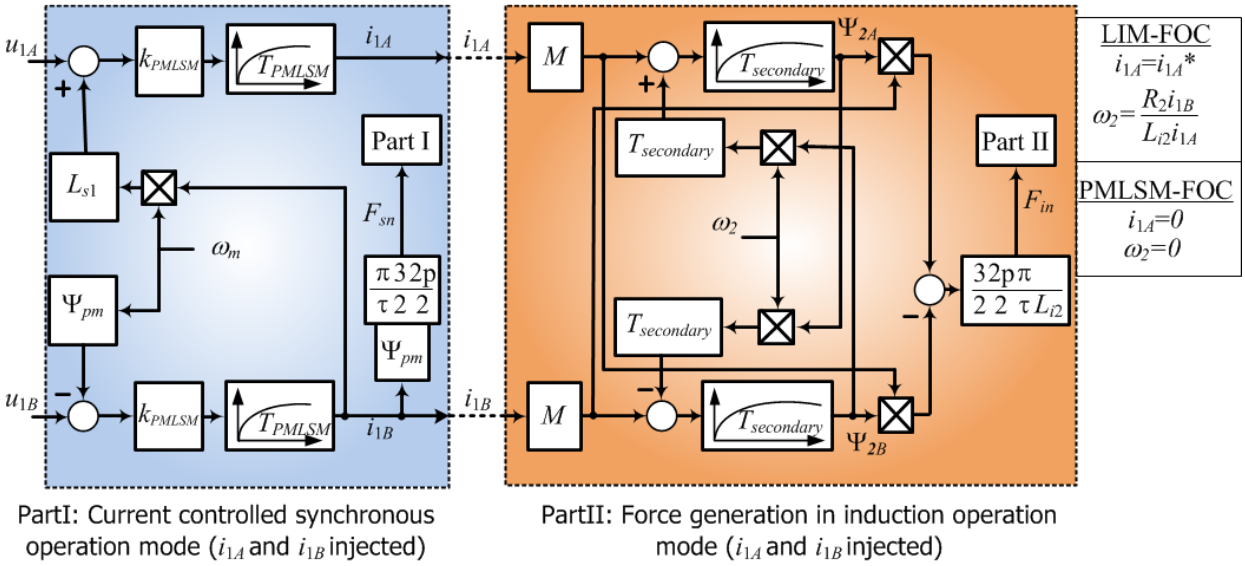


Figure 5.7: Thrust force generation.

The question is: what happens with part II of the primary, which covers the induction rail. The classical block diagram of force generation by an induction machine with injected stator currents and slip frequency $\omega_2$ is shown at the right-side of Figure 5.7. As long as the primary is operated in synchronous mode, $\omega_2$ is zero (no slip for synchronous operation) and the cross coupling between the secondary flux components $\Psi_{2A}$ and $\Psi_{2B}$ is zero too. As $i_{1d}=i_{1A}$ is controlled to be zero, $\Psi_{2A}$ is zero too ($\Psi_{2A}=0$). In order to generate the force $F_{sn}$ the current $i_{1q}=i_{1B}$ is controlled to be $i_{1B}=(4F_{sn}\tau)/(6p\Psi_{pm}\pi)$. Due to this, the steady state value of $\Psi_{2B}$ is $\Psi_{2B}=Mi_{1B}$. Under the assumption, that the classical block diagram for force generation in an induction machine can be used here, the force $F_{in}$ remains zero as long as $i_{1A}=\omega_2=0$.

When the vehicle reaches a predefined position $\gamma$(see Figure 5.6) the control mode is switched to field oriented control of an induction machine (LIM-FOC). From this instant on, force from the induction machine part should be provided. Typically, in base in speed range of FOC, the magnetizing flux is $\Psi_{2A}$ which is controlled by $i_{1A}$ (flux producing current) to its rated value. The flux $\Psi_{2B}$ is (open loop) controlled to zero by setting the secondary frequency to $\omega_2=(R_2i_{1B})/(L_{i2}i_{1A})$. The force is produced by the product of $\Psi_{2A}$ and $i_{1B}$ (force producing current). To start the machine,

the magnetizing flux $\Psi_{2A}$ has to be build up to its rated value. Normally designed induction machines (with laminated iron core) have a low secondary resistance $R_2$. This results in a large secondary time constant $T_{\text{secondary}}$. Therefore, changing the secondary flux components $\Psi_{2A}$ and $\Psi_{2B}$ needs a long time and is therefore avoided during (base speed) operation.

But when the vehicle reaches a predefined position $\gamma$ (see Figure 5.6), the initial values of the secondary flux components are just the opposite from what we need for typical FOC, as $\Psi_{2A}$ is zero while FOC needs it at its rated value and $\Psi_{2B}$ is a large value while FOC needs it to be zero.

The typical FOC may be applied in the very special case of a machine with a very large secondary resistance, i.e. a very short secondary time constant. Then, the transients when switching to rated magnetizing current $i_{1A}$ and the secondary frequency $\omega_2=(R_2 i_{1B})/(L_{i2} i_{1A})$ may be sufficient short to provide a smooth motion.

At the moment of the switching to LIM-FOC the part I still produces a very small fraction of the force $F_{sn}$ (positive in the direction of the motion), since the angle between the traveling field of the primary and the field of the magnets increases exceeds 90° and the area covering the magnets is reduced. On the other hand, the flux component $\Psi_{2B}$ is decaying to zero with a time constant of $T_{\text{secondary}}$, which produces a negative force $F_{in}=-(6p\pi M\Psi_{2B} i_{1A})/(4\tau L_{i2})$ in the part II. Besides this, the flux component $\Psi_{2A}$ increases with the same time constant $T_{\text{secondary}}$. During this short time interval, the vehicle's inertia keeps the vehicle moving in the same direction. Afterwards, the flux component $\Psi_{2B}$ reaches the zero value and only a positive force is generated in the part II.

The next question is: What happens with the part I of the machine, still covering the magnets? Due to the positive slip, the angle between the traveling field of the primary and the field of the magnets increases. When this angle exceeds 90°, then the force $F_{sn}$ decreases. When this angle exceeds 180°, then the force $F_{sn}$ becomes negative (breaking), which is of course is an unwanted disturbance. But this may happen, when only a small fraction of the primary covers the magnets. As only a small fraction of $\Psi_{pm}$ is linked with the primary, the disturbance may be small.

### 5.2.2 Force generation when the vehicle is entering a processing station

Here, the very special case of a machine with a very large secondary resistance is assumed. The primary is covering only the induction rail, at this point the LIM-FOC is active. The secondary frequency is $\omega_2=(R_2 i_{1B})/(L_{i2} i_{1A})$ to keep the flux component $\Psi_{2B}$ regulated to zero. Moreover, the magnetizing current $i_{1A}$ is controlled to $i_{1A}=(\Psi_{2A}^*/M)$, while the current component $i_{1B}$ controls the thrust force $F_{in}$.

When the primary is entering the magnets section, the primary starts to be attracted by the magnets and the thrust force initiates to decrease since the vehicle will not cover completely the induction rail. At this point, the induction operation (Part II) starts to break the vehicle ($i_{1B}^*$ is set to a negative value by the speed controller). The angle between traveling field of the primary and the field of the magnets is now higher than 180°, resulting in a negative force $F_{sn}$. Since a small fraction of the primary covers the magnets, the force generated $F_{sn}$ by the part I may be small, but it may increase as long as the vehicle enters in the processing section.

Now, the vehicle is located at the position $\gamma$ (see Figure 5.6) the control mode is switched to PMLSM-FOC and the thrust force should be furnished by the Part I. The secondary frequency $\omega_2$

and the reference value for $i_{1A}$* are set to zero. Then, the synchronous frequency is $\omega_{syn}=\omega_m$. As the secondary flux component $\Psi_{2A}$ decreases with a time constant of $T_{\text{secondary}}$, a force is produced by the part II with negative value ($i_{1B}$ is negative), thus the braking force at this moment is $F_{in}=-(6p\pi M\Psi_{2A}i_{1B})/(4\tau L_{i2})$. The speed must be kept constant, and then the current controller of the PMLSM-FOC injects positive current $i_{1B}$ in the B-axis to maintain the speed constant. However, until the flux component $\Psi_{2A}$ decays to zero, the part II produces a not controlled thrust force $F_{in}$ in the same direction of the thrust force generated by synchronous operation mode.

Finally, as long as $i_{1A}=\omega_2=0$, the cross coupling between the secondary flux components $\Psi_{2A}$ and $\Psi_{2B}$ is zero, thus the thrust force $F_{in}$ remains zero.

### 5.2.3 Transition control strategy block diagrams

Due to the two different operation modes and different secondary flux angles at the transition area (PMLSM→LIM) it is important to determine the position $\gamma$ (see Figure 5.6) where the switching of the FOC control modes should be changed. The best position $\gamma$ is found experimentally such that a sufficient thrust force with acceptable disturbance is reached. In other words, if the operation mode is changed too late from PMLSM-FOC to LIM-FOC, the thrust force required to guarantee a constant speed will not be achieved in the transition area.

For the synchronous operation, it is utilized only the *B*-axis current component $i_{1B}$, whereas in induction operation mode, both current components ($i_{1A}$ and $i_{1B}$) are injected. During the transition moment, the majority of the thrust force should be generated with the primary working in synchronous operation mode due to the fact that the induction operation requires more power and causes more power losses to keep the thrust force at the same level. Definitely, the LIM-FOC operation should be activated as late as possible. In face of that, the position value $\gamma$ was fixed taking such that the speed variation of the active vehicle was small.

Based on the criteria above, several experimental tests were carried out, and it was determined that the operation mode should be changed when the vehicle has 64% of its length above the induction rail, then the optimum position value is $\gamma \approx 209$mm.

The transition control strategy block diagrams with all the cascade control are shown in Figures 5.8 and 5.9. Figure 5.8 illustrates the active vehicle traveling within the processing station with PMLSM-FOC and Figure 5.8 shows the vehicle leaving the processing station, consequently, moving on the induction rail section with LIM-FOC. Depending on the position of the active vehicle, either the blocks for LIM-FOC (yellow area) or PMLSM-FOC (blue area) are activated. In each case, there are two inner closed current-loops. The *A*-axis current is controlled to keep the secondary flux constant (for synchronous operation $i_{1A}=0$ and induction operation $i_{1A}>0$), and the *B*-axis current $i_{1B}$ is controlled to adjust the electromagnetic thrust force. In each operation mode, the system has two controllers (speed and current) while the same position controller is used in both operation modes. The voltage source inverter switching signals are generated by the SV PWM block, as shown in Figures 5.8 and 5.9. For simplification, signals corresponding to limitation or the anti-windup of controllers are not drawn in Figures 5.8 and 5.9.

To start the linear motor FOC, the position signal feedback is necessary for orientation of the rotating *AB*- reference frame, and for the speed and position controllers. Within a processing station,

high accuracy is necessary. The position signal information is measured by a magneto-resistive incremental encoder (attached to the active vehicle), as show in Figures 5.8 and 5.9. A 3m-long linear magnetic scale was installed along the whole guidance profile covering the entire track. Due to this the actual position can always be measured. The light grey area in Figures 5.8 and 5.9 represents the control algorithm which was programmed in the DSP. During the transition period, the current $i_{1B}$ is regulated to brake or to accelerate the vehicle avoiding jerks.

#### 5.2.3.1 Active vehicle traveling within the processing station

When the vehicle is traveling on the permanent magnet section, the PMLSM-FOC is activated.

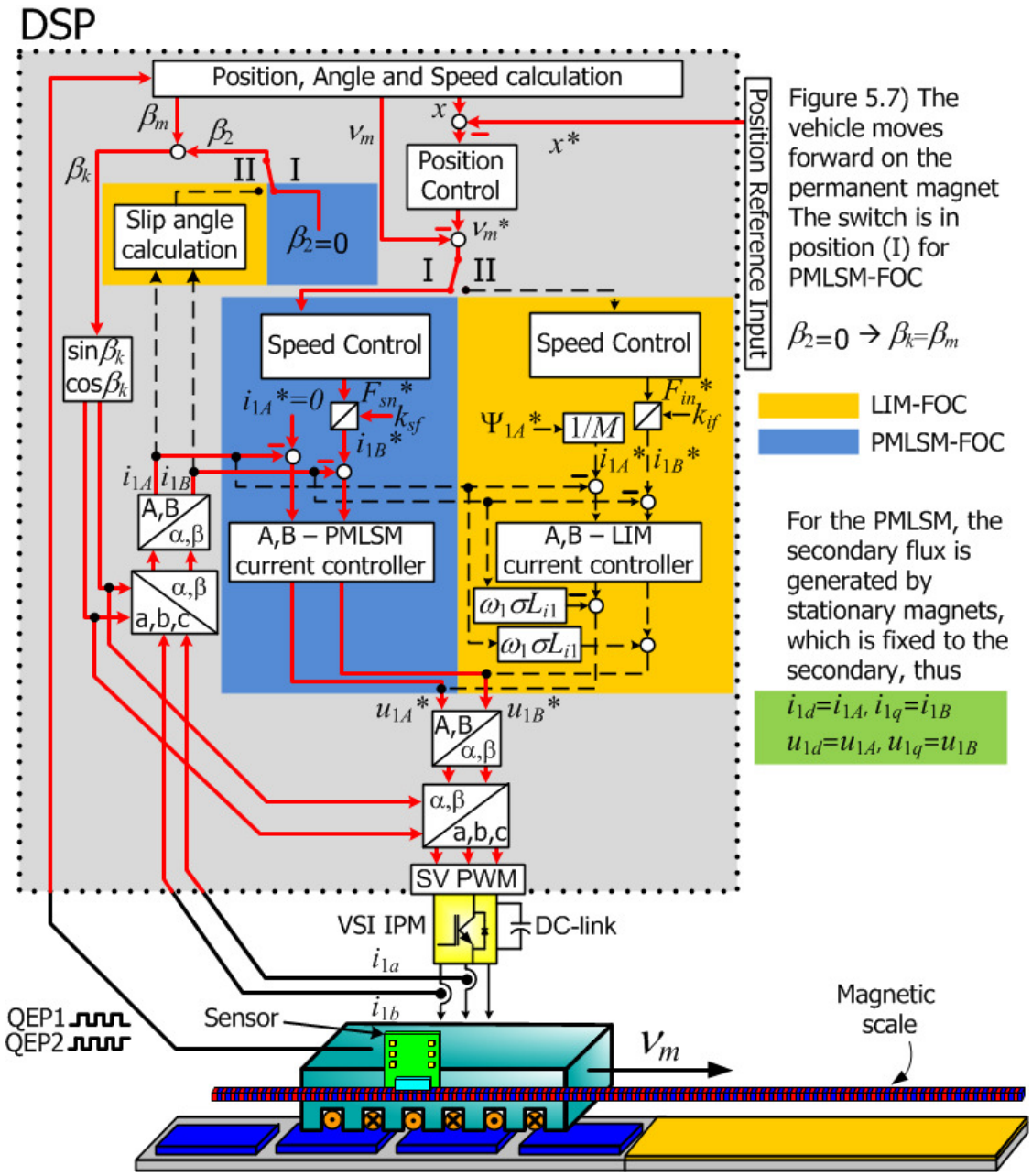


Figure 5.8: Transition control strategy block diagram when active vehicle is traveling within the processing station.

Then, the transition switch (I/II) is in position "I" (see Figure 5.8), the actual position and speed are calculated by the "Position, Angle, and Speed calculation" block, taking the information sent by the magneto-resistive incremental encoder with resolution of 200 increments per mm. Moreover, the slip angle $\beta_2$ is set to zero, and the current and speed controller uses the PMLSM parameters for the control loop. The angular position of the secondary utilized for orientation of the rotating *AB*-reference frame is $\beta_k=\beta_m$, as the secondary flux is electrically fixed to the secondary.

#### 5.2.3.2 Active vehicle traveling on the induction rail section

When the vehicle is leaving a processing section (PMLSM→LIM) and the vehicle has 64% of its

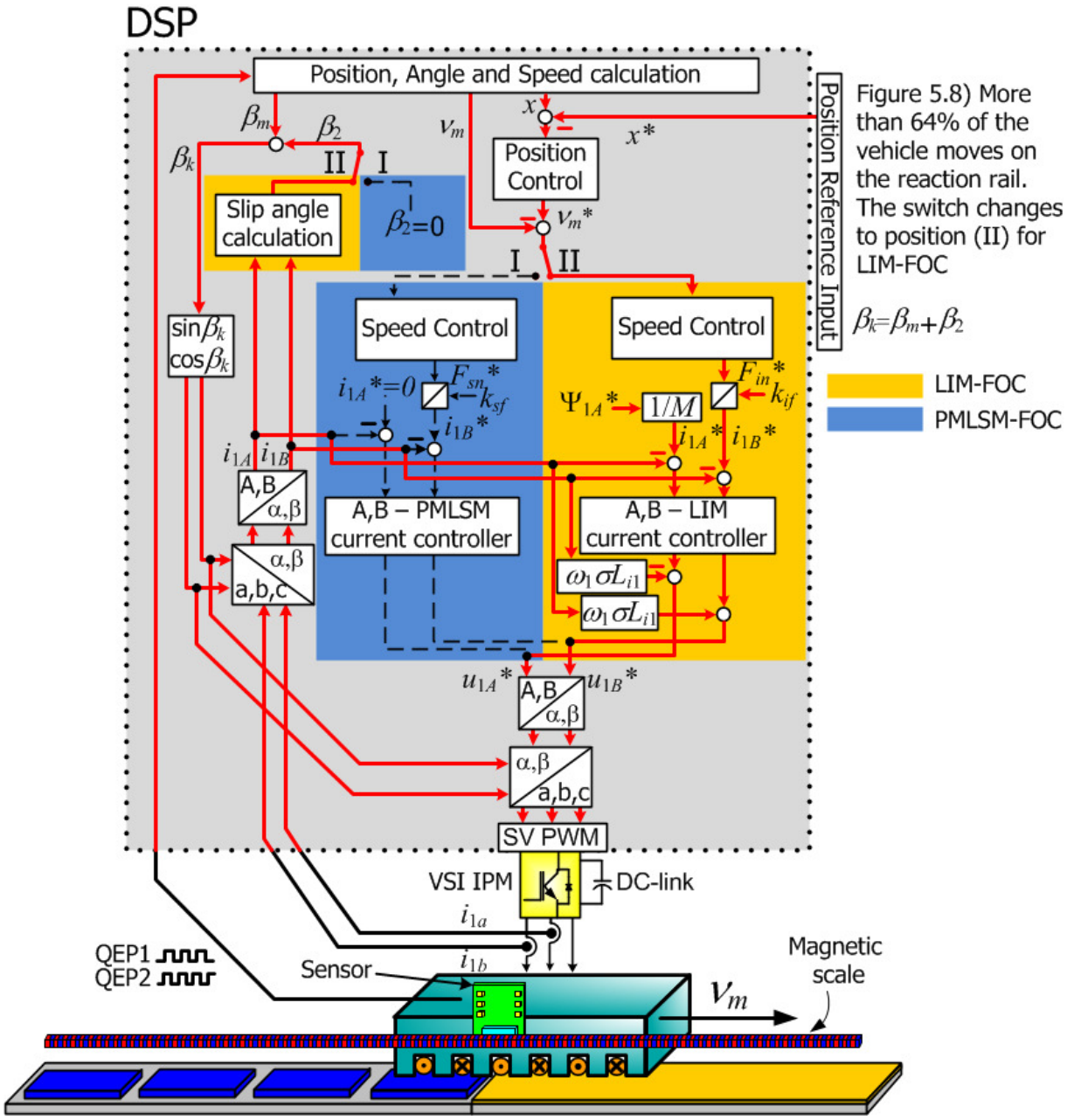


Figure 5.9: Transition control strategy block diagram when the active vehicle is moving on the induction rail section.

length above the induction rail, the switch changes to position "II", then the controller injects the magnetizing current $i_{1A}$ at the rated value and the slip angle $\beta_2$ is calculated using the measured currents $i_{1A}$ and $i_{1B}$, then the angular position of the secondary flux linkage is the sum of angles $\beta_k=\beta_m+\beta_2$. The LIM current and speed controller uses the induction linear motor parameters for the control loop, as shown in Figure 5.9.

At the border (PMLSM→LIM), the reluctance force of the stationary magnets becomes very high, thereby the force producing current $i_{1B}$ must be increased to avoid a speed drop. On the other hand, when the vehicle is entering a processing station (LIM→PMLSM), the control returns the switch to position "I". Unlike the "leaving" transition (PMLSM→LIM), the active vehicle is strongly attracted by the magnets increasing its speed. Therefore, the current $i_{1B}$ must be set to brake smoothly the active vehicle.

## 5.3. Transition control results

Out of the experimental results, the measured speed is the most important one, as its derivative (=acceleration) is the only quantity to get an idea which forces are acting on the vehicle. But unfortunately, there are severe restrictions in obtaining insight in the dynamic behavior of the forces. The incremental encoder measures the position. The speed is obtained by numerical derivation and filtering. This filter may hide transients in real speed and of course in acceleration (force). Additionally, the very high mass (53.7 kg) of the vehicle prevents that transients in force can be easily concluded from the recorded speed.

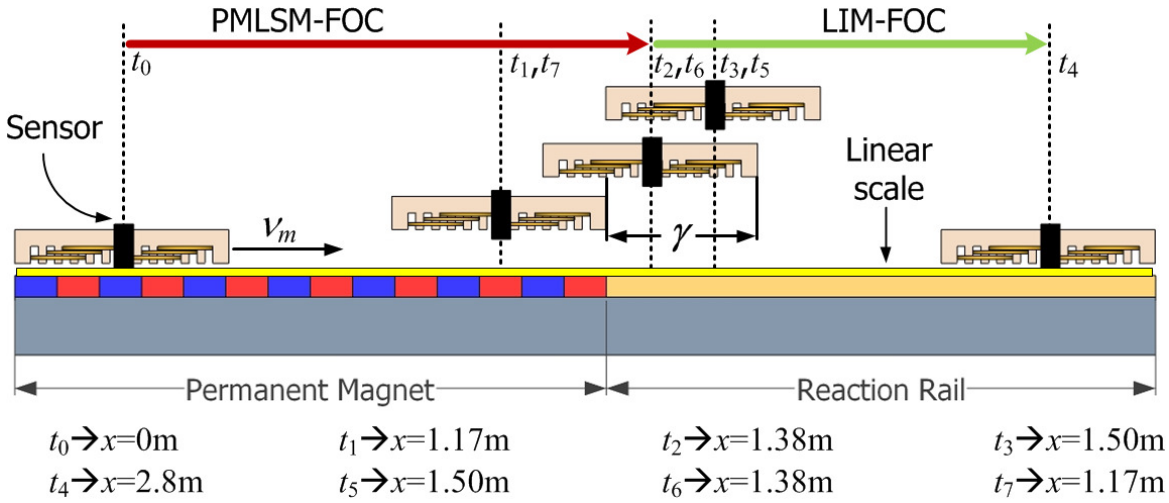


Figure 5.10: Sketch of the active vehicle position during the experimental drive cycle.

In order to test the position performance of the proposed control strategy, a position command ($x^*$=2.8m) was sent to the vehicle. The vehicle starts from the initial position ($x$=0m) on the processing station at time $t_0$, and reaches the transition area at the time $t_1$. Afterwards, the optimum position $\gamma$is achieved at time $t_2$, and at time $t_3$ the vehicle covers only the induction rail. At time $t_4$, the vehicle receives the new reference position ($x^*$=0m) and finally returns to the original position, as illustrated in Figure 5.10. For this experimental test, the speed was limited to 1m/s, the current $i_{1B}$ was limited to 8A and the magnetizing current was set to $i_{1A}$=3.6A.

During the drive, the active vehicle crosses both secondaries and returns to the original position. The experimental test was carried out in order to simulate a supposed situation where the vehicle leaves a processing station, but it needs to wait for the next processing station to be released. Then, it should stop for few seconds and move again toward the next processing station. At the border

Table 5.1 Description of the vehicle's actions during the drive cycle.

| Time | Position | Description | FOC | Required Thrust Force |
|---|---|---|---|---|
| $t_0$ | 0m | The vehicle accelerates, $i_{1B}>0$ and $i_{1A}=0$ | PMLSM | *positive, hard acceleration |
| $\Delta t_a=t_1-t_0$ | $\Delta x$=1.17m | The vehicle moves with constant speed $v_m$=1m/s | PMLSM | positive, constant |
| $t_1$ | 1.17m | The vehicle reaches the border, $i_{1B}>0$ and $i_{1A}=0$ | PMLSM | positive, soft acceleration |
| $\Delta t_a=t_2-t_1$ | $\Delta x$=0.21m | The reluctance force of the PM starts to increase and vehicle's speed drops. | PMLSM | positive, moderate acceleration |
| $t_2$ | 1.38m | The vehicle reaches the optimum position $\gamma$, $i_{1B}>0$ and $i_{1A}=3.6$A | PMLSM to LIM | positive, increasing |
| $\Delta t_b=t_3-t_2$ | $\Delta x$=0.12m | Current controller compensating the vehicle's speed. | LIM | positive, hard acceleration |
| $t_3$ | 1.50m | The vehicle covers completely the induction rail, $i_{1B}>0$ and $i_{1A}=3.6$A | LIM | *negative, soft braking |
| $\Delta t_c=t_4-t_3$ | $\Delta x$=1.30m | The vehicle moves with constant speed $v_m$=1m/s and stops at $x$=2.8m | LIM | constant and slowly brake until stop |
| $t_4$ | 2.80m | The vehicle had been stopped and prepares to return back, $i_{1B}>0$ and $i_{1A}=3.6$A | LIM | positive, hard acceleration |
| $\Delta t_d=t_5-t_4$ | $\Delta x$=1.30m | The vehicle moves with constant speed $v_m$=1m/s | LIM | positive, constant |
| $t_5$ | 1.50m | The vehicle reaches the border and prepares to brake, $i_{1B}<0$ and $i_{1A}=3.6$A | LIM | negative, reducing |
| $\Delta t_e=t_6-t_5$ | $\Delta x$=0.12m | The vehicle is attracted by the PM and vehicle's speed rises. | LIM | negative, hard braking |
| $t_6$ | 1.38m | The vehicle achieves the transition position, $i_{1B}<0$ and $i_{1A}=3.6$A | LIM to PMLSM | negative, reducing |
| $\Delta t_e=t_7-t_6$ | $\Delta x$=1.38m | The vehicle's speed increases, but is regulated by the current controller. | PMLSM | negative, soft braking |
| $t_7$ | 0.21m | The vehicle is completely within the PM section and moves to the end position, $i_{1B}>0$ and $i_{1A}=0$ | PMLSM | positive, increasing |

*positive=thrust force in the direction of the motion; *negative=thrust force opposite to the motion.

between both secondaries, there are some disturbances in the vehicle's speed that must be compensated by the current controller. Such disturbances are explained in details in the following subsections.

The vehicle's actions during the experimental drive cycle are described in Table 5.1. The speed, position and current responses for the executed experimental test are shown in Figure 5.11.

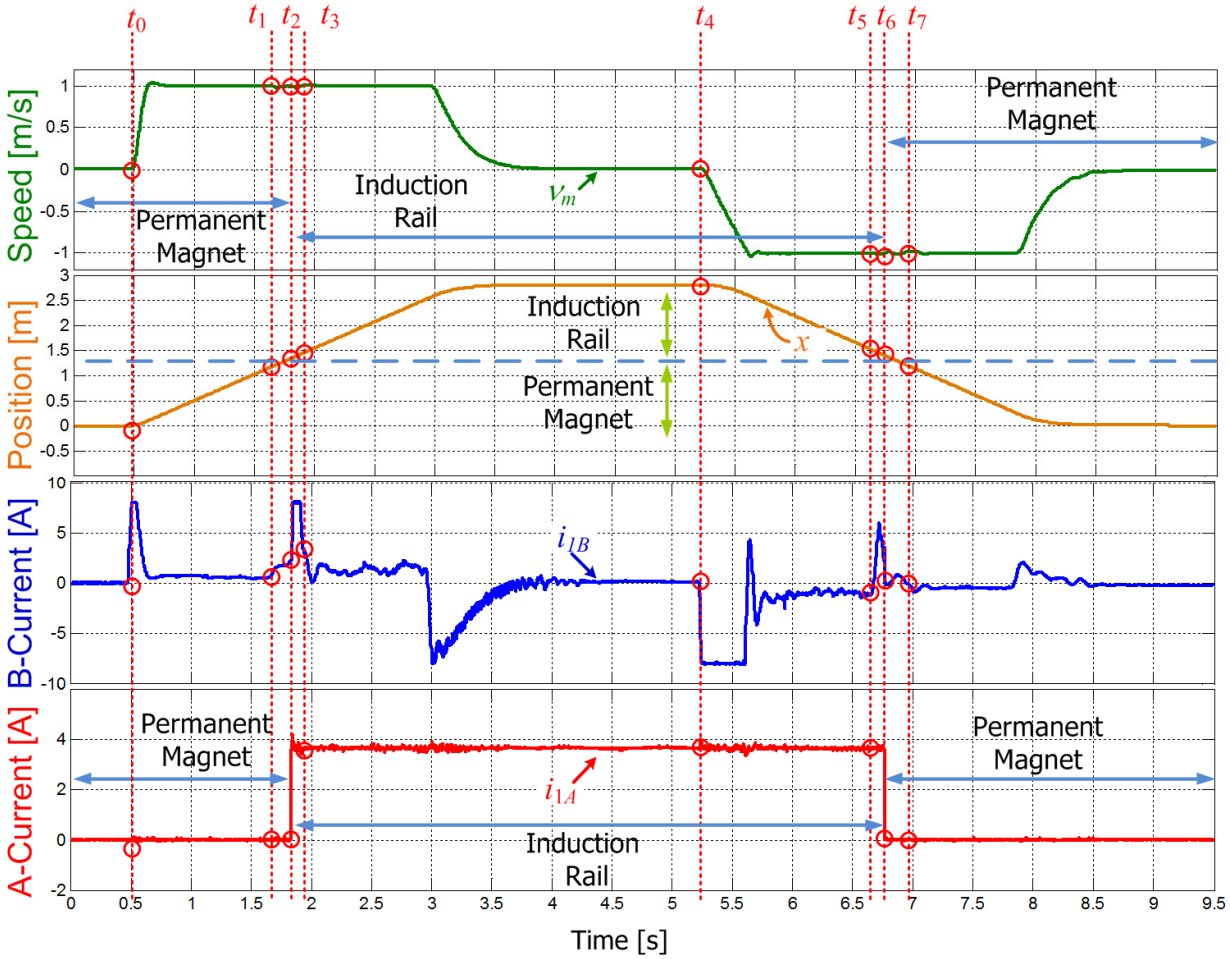


Figure 5.11: Measured position, speed and current for the drive cycle.

In order to obtain a better analysis of the speed disturbances and the current responses depicted in Figure 5.11 we will divide and describe the experimental drive cycle in two subsections: leaving a processing station (subsection 5.3.1) and entering a processing station (subsection 5.3.2). Afterwards, both parts in Figure 5.11 will be zoomed-in to give better insight of what happens during the transition.

### 5.3.1 Leaving a processing station

The first transition interval is zoomed-in in Figure 5.12. The control transition strategy starts the PMLSM-FOC operation at time $t_0$ with the vehicle within the processing station. When the position command is received, the vehicle moves forward 2.8m, with a controlled maximum speed of 1.0 m/s. At the time $t_1$, the vehicle is at the border of the magnet section and entering an induction

rail section, as shown in Figure 5.10. At this point, the reluctance force of the stationary magnets starts to increase slowly, dropping the vehicle speed, as illustrated in Figure 5.12c. Additionally, the area of the primary covering the magnets reduces. In the same way, the linked flux reduces. For the same force, this needs an increased current. To improve speed quality, a feed forward to the current reference signal proportional to the position could be used, but this was not implemented in the experiment. Part II of the primary generates no force in this situation.

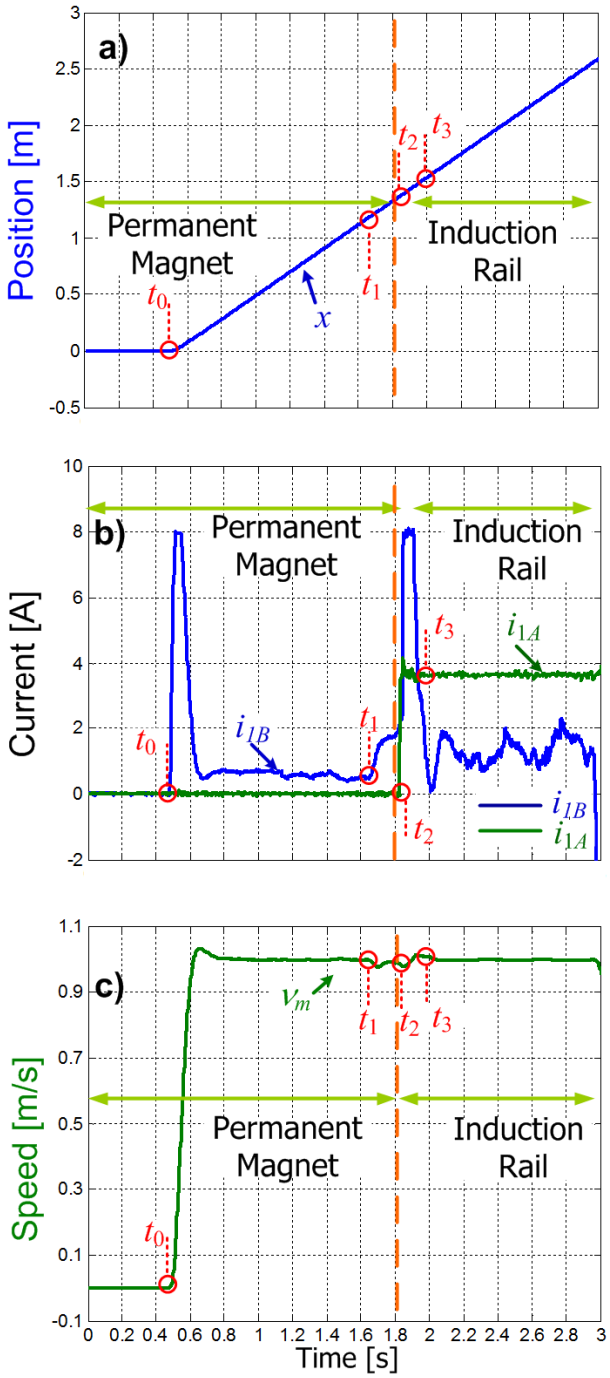


Figure 5.12: Position, speed and current responses when the vehicle is leaving a processing station: a) measured position; b) controlled currents in the *A*- and *B*- axis current; c) measured speed.

To compensate the vehicle speed drop, the current controller increases the thrust force through the current $i_{1B}$, as depicted in Figure 5.12b. When the vehicle is located at the optimum position $\gamma$, the LIM-FOC is started by changing the switch to position "II", at the time $t_2$. As the machine of the experimental setup has a high secondary resistance, the secondary time constant is small. In this experiment, the typical FOC is applied. This causes transients in torque, as initially, there is no flux in the secondary A-axis, and all the flux is in initially in the B-axis, which may produce even a negative force when the A-axis current is injected. But due to the short time constant, the transients may decay fast and due to the high mass of the vehicle, speed variations seem acceptable. Figure 5.12b shows that during the LIM-FOC the $i_{1B}$ current response, which compensates the high reluctance force, is higher than for PMLSM-FOC, since the LIM force constant ($k_{if}$) is around one-half of the PMLSM force constant ($k_{sf}$), as described in Table 3.2. Moreover, the LIM-FOC starts with the magnetizing current $i_{1A}$ being injected by the current controller, later the speed falls once again, as illustrated in Figure 5.12c. However, between the time $\Delta t_c = t_3 - t_2$, the vehicle speed drop is quickly compensated by the LIM current controller.

Finally, the vehicle covers only the induction rail ($t_3$), thereafter the reluctance force falls to zero, increasing the vehicle speed, as depicted in Figure 5.12c. After leaving the transition area, the current values were kept approximately constant to maintain the vehicle speed at 1.0 m/s. The vehicle has left the processing station and moves with low thrust force through the transport section, towards the next processing station.

### 5.3.2 Entering a processing station

The transition interval during which the vehicle enters a processing section is zoomed in Figure 5.13. With the active vehicle inside the transporting section, a step in the position reference is given by the stationary central motion controller and the vehicle starts to accelerate. The control operates in LIM-FOC mode. Thereby, the active vehicle moves in the opposite direction and achieves the border of the induction rail section at time $t_5$, as illustrated in Figure 5.10.

At time $t_5$, the active vehicle begins to be attracted by the stationary magnets, and then the vehicle speed is increased (in negative direction), as shown in Figure 5.13c. Afterwards, the current controller starts to brake the vehicle smoothly (positive $i_{1B}$ current). This force produced to brake the vehicle is generated mainly by Part II. During the braking, the generated energy is absorbed by the ultracapacitor energy storage system. When the vehicle has 36% of its length within the processing section, the switch changes to position "I", the magnetizing current $i_{1A}$ becomes zero, and the PMLSM-FOC is initiated. As the PMLSM thrust force is higher than the LIM, the current $i_{1B}$ rapidly falls, as illustrated in the Figure 5.13b.

At time $t_6$, the speed rises again, since an uncontrolled fraction of the force (positive force in the direction of the motion) is generated by the Part II of the vehicle, until the flux component $\Psi_{2A}$ decays to zero, this force is added to the force produced by the Part I (positive force in the direction of the motion). Afterwards, the PMLSM current controller tries to compensate this speed braking the active vehicle between the time $\Delta t_e = t_7 - t_6$, as depicted in Figure 5.13b. At last, the vehicle covers only the processing section at time $t_7$. The vehicle speed drop for the given position occurs due to the

$i_{1B}$ current shifting from positive (braking) to negative (driving) value. Hence, the active vehicle speed is controlled at 1.0 m/s until the end of the drive cycle.

With all results presented From Figures 5.12 and 5.13 it can be seen that the speed was kept constant, without jerks. There were only small speed disturbances (less than 3% of speed drop) at the border.

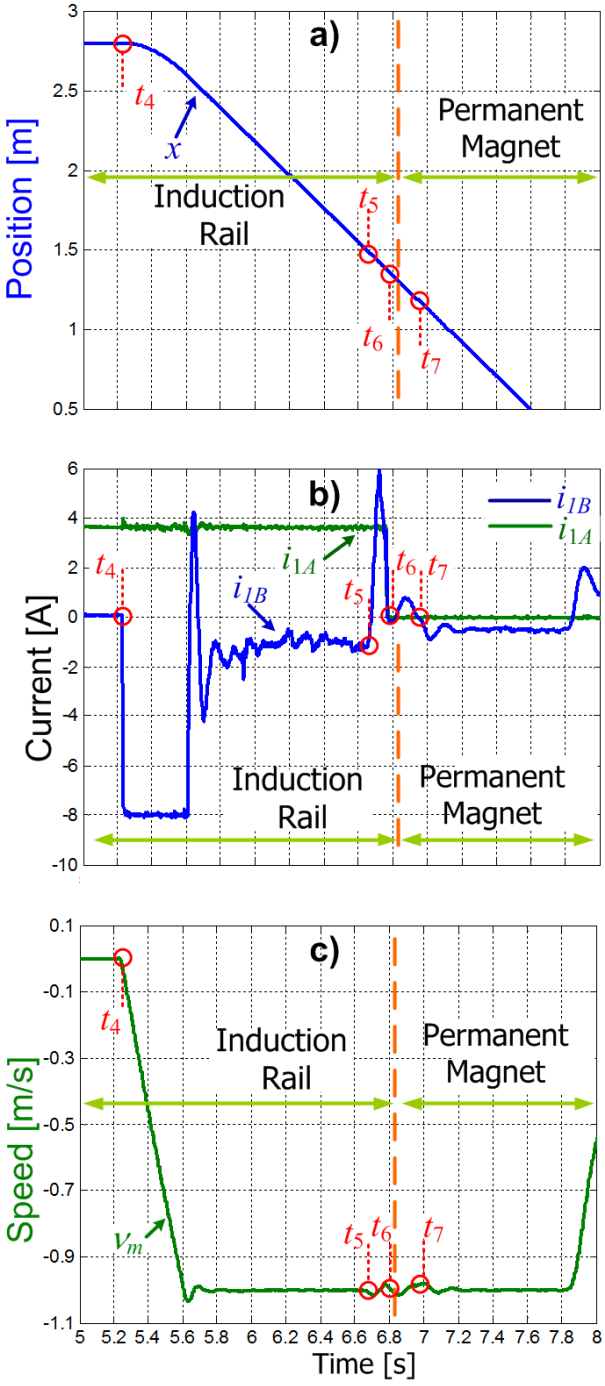


Figure 5.13: Position, speed and current responses when the vehicle is entering a processing station: a) measured position; b) controlled currents in the *A*- and *B*- axis current; c) measured speed.

# 6. Sensorless Transition Control Strategy

As described in Chapter 1, at the transporting section the sensorless motion control may be used in order to reduce de cost of the linear magnetic scale for very long track applications. In this chapter, the principle of sensorless operation, the control algorithm employed to estimate the secondary flux angle and the speed, the practical problems and constraints involved, and their solutions are presented. In addition, the sensorless flux and speed estimators based on the standard rotating induction machines are discussed. Finally, the experimental setup is used to check the speed tracking results and to show the performance of the control system.

## 6.1. Sensorless field oriented control

For rotary motors, it is required only one encoder on the shaft, but for a linear motor, the position sensor is installed along the track, increasing the costs proportionally to the length and the complexity. Therefore, position sensorless operation in linear motor applications is more important than in rotary motor applications.

Focusing on our application, we will ignore the position signal feedback required for orientation of the rotating *AB*- reference frame and for the speed and position controllers, when the active vehicle travels above the induction rail.

In the literature several techniques have been proposed to obtain the secondary position of an electrical machine, and they can generally be classified in two main categories:

- Estimation of the EMF or the secondary flux, which is based on the fundamental field model of the motor [85][86][87].
- Injection of a high-frequency signal carrier on a salient motor, which is based on the tracking of the high-frequency magnetic saliency produced by the magnetic saturation (main flux or leakage flux saturation) [88][89][90][91].

The first technique loses performance as the speed decreases, and does not work at standstill, because the EMF is proportional to the secondary's speed [85][86][87]. The second method is more complex, and in some cases it requires extra components (filters)[90], but it gives reasonable thrust force controllability at very low or zero speed [88][89][91].

Considering that the vehicle will not travel at very low speeds within the transporting section, the sensorless method utilized in this thesis will be based on the estimation of the secondary flux or EMF. Since the linear scale, which is installed inside the processing section, is shortly extended above the induction rail, the vehicle is able to stop and wait in case of the next processing station should be in use, as shown in Figure 6.1.

From various approaches of sensorless flux and speed estimation [85][86][92][93][94], we can select between open or closed-loop speed and flux estimators. The open-loop estimator depends strongly on the accuracy of the machine parameters, e.g. the primary and secondary resistances. However, in closed-loop estimators, the accuracy can be improved [85][92][93]. Therefore, from

all closed-loop estimators, the most promising and robust estimators against model parameter's variations seem to be the model reference adaptive system (MRAS) for speed estimation and the closed-loop secondary flux observer or estimator for the flux estimation [86][94].

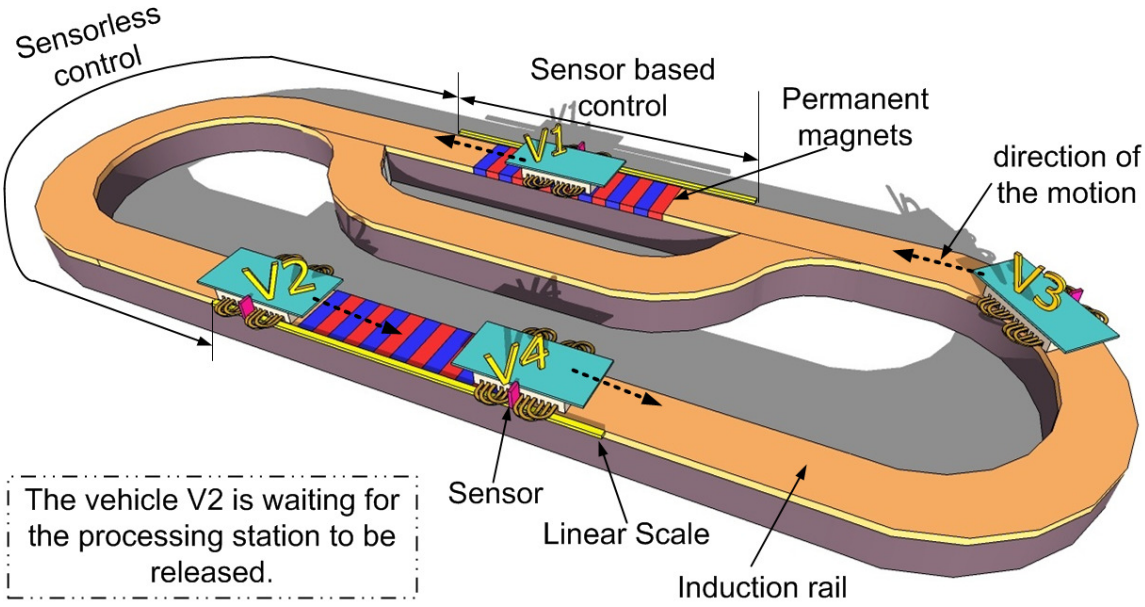


Figure 6.1: Sketch of a material handling application with linear drive and an extended linear scale.

The MRAS speed estimator uses a reference model compared with the output of an adaptive model to estimate the same state variables and then the actual error between both output variables is applied to a PI compensator, which produces the estimated variable used in the adaptive model. The reference model uses the voltage model (which does not include the estimated speed), while an adjustable current model (which includes the estimated speed) is employed by the adaptive model.

As the inverter feeds the machine with pulse-modulated voltages, and only the low frequency content of this pulsed voltage is useful for the estimation, the reference signal at the input of the modulator is used for estimation. But there are systematic deviations between the low frequency content of the pulse-modulated voltages and its reference signal. The most important one is the interlock time (also called dead time) necessary for save switching the power-semiconductors. Hence, the dead-time compensation is indispensable for accurate flux and speed estimations, especially at low speeds [96][97]. Such compensation will be explained further.

### 6.1.1 Dead-time compensation

Since the turn-on and turn-off times of an IGBT are not the same, it is necessary to add a time delay (dead-time) between each PMW signal, in order to avoid a short circuit, which would occur if both IGBT are turned-on at the same time. The dead-time values depend on the switching devices. For sensorless applications, such values should be as low as possible; because it causes errors in the applied fundamental voltage, reducing the output voltage and distorting the motor current.

The IPM module used in our VSI board requires a minimum dead-time of 3.3µs. The DSP algorithm was implemented with $T_{dead}$=3.4µs of dead-time. It was observed that this value is large and causes a voltage drop of approximately ±20V.

The dead-time compensation has been widely investigated and different solutions are presented. Basically, these solutions can be classified in two main categories:

- Compensation of the dead-time error in each PWM pulse [95].
- Compensation of the averaged voltage error [98].

It was adopted the compensation method presented in [95], to adjust the dead-time errors, since the given method is recommended by the DSP's manufacturer [99] and uses a minimal number of software code lines.

In the chosen method, the PWM pulses are independently modifiable in each PWM period ($T_{sample}$) in the DSP algorithm, as shown in Figure 6.2. That means the dead-time compensator can update the turn-on time at the beginning of the PWM period and another update can be made in the middle of the PMW period. Also illustrated in Figure 6.2 the output of the SV PWM is corrected based on the current polarity.

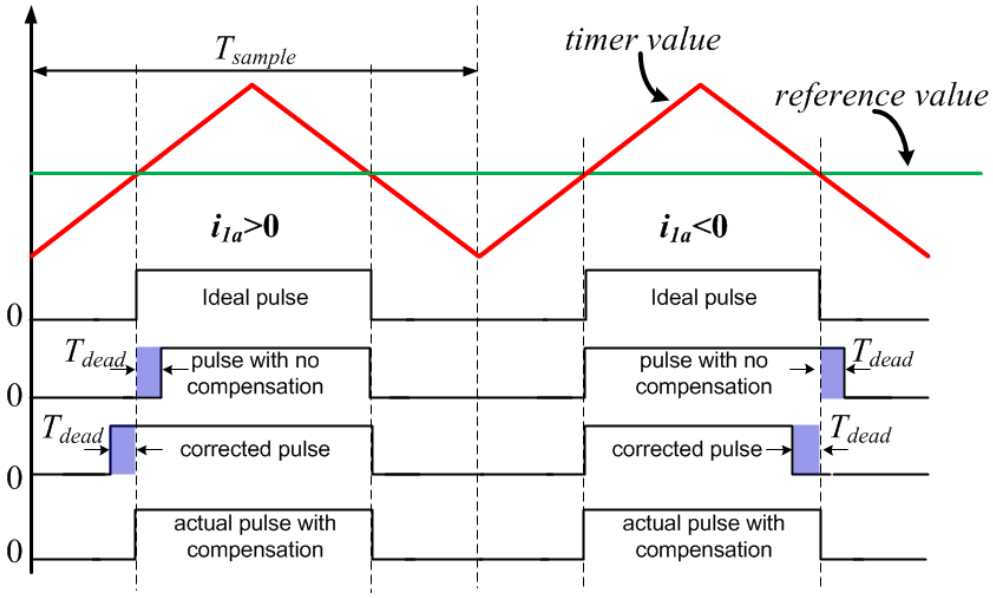


Figure 6.2: Dead-time compensation. [95]

In summary, the dead-time compensation method changes the rising edge and falling edge of ideal pulses by adding or subtracting the preset dead-time value ($T_{dead}$) from them, reducing the dead-times effects. The block diagram of the dead-time compensation using the F2812 DSP is described in appendix B.5. Finally by using the dead-time compensation, the primary reference voltages $u_{1A,B}$* are used in the flux and speed estimators, i.e., the primary voltages $u_{1A,B}$ are assumed to be equal their references.

### 6.1.2 Flux and speed estimators

Along the transporting section, sensorless methods should be used for estimation of the angular position of the secondary. The speed and flux estimators are based on rotating induction machines. For the sensorless operation, the angular position of the secondary flux $\beta_k$ is provided by the flux estimator.

### 6.1.2.1 Flux estimator

The flux estimator used to calculate the estimated secondary flux linkage from a closed-loop system, uses the $\alpha\beta$- stationary reference frame. The flux estimator block diagram is shown in Figure 6.3 [93].

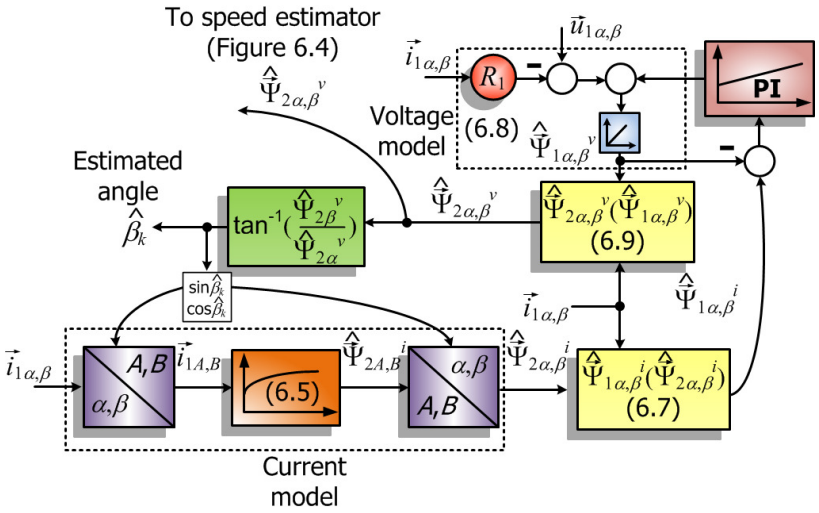


Figure 6.3: Block diagram of the flux estimator [93].

The LIM voltage equations (4.6) and (4.7), the flux linkages (4.10) and (4.11) in the $\alpha\beta$- stationary reference frame are:

$$u_{1\alpha} = R_1 i_{1\alpha} + \frac{d\Psi_{1\alpha}}{dt}$$
$$u_{1\beta} = R_1 i_{1\beta} + \frac{d\Psi_{1\beta}}{dt} \tag{6.1}$$

$$u_{2\alpha} = R_2 i_{2\alpha} + \frac{d\Psi_{2\alpha}}{dt} - \omega_m \Psi_{2\alpha} = 0$$
$$u_{2\beta} = R_2 i_{2\beta} + \frac{d\Psi_{2\beta}}{dt} + \omega_m \Psi_{2\alpha} = 0 \tag{6.2}$$

$$\Psi_{1\alpha} = L_{i1} i_{1\alpha} + M i_{2\alpha} \rightarrow i_{1\alpha} = \frac{1}{\sigma L_{i1}} \Psi_{1\alpha} - \frac{M}{\sigma L_{i1} L_{i2}} \Psi_{2\alpha}$$
$$\Psi_{1\beta} = L_{i1} i_{1\beta} + M i_{2\beta} \rightarrow i_{1\beta} = \frac{1}{\sigma L_{i1}} \Psi_{1\beta} - \frac{M}{\sigma L_{i1} L_{i2}} \Psi_{2\beta} \tag{6.3}$$

$$\Psi_{2\alpha} = M i_{1\alpha} + L_{i2} i_{2\alpha} \rightarrow i_{2\alpha} = \frac{1}{L_{i2}} \left( \Psi_{2\alpha} - M i_{1\alpha} \right)$$
$$\Psi_{2\beta} = M i_{1\beta} + L_{i2} i_{2\alpha} \rightarrow i_{2\beta} = \frac{1}{L_{i2}} \left( \Psi_{2\beta} - M i_{1\beta} \right) \tag{6.4}$$

where: the subscripts "$\alpha$, $\beta$" denote the quantities in the $\alpha\beta$- stationary reference frame,
$\omega_m$ is the mechanical angular speed.

The flux estimator has a current model and an adaptive voltage model. The current model is the reference model and is dominant at low speed range; instead the voltage model has more influence for wide speed range, only if a very poor position sensor is used. The voltage model depends on the

reference voltages ($u_{1\alpha}$*, $u_{1\beta}$*) and actual currents ($i_{1\alpha}$, $i_{1\beta}$) and the current model uses the actual primary current and the estimated angular position of the secondary flux $\hat{\beta}_k$ to produce an estimated secondary flux. The transition between both models is made by a PI compensator, as shown in Figure 6.3.

Using the expressions (4.28) and $\Psi_{2B}$=0, the estimated secondary flux linkage current model (superscript "*i*") in rotating *AB*- reference frame can be written as:

$$\begin{aligned} \hat{\Psi}_{2A}{}^{i} &= \frac{M}{\left(1+sT_{secondary}\right)i_{1A}} \\ \hat{\Psi}_{2B}{}^{i} &= 0 \end{aligned} \tag{6.5}$$

where: All quantities marked with "^" denote estimated quantities.

The current model is utilized in rotating *AB*- reference, since the coordinate transformation plays a role in the input decoupling and removes the speed as input value, which can lead to instability problems [100].

Arranging a coordinate system conversion of (6.5) to the $\alpha\beta$- stationary reference frame, by using the inverse transformation matrix $[T_{AB}]^{-1}$ (see appendix B.2), the estimated fluxes are:

$$\begin{aligned} \hat{\Psi}_{2\alpha}{}^{i} &= \hat{\Psi}_{2A}{}^{i}\cos(\hat{\beta}_k) \\ \hat{\Psi}_{2\beta}{}^{i} &= \hat{\Psi}_{2A}{}^{i}\sin(\hat{\beta}_k) \end{aligned} \tag{6.6}$$

With the primary currents in (6.3), the estimated primary flux $\hat{\Psi}_{1\alpha,\beta}{}^{i}$ can be determined, as follows:

$$\begin{aligned} \hat{\Psi}_{1\alpha}{}^{i} &= \frac{M}{L_{i2}}\hat{\Psi}_{2\alpha}{}^{i} + \sigma L_{i1} i_{1\alpha} \\ \hat{\Psi}_{1\beta}{}^{i} &= \frac{M}{L_{i2}}\hat{\Psi}_{2\beta}{}^{i} + \sigma L_{i1} i_{1\beta} \end{aligned} \tag{6.7}$$

The reference model also determines the primary flux through a feedback system using a voltage model (superscript "*v*"), where the primary flux estimation $\hat{\Psi}_{1\alpha,\beta}{}^{i}$ is the feedback variable, as shown in Figure 6.3. Using the feedback from a PI compensator, the difference between the estimated values of (6.7) and (6.8) is controlled to be small.

$$\begin{aligned} \hat{\Psi}_{1\alpha}{}^{v} &= \frac{1}{s}\left(u_{1\alpha} - R_1 i_{1\alpha} - \left(k_1 + \frac{k_2}{s}\left(\hat{\Psi}_{1\alpha}{}^{v} - \hat{\Psi}_{1\alpha}{}^{i}\right)\right)\right) \\ \hat{\Psi}_{1\beta}{}^{v} &= \frac{1}{s}\left(u_{1\beta} - R_1 i_{1\beta} - \left(k_1 + \frac{k_2}{s}\left(\hat{\Psi}_{1\alpha}{}^{v} - \hat{\Psi}_{1\beta}{}^{i}\right)\right)\right) \end{aligned} \tag{6.8}$$

where: $k_1$ is the proportional gain for the flux PI compensator,
$k_2$ is the integral gain for the flux PI compensator.

This PI compensator is utilized to correct the pure integrator errors and small resistance variations at low speed and provides a wide speed range operation [92][93]. The method to determine the gains of the estimator, as well as a dynamic analysis is given in [100].

The selection of gains $k_1$ and $k_2$ is limited to the error between the estimated and actual angular position of the secondary flux ($\Delta\beta_k = \hat{\beta}_k - \beta_k$). The error $\Delta\beta_k$ should be less than 30 degrees. In case

of a higher error, the field orientation will be lost, thus the equation (4.34) is not longer valid and thrust force is drastically reduced.

Using the primary currents in (6.3), the final reference model secondary flux is calculated from the primary flux estimation $\hat{\Psi}_{1\alpha,\beta}{}^{v}$ in (6.8) and the primary currents, hence:

$$\begin{aligned}\hat{\Psi}_{2\alpha}{}^{v} &= \frac{L_2}{M}\hat{\Psi}_{1\alpha}{}^{v} - \frac{\sigma L_1 L_2}{M} i_{1\alpha} \\ \hat{\Psi}_{2\beta}{}^{v} &= \frac{L_2}{M}\hat{\Psi}_{1\beta}{}^{v} - \frac{\sigma L_1 L_2}{M} i_{1\beta}\end{aligned} \tag{6.9}$$

Finally, the estimated angular position of the secondary flux $\hat{\beta}_k$ in relation to the $\alpha$-axis of the $\alpha\beta$-stationary reference frame is defined as follows:

$$\hat{\beta}_k = \tan^{-1}\left(\frac{\hat{\Psi}_{2\beta}{}^{v}}{\hat{\Psi}_{2\alpha}{}^{v}}\right) \tag{6.10}$$

### 6.1.2.2 Speed estimator

The MRAS speed estimator used to estimate the vehicle's speed and the position is shown in Figure 6.4.

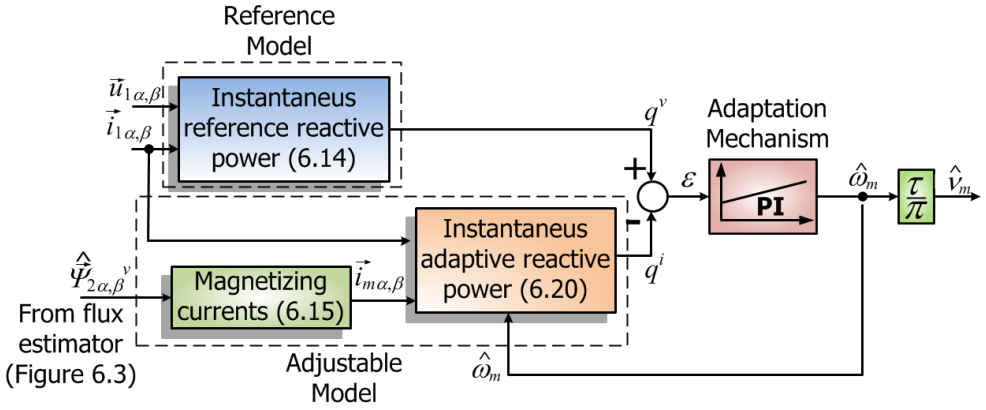


Figure 6.4: Block diagram of the MRAS speed estimator. [101]

The main advantage of this method is the utilization of the instantaneous reactive power of the secondary flux. Therefore, it does not require the primary resistance and any pure integrator, avoiding DC-offset problems and as a result increases the robustness. However, it becomes unstable when the speed is near to stand still [86][101].

By using (6.3), the secondary flux linkages ($\Psi_{2\alpha}$ and $\Psi_{2\beta}$) can be expressed in terms of primary flux linkages ($\Psi_{1\alpha}$ and $\Psi_{1\beta}$), then:

$$\begin{aligned}\Psi_{2\alpha} &= \frac{L_{i2}}{M}\left(\Psi_{1\alpha} - \sigma L_{i1} i_{1\alpha}\right) \\ \Psi_{2\beta} &= \frac{L_{i2}}{M}\left(\Psi_{1\beta} - \sigma L_{i1} i_{1\beta}\right)\end{aligned} \tag{6.11}$$

With the derivative of equations (6.11), and inserting (6.1), we get (6.12) which is the voltage back-EMF ($e_{1\alpha}{}^{v}$ and $e_{1\beta}{}^{v}$) for the reference model depicted in Figure 6.4.

$$\underbrace{\frac{d\Psi_{2\alpha}}{dt}\frac{M}{L_{i2}}}_{e_{1\alpha}{}^{v}} = u_{1\alpha} - R_1 i_{1\alpha} - \sigma L_{i1}\frac{di_{1\alpha}}{dt}$$
$$\underbrace{\frac{d\Psi_{2\beta}}{dt}\frac{M}{L_{i2}}}_{e_{1\beta}{}^{v}} = u_{1\beta} - R_1 i_{1\beta} - \sigma L_{i1}\frac{di_{1\beta}}{dt} \tag{6.12}$$

From the above equation, it can be seen that the voltage Back-EMF is the difference between the primary voltage and the sum of the voltage drop across the primary resistance and across the transient inductance. The instantaneous reference reactive power $q^v$ for a rotating induction machine is the cross product of the voltage back-EMF and the primary current vectors, which removes the integral calculation and the dependence on the primary resistance. That is:

$$q^v = \vec{i}_{1\alpha,\beta} \otimes \vec{e}_{1\alpha,\beta}{}^{v}$$
$$q^v = \vec{i}_{1\alpha,\beta} \otimes \left( \vec{u}_{1\alpha,\beta} - R_1 \vec{i}_{1\alpha,\beta} - \sigma L_{i1}\frac{d\vec{i}_{1\alpha,\beta}}{dt} \right) \tag{6.13}$$

where: $\otimes$ denotes the cross product of vectors.

As $\vec{i}_{1\alpha,\beta} \otimes \vec{i}_{1\alpha,\beta} = i_{1\alpha} i_{1\beta} - i_{1\beta} i_{1\alpha} = 0$, then:

$$q^v = i_{1\alpha} u_{1\beta} - i_{1\beta} u_{1\alpha} + i_{1\beta}\sigma L_{i1}\frac{di_{1\alpha}}{dt} - i_{1\alpha}\sigma L_{i1}\frac{di_{1\beta}}{dt} \tag{6.14}$$

From the equation above you can see that primary resistances were canceled out. For this reason, the given model is not sensitive to parameter variation. However, the noise level is increased due to the derivative of the primary current which must be computed in (6.14).

Similarly to (4.29), the magnetizing current in the $\alpha\beta$-stationary frame is defined as:

$$i_{m\alpha} = \frac{\Psi_{2\alpha}}{M} \approx \frac{\hat{\Psi}_{2\alpha}{}^{v}}{M}$$
$$i_{m\beta} = \frac{\Psi_{2\beta}}{M} \approx \frac{\hat{\Psi}_{2\beta}{}^{v}}{M} \tag{6.15}$$

where: $i_m$ is the magnetizing current.

Inserting the (6.15) in the voltage back-EMF ($e_{1\alpha}{}^{v}$ and $e_{1\beta}{}^{v}$) depicted in (6.12), we get the back-EMF ($e_{1\alpha}{}^{i}$ and $e_{1\beta}{}^{i}$) for the adjustable model.

$$e_{1\alpha}{}^{i} = \frac{M}{L_{i2}}\frac{d\Psi_{2\alpha}}{dt} = \frac{M^2}{L_{i2}}\frac{di_{m\alpha}}{dt}$$
$$e_{1\beta}{}^{i} = \frac{M}{L_{i2}}\frac{d\Psi_{2\beta}}{dt} = \frac{M^2}{L_{i2}}\frac{di_{m\beta}}{dt} \tag{6.16}$$

Similarly to (4.26) and (4.27) and setting $\nu_1$=0, the derivative of the secondary flux in the $\alpha\beta$-stationary frame is defined as:

$$\frac{d\Psi_{2\alpha}}{dt} = \frac{1}{T_{secondary}}\left( M i_{1\alpha} - \Psi_{2\alpha} - \omega_m \Psi_{2\beta} T_{secondary} \right)$$
$$\frac{d\Psi_{2\beta}}{dt} = \frac{1}{T_{secondary}}\left( M i_{1\beta} - \Psi_{2\beta} + \omega_m \Psi_{2\alpha} T_{secondary} \right) \tag{6.17}$$

Then, inserting the secondary flux (Equation 6.16) in (6.17) the back-EMF, the adjustable current model is:

$$\begin{aligned} e_{1\alpha}{}^{i} &= \frac{M}{L_{i2}}\left(\frac{1}{T_{secondary}}Mi_{1\alpha} - \frac{1}{T_{secondary}}\Psi_{2\alpha} - \omega_m\Psi_{2\beta}\right) \\ e_{1\beta}{}^{i} &= \frac{M}{L_{i2}}\left(\frac{1}{T_{secondary}}Mi_{1\beta} - \frac{1}{T_{secondary}}\Psi_{2\beta} + \omega_m\Psi_{2\alpha}\right) \end{aligned} \tag{6.18}$$

And, substituting (6.15) in (6.18), it yields:

$$\begin{aligned} e_{1\alpha}{}^{i} &= \frac{M^2}{L_{i2}}\left(\frac{1}{T_{secondary}}i_{1\alpha} - \frac{1}{T_{secondary}}i_{m\alpha} - \omega_m i_{m\beta}\right) \\ e_{1\beta}{}^{i} &= \frac{M^2}{L_{i2}}\left(\frac{1}{T_{secondary}}i_{1\beta} - \frac{1}{T_{secondary}}i_{m\beta} + \omega_m i_{m\alpha}\right) \end{aligned} \tag{6.19}$$

Similarly to (6.13), the instantaneous adaptive reactive power $q^i$ for a rotating induction motor is the cross product of (6.19) and the primary current vectors.

$$q^i = \vec{i}_{1\alpha.\beta} \otimes \vec{e}_{1\alpha.\beta}{}^{i}$$

$$q^i = \frac{M^2}{L_{i2}}\left(\hat{\omega}_m\left(i_{m\alpha}i_{1\alpha} + i_{m\beta}i_{1\beta}\right) + \frac{1}{T_{secondary}}\left(i_{m\alpha}i_{1\beta} - i_{m\beta}i_{1\alpha}\right)\right) \tag{6.20}$$

The error between the two models becomes the input to the PI compensator, which gives the estimated angular mechanical speed. The estimated angular mechanical speed $\hat{\omega}_m$ can be calculated with a PI compensator by:

$$\hat{\omega}_m = \left(k_1{}^s + \frac{k_2{}^s}{s}\right)\cdot\varepsilon \tag{6.21}$$

where: $k_1{}^s$ is the proportional gain for the speed PI compensator,
$k_2{}^s$ is the integral gain for the speed PI compensator,

and

$$\varepsilon = q^v - q^i \tag{6.22}$$

is the error between the adaptive and reference reactive powers (6.14) and (6.20). The method to determine the gains of the estimator and the dynamic analysis is presented in [101].

Finally, the active vehicle estimated speed $\hat{v}_m$ is:

$$\hat{v}_m = \hat{\omega}_m\frac{\tau}{\pi} \tag{6.23}$$

In summary, the speed estimator can track the speed, being robust to thermal variations, especially with the primary and secondary resistances. However, it does not work at stand still. [101].

## 6.2. Vehicle motion control strategy

According to the position of the active vehicle, a simplified block diagram of the vehicle motion control strategy was designed, as depicted in Figures 6.5, 6.6 and 6.7. In the mentioned figures, there are two transitions: the transition between synchronous to induction motor operation and the transition between sensor based to sensorless control. Therefore, there are two different switches,

which are: the switch "I/II" (linear motor operation) and the switch "a/b" (sensorless estimation). When the vehicle travels within a processing station, high accuracy is necessary. Therefore, in a processing station and its surrounding, the position signal information is measured by a magneto-resistive incremental encoder (attached to the vehicle). As shown in Figure 6.5, the linear magnetic scale is shortly extended over the induction rail. The extension of the linear scale along the induction rail has the length of the vehicle, as it is necessary that the primary covers 100% of the induction rail

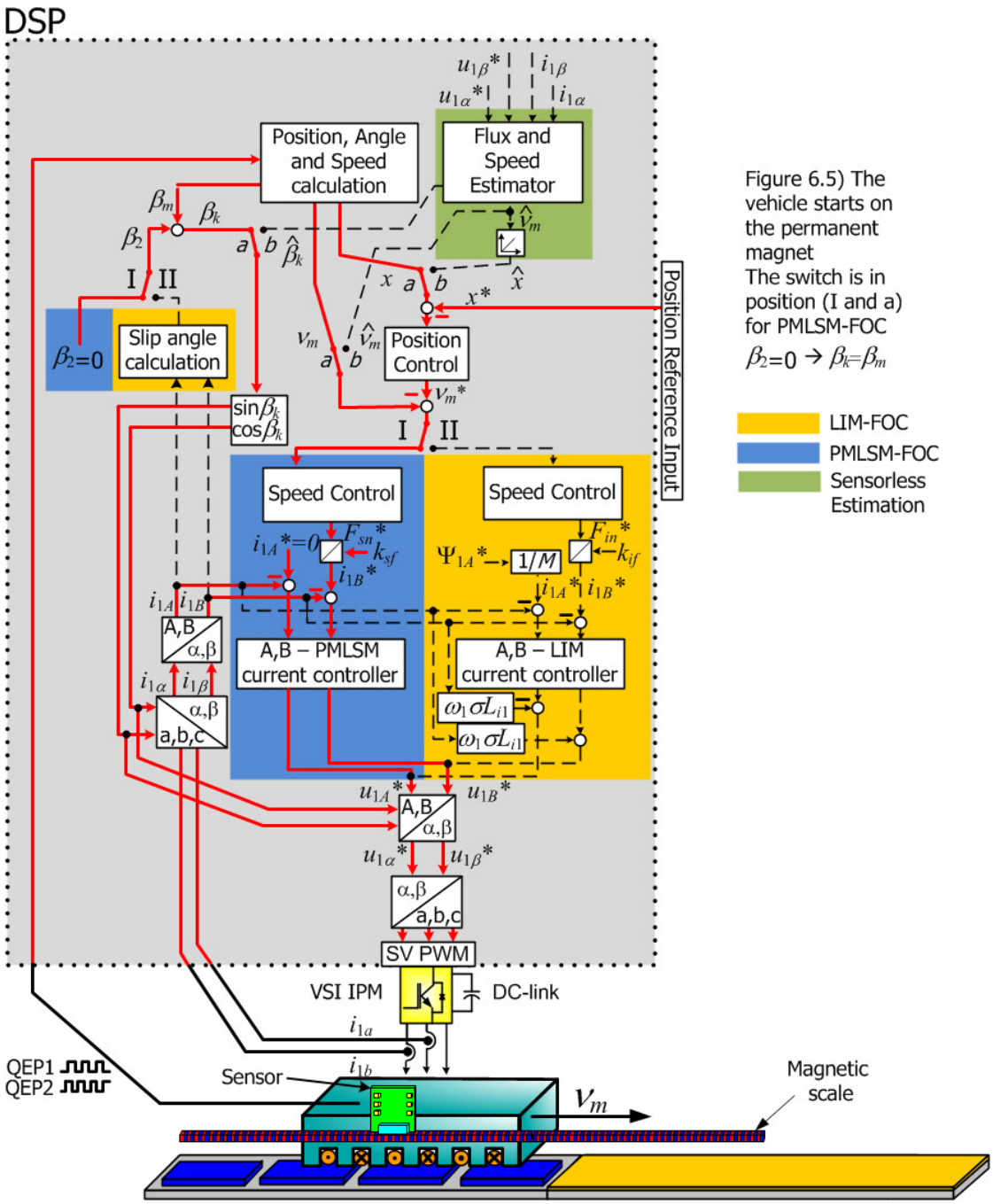


Figure 6.5: Transition control strategy block diagram when active vehicle is traveling within the processing station.

to start the sensorless speed estimation. Outside of this area, the position is estimated using flux and speed estimators (light green area).

### 6.2.1 Transition between synchronous to induction motor

The Figures 6.5 and 6.6 display the transition when the vehicle is leaving a processing section. Within a processing section and its surrounding, the position information is acquired by a magneto-resistive incremental encoder, which is attached to the active vehicle. Its feedback is used for

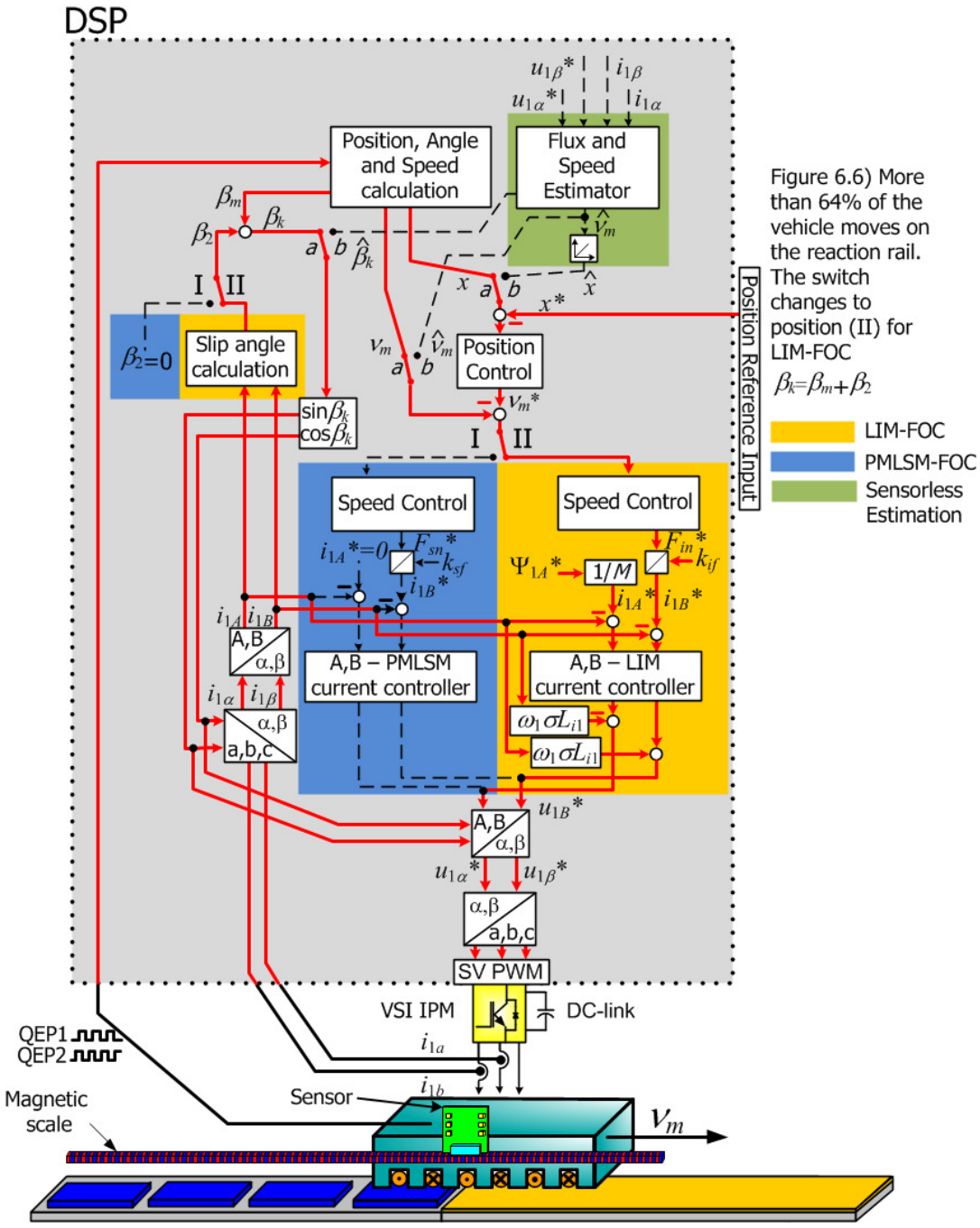


Figure 6.6: Transition control strategy block diagram when the active vehicle is moving on the induction rail section.

orientation of the rotating *AB*- reference frame and for the speed and position controllers. When the vehicle is moving within the processing section, the PMLSM-FOC is turned ON. The transition switch (I/II) keeps in position "I" (see Figure 6.5) and the switch (a/b) is in position "a", for measured values. With the position information sent by the encoder, the position and speed are calculated by the "Position, Angle, and Speed calculation" block. The slip angle $\beta_2$ is set to zero, thus the angular position of the secondary is $\beta_k=\beta_m$. Furthermore, the current and speed controllers use the synchronous linear motor parameters for the control loop. When the vehicle is leaving a processing

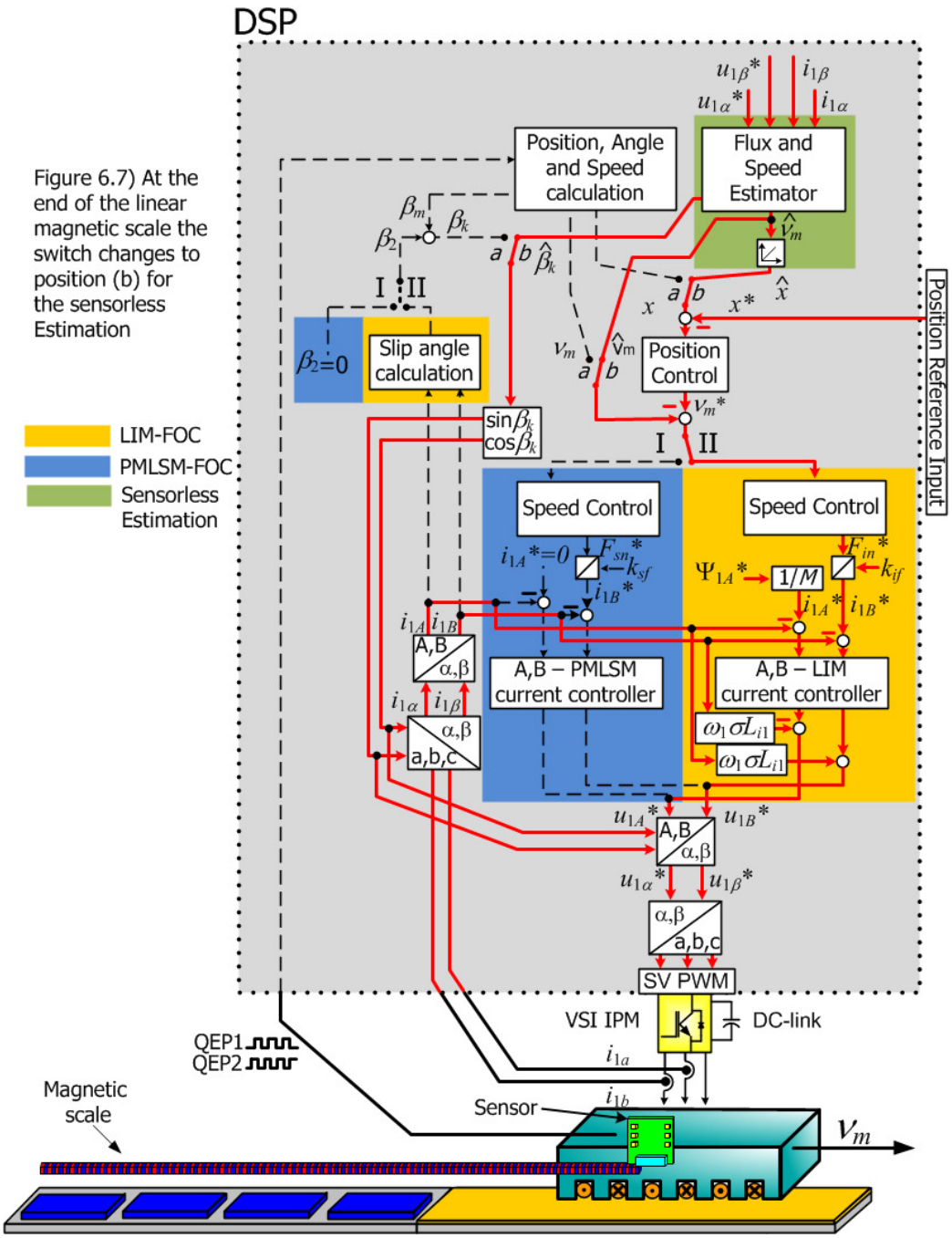


Figure 6.7: Transition control strategy block diagram when active vehicle is moving with sensorless estimation.

section (PMLSM→LIM) and the vehicle has 64% of its length on the induction rail, the switch changes to position "II", then the controller injects the magnetizing current $i_{1A}$ at the rated value and the angular position of the secondary $\beta_k$ is calculated. The LIM current and speed controllers use the induction linear motor parameters for the control loop, as shown in Figure 6.6. At the border, the reluctance force of the stationary magnets becomes very high, decreasing the vehicle speed. On the other hand, if the vehicle is entering a processing station (LIM→PMLSM), the vehicle is strongly attracted by the magnets increasing its speed. For both situations the current $i_{1B}$ is regulated to brake or to accelerate the vehicle avoiding jerks.

### 6.2.2 Transition between sensor based to sensorless control

Figure 6.7 shows the vehicle near to the end of the linear scale and travelling on the induction rail. While the vehicle is inside the linear scale region at the transporting section, the flux and speed estimator block is activated when the measured speed is higher than 0.5m/s. This block has as inputs the reference voltages and the actual currents in $\alpha\beta$-stationary reference frame to estimate the speed and the angular position of the vehicle. At the border of the linear scale, the switch (a/b) changes to position "b", then the electrical angle, the speed and position are the estimated values calculated by the "flux and speed estimator" block. The estimated speed is filtered through a low-pass filter to suppress the noise. The speed and the flux estimators lose performance as the speed decreases, and does not work at standstill, thus the vehicle cannot stop at the transporting section. In case of the next processing station be in use, the vehicle is able to wait at the beginning of the linear scale (see Figure 6.1), which is installed inside the processing section and is shortly extended above the induction rail.

## 6.3. Transition control results

In this section, the implemented experimental setup is put through some tests to verify the performance of the speed and flux estimators. First, a step change in speed is presented in subsection 6.3.1. Then, a transition test (PMLSM to LIM and sensor based to sensorless section) is described in subsection 6.3.2.

### 6.3.1 Step change in speed

In order to get some idea of the performance of the estimator, the speed controller is tested by varying the speed command. First, the speed reference was set to 0.9m/s. When the speed reaches a value higher than 0.5m/s, the estimation is activated. The sensorless control started (switch over to estimated values) when the estimated speed reach steady-state (ca. 170ms). It was not possible to reach speed regulation below 0.12m/s. Thereafter, the reference speed was changed to 0.7m/s at time 0.65s. In Figure 6.8a, it can be observed that the estimated speed (green line) agrees with the measured speed (blue line) for $t$>0.45s only. From Figure 6.8b the accuracy of the estimation. The designed speed control has a good performance under abrupt changes of the reference speed. In Figure 6.8c, the controlled current responses are displayed.

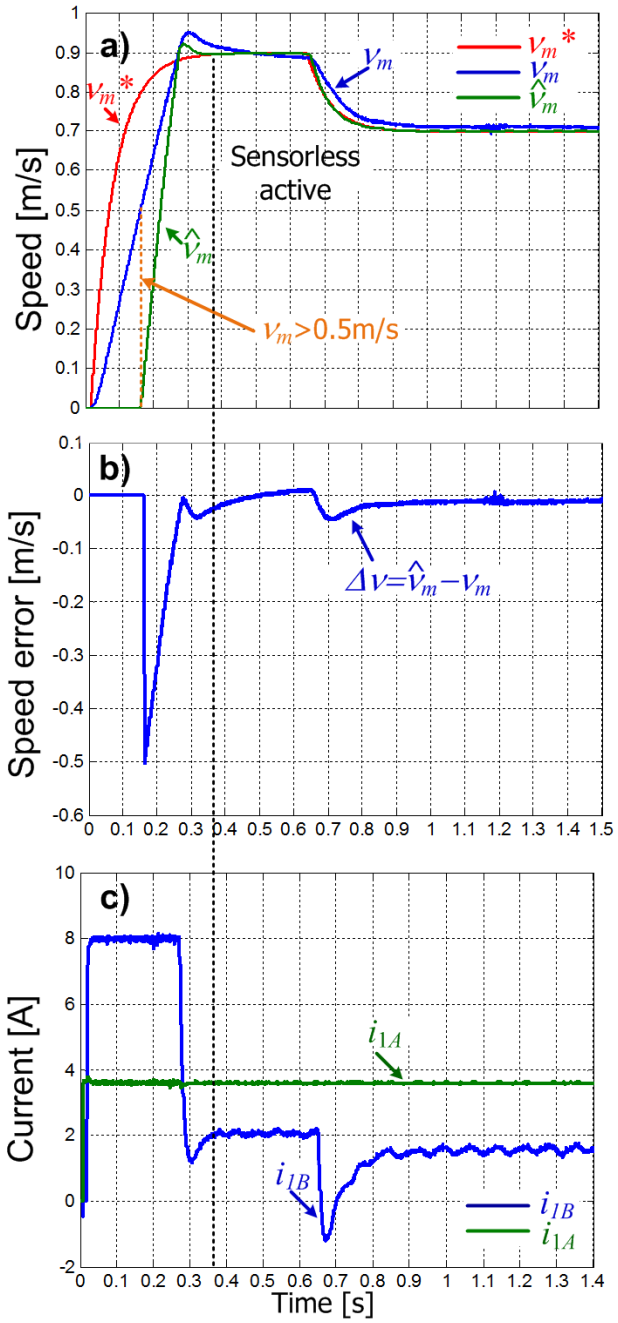


Figure 6.8: Experimental test result of a step change in speed: a) reference, estimated and actual speed; b) difference between the estimated speed and actual speed; c) controlled currents in the *A*- and *B*- axis current.

### 6.3.2 Transition test

For the transition test, a position command was applied in order to test the transitions (motor operations and with/without sensor). The tested drive cycle is shown in Figure 6.9.

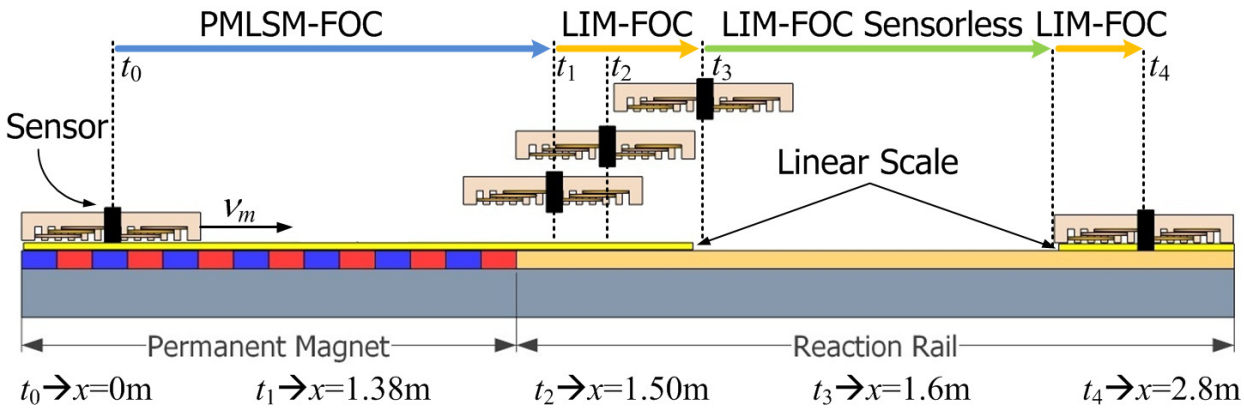


Figure 6.9: Sketch of the active vehicle position during transition test.

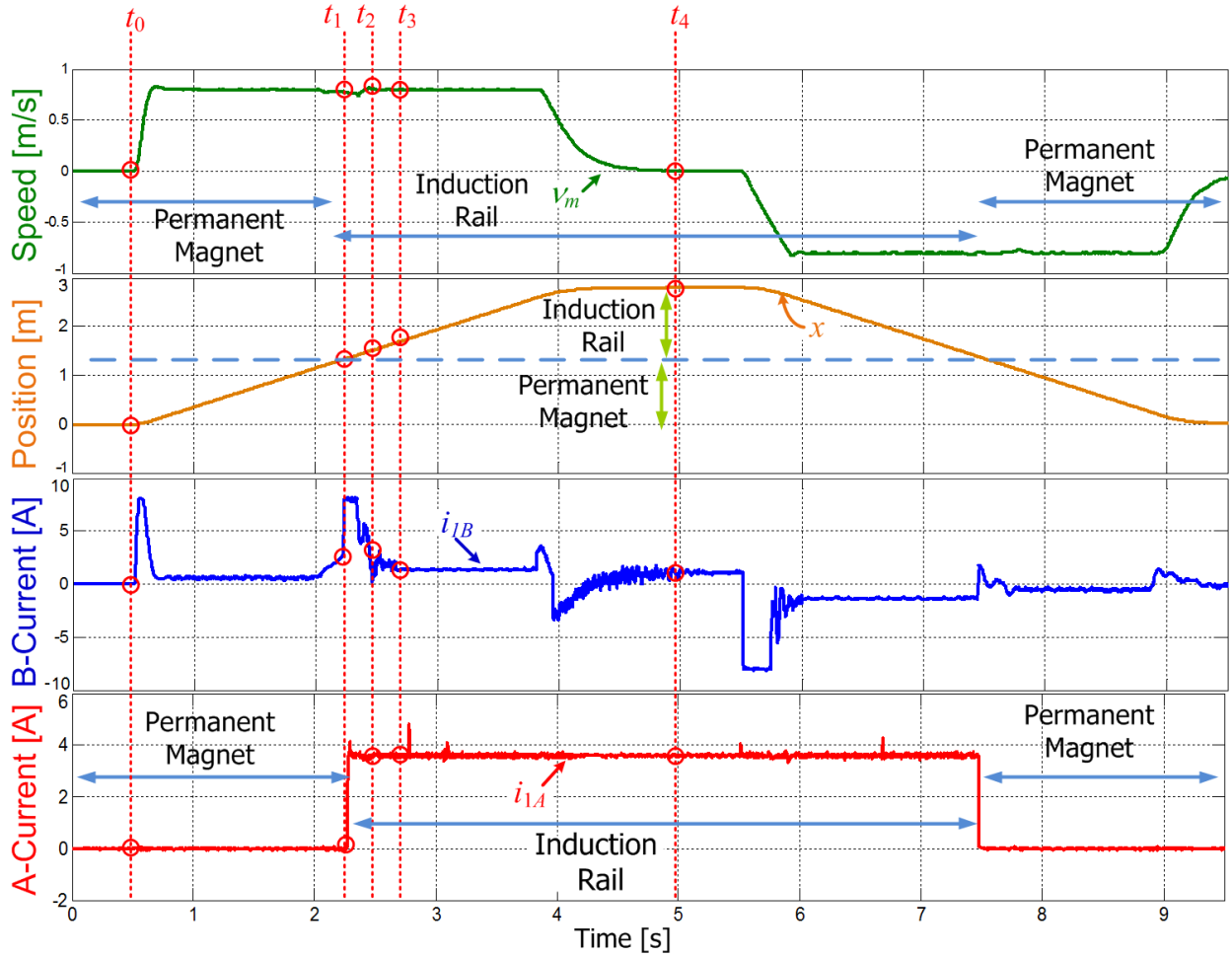


Figure 6.10: Measured position, speed and current for the sensorless drive cycle.

The vehicle starts from the initial position at time $t_0$, reaches the transition operation area (PMLSM→LIM) at the time $t_1$, then at time $t_2$ the sensorless estimation is started, when speed is higher than 0.5m/s and the vehicle covers 100% of the induction rail. After being enabled, the speed estimator reaches the steady state and when the vehicle is near to the end of the linear scale, the switch (a/b) for sensorless estimation is switched to position "b" at time $t_3$. At time $t_4$, the vehicle

stops and returns to the original position. The speed, position and current responses for the executed drive cycle are shown in Figure 6.10.

The first transition interval is zoomed in Figure 6.11. At the transition between synchronous to induction operation ($t_1$), Figure 6.11a shows that the vehicle speed decreases when the magnetizing current is applied (see Figure 6.11b). Simultaneously, the current $i_{1B}$ rises to increase the thrust force,

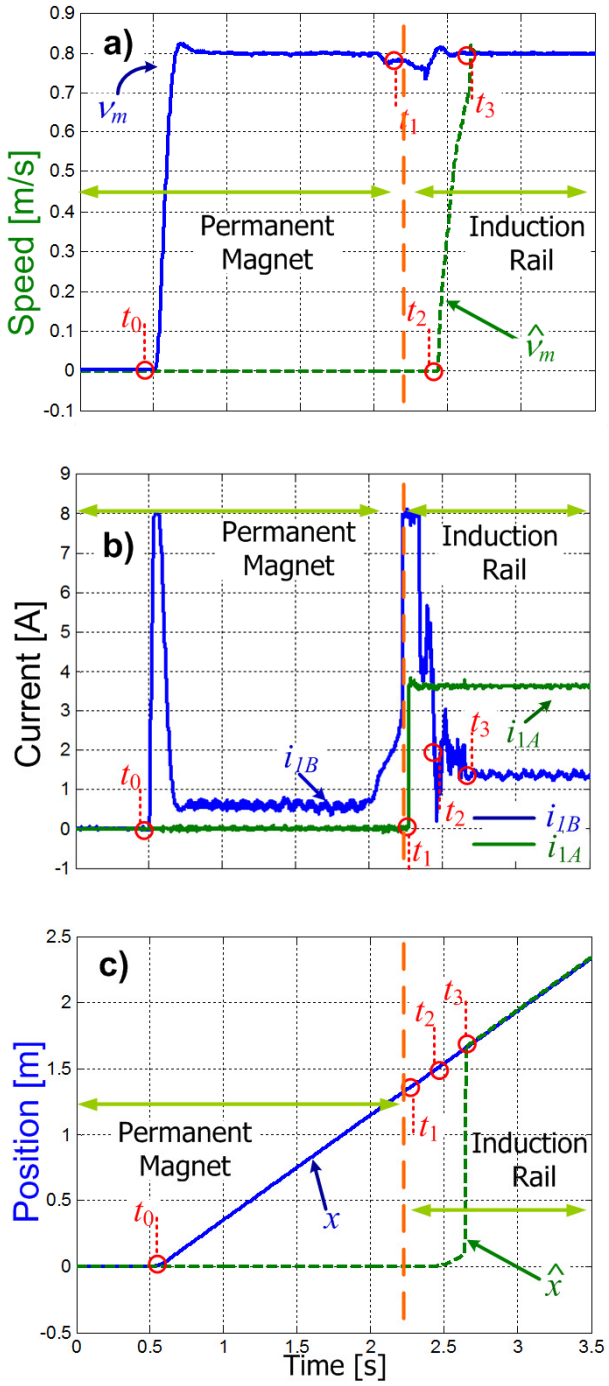


Figure 6.11: Position, speed and current responses when the vehicle is leaving a processing station: a) sensed and estimated position; b) controlled currents in the *A*- and *B*- axis current; c) sensed position and estimated position.

since the LIM force constant ($k_{if}$) is around one-half of the PMLSM force constant ($k_{sf}$). The vehicle has now exited a processing station and moves with constant speed of 0.8m/s through the transport section, as shown in Figure 6.11a.

At time $t_2$, the sensorless estimation is activated. Afterwards, the speed estimator reaches the steady-state value and near to the end of the linear scale, the switch (a/b) is changed to the position "b". Therefore, the estimated position and speed are used in the control loop. The difference between the estimated position and the measured value is synchronized ($\hat{x} = x$), as shown in Figure 6.11c. After crossing the transition area, the currents were kept constant to maintain the vehicle speed at 0.8 m/s, as depicted in Figure 6.11b. Finally, the vehicle moves towards the next sensor based region ($t_4$), where the switch (a/b) returns to position "a" for the sensor based position control and again, the position is synchronized.

# 7. Conclusion

The design of a short primary linear motor for combined synchronous and induction operation with on-board energy storage was completed with some success. As shown in the two last chapters, the goals were mostly met. The summary from all experimental results and some topics which could be more investigated to improve the current project are described in this chapter.

## 7.1. Summary

This thesis deals with the design of a short primary linear drive with combined synchronous and induction operation mode with on-board energy storage for an industrial manufacturing system. This opens new ideas to investigate the current systems, simplifying the mechanical complexity and increasing the scalability and independency of the vehicles. Nevertheless, the main innovative contribution of this thesis is the combined operation (induction and synchronous) of a short primary linear motor.

In chapter 1, different topologies of material handling system using linear drives were reviewed and analyzed. The significant advantages of the LIM at the transporting section were: the track's cost can be reduced by saving magnets outside the processing station and horizontal and vertical curves can be easily built due to the simple reaction rail.

The topology presented here (active vehicles on passive track with contactless system) has the disadvantage of limited peak power. In order to solve this issue, a bidirectional DC-DC converter with an ultracapacitor (energy storage) was designed to compensate this peak power limit. Then, a control strategy has been developed to control the bidirectional DC-DC converter to deliver peak power, to charge the ultracapacitor and to absorb the braking energy. The experimental results presented in chapter 2 show that the bidirectional DC-DC converter can supply the peak power during the acceleration and absorb the generated energy during the braking period.

One laboratory prototype of a short primary linear drive with an on-board energy storage device was assembled and depicted in chapter 3. The utilized contactless system is an industrial/commercial equipment from *SEW-Eurodrive* and the PMLSM (primary and magnet segments) from *Baumüller*. The induction rail, the VSI and the bidirectional DC-DC converter were developed at our Institute. Furthermore, mathematical models based on the rotating *AB*- reference frame for the LIM, and the PMLSM which are necessary for the implementation of the FOC were presented in chapter 4. Also, experimental results were carried out in order to determine the thrust force constant for both operation modes.

Based on the mathematical model described in chapter 4, the current, speed and position control loops were implemented for both operations (LIM and PMLSM) as presented in chapter 5. Moreover, the track was equipped with a linear magnetic scale inside and outside the processing station, for high accuracy of positioning. As the linear scale was installed in the whole track, all the traveling vehicles can be stopped inside the transporting section and wait for the next processing

station to be released. Therefore, a transition control strategy has been developed to control the active vehicle for a low speed drop when it moves between the permanent magnets and the reaction rail sections. The proposed transition control strategy was verified experimentally with a satisfactory control of speed and position in both regions (LIM and PMLSM). Therefore, the designed control strategy has proven to fulfill the demands of speed control and positioning at both sections.

In chapter 6, a sensorless method was presented, considering that the linear scale could be installed only within the processing station and its surrounding. At the transporting section, where the vehicle should move only with slow speed changes, sensorless methods (speed and flux) were implemented. Further, the principle of the employed flux and speed estimators were described. The sensorless speed method was estimated using a classic MRAS speed estimator based on rotating induction machines. At last, a sensorless motion control strategy has been developed to control the active vehicle, when it moves between the sensor based to sensorless sections and between synchronous to induction operation (or vice-versa).

The experimental results show that the transition between both regions is smooth with a satisfactory control of speed and position, with the possibility to stop the vehicle surrounding the processing section and wait it to be released. The proposed sensorless motion control strategy has proven to fulfill the requirements for applications, where speed control is required at the transporting section, and the starting and stopping of the vehicle will happen inside a processing section and its surrounding.

Finally, for a material handling application with very long track, low density of vehicles and moderate acceleration, the topology of short primary linear machines may be a good solution.

## 7.2. Future work

Future works can be done to complete and improve some results for the proposed industrial manufacturing system. They are listed below:

- It is necessary to find a better relation between the maximal on-board power (ultracapacitors) and the maximal power of the contactless energy transmission. Therefore, the on-board mass would be reduced. Moreover, a bidirectional contactless system could be used to transfer power to the vehicles, avoiding a situation where the ultracapacitors are fully charged.
- The efficiency and the thrust force when the vehicle is traveling at the transporting section may be increased if a ladder secondary is employed. Then, the air-gap would be smaller and a thicker copper sheet for high-current values would be avoided. However, the assembly cost would increase as well.
- In case of a transporting section without linear scale, a high-frequency signal injection sensorless method could be utilized, with the advantage of vehicles stopping, waiting and starting in this section.
- The motion control's quality, when the active vehicle is crossing the border between both secondary types can be improved. Then, FEM simulations and mathematical models about the operation at border should be more studied, in order to compensate the disturbances.

- An optimized efficiency method could be implemented, since the magnetizing current can be regulated according to the load (optimized air-gap flux). Therefore, only the ultracapacitor bank would be necessary to supply the vehicle at the transporting section, reducing the length of the primary conductor loop in the contactless energy transmission and increasing the efficiency for induction operation mode.
- Finally, the implementation of a multiple vehicle system should be considered. Not forgetting the communication issues necessary to make it successful.

# Bibliography


[1] A. Cassat, N. Corsi, R. Moser and N. Wavre, "Direct linear drives: market and performances status," *in 4th International Symposium on Linear Drives for Industry Applications*, 2003, LDIA'03, pp. 1-11.

[2] J. Gieras, "*Linear Induction Drives*," Oxford: Clarendon Press, 1994, ISBN 0198593813.

[3] E. R. Laithwaite, "Linear electric machines – a personal view," *in Proceedings of the IEEE*, vol. 63, no. 2, pp. 250-290, February. 1975.

[4] G. Brandenburg, S. Brückl, J. Dormann, J. Heinzl, and C. Schmidt, "Comparative investigation of rotary and linear motor feed drive systems for high precision machine tools," *in 6th International workshop on Advanced Motion Control*, Mar-Apr. 30-1, 2000, pp. 384-389.

[5] H. Gurol, "General atomics linear motor applications: moving towards deployment," *in Proceedings of the IEEE*, vol. 97, no 11, pp. 1864-1871, November 2009.

[6] Li. Xiaoli, R. Du,B. Denkena and J. Imiela, "Tool breakage monitoring using motor current signals for machine tools with linear motors," *in IEEE Transactions on Industry Electronics*, v. 52., no. 5, pp. 1403-1408, October 2005.

[7] N. J. Elliott, "Novel application of a linear synchronous motor drive," *in IEE Colloquium on Update on New Power Electronic Techniques*, 1997, pp. 8/1-8/5.

[8] D. C. Meeker and M. J. Newman, "Indirect vector control of a redundant linear induction motor for aircraft launch," *in Processings of IEEE*, v. 97, no. 11, pp. 1768-1776, November 2009

[9] R. Krishnan, H. S. Lim and N. S. Lobo, "Comparison of linear switched reluctance machines for vertical propulsion application: analysis, design, and experimental correlation," *in IEEE Transactions on Industry Applications*, v. 44., no. 4, pp. 1134-1142, July/August 2008.

[10] H. Polinder, B.C. Mecrow, A.G. Jack, P.G. Dickinson and M.A. Mueller, "Conventional and TFPM linear generators for direct-drive wave energy conversion," *in IEEE Transactions on Energy Conversion*, v. 20., no. 2, pp. 260-267, June 2005.

[11] Y. Luguang, "The linear motor powered transportation development and application in china," *in Processings of IEEE*, v. 97, no. 11, pp. 1872-1880, November 2009.

[12] J.F. Gieras and Z.J. Piech, "*Linear synchronous motors: transportation and automation systems*," CRC Press, Boca Raton, 1999, ISBN 0849318599.

[13] S. Yamamura, H. Ito and Y. Ishulawa, "Theories of the linear, induction motor and compensated linear induction motor," *in IEEE Transactions on Power Apparatus and Systems*, v. 91, no. 4, pp. 1700-1710, July 1972.

[14] I. Boldea and S. A. Nasar, "*The induction machine handbook*," 2th ed. CRC Press, Boca Raton, 2009, ISBN 1420066684.

[15] G.H. Abdou and S.A. Sherif, "Theoretical and experimental design of LIM in automated manufacturing systems," *in IEEE Transactions on Industry Applications*, v. 27, no. 2, pp. 286-293, March/April 1991.

[16] P.L Jansen, L.J Li and R.D. Lorenz, "Analysis of competing topologies of linear induction machines for high-speed material transport systems," *in IEEE Transactions on Industry Applications*, v. 31, no. 4, pp. 925-932, July/August 1995.

[17] Hyung-Suk Han, Chang-Hyun Kim, Jong-Min Lee and Chang-Woo Lee, "System integration of a non-contact conveyer using magnetic levitation technology," *in IEEE International Conference on Mechatronics*, 2011, ICM 2011, pp. 708-712.

[18] K. Steele, "A conveyor for sealed environs," in Machinedesign.com, pp. 72-73, August 2007. http://machinedesign.com/article/a-conveyor-for-sealed-environs-0823.

[19] P. G. Ranky, "MagneMotion's linear synchronous motor (LSM) driven assembly automation and material handling system designs," *in Assembly Automation Journal*, v. 27, no. 2, pp. 97-102, 2007.

[20] P. Mutschler and S. Silaghiu, "Linear drives for material handling and processing: A comparison of system architectures", *in 34th Annual Conference of the IEEE Industrial Electronics Society*, 2008, IECON '08, pp. 1264-1269.

[21] R. Benavides, "Investigation of control methods for segmented long stator linear drives," PhD. thesis, TU Darmstadt, Germany 2008.

[22] M. Mihalachi and P. Mutschler, "Long primary linear drive for material handling," *in International Conference on Electrical Machines and Systems*,2009, ICEMS'09, pp. 1-6.

[23] S. Silaghiu and P. Mutschler, "Optimizing operation of segmented stator linear synchronous motors", *in 5th IET International Conference on Power Electronics, Machines and Drives*, 2010, PEMD'10, pp. 1-6.

[24] T.R Fernandes Neto and P. Mutschler, "Short primary linear synchronous motor drive with an ultracapacitor regenerative braking system for material handling and processing," *in 8th International Symposium on Linear Drives for Industry Applications*, 2011, LDIA'11.

[25] J. M. Barnard, J. A. Ferreira and J. D. van Wyk, "Sliding transformer for linear contactless power delivery," *in IEEE Transactions on Industrial Electronics*, v. 44, no. 6, pp.774-779, December 1997.

[26] G. A. Covic, J. T. Boys, M. L. G. Kisin and H. G. Lu, "A three-phase inductive power transfer system for roadway-powered vehicles," *in IEEE Transactions on Industrial Electronics*, v. 54, no. 6, pp. 3370-3378, December 2007.

[27] S. Judek and K. Karwowski, "Supply of electric vehicles via magnetically coupled air coils," *in 13th Power Electronics and Motion Control Conference*, EPE-PEMC, September 2008, pp. 1497-1504.

[28] D. Robertson, A. Chu, A. Sabitov and G.A. Covic, "High power IPT stage lighting controller," *in IEEE International Symposium on Industrial Electronics*, ISIE, August 2011, pp. 1974-1979.

[29] SEW-EURODRIVE, Contactless Energy Transfer MOVITRANS® (System Descriptions), Edition 06/2007, http://www.seweurodrive.com/download/pdf/11626216.pdf.

[30] VAHLE, CPS® Contactless Power System (Katalog 5a), http://www.vahle.de/vahleassets/pdf/Kataloge/deutsch/Cat_05a_de_CPS_Beruehrungslose_Energieuebertragung.pdf.

[31] P. Knaup, "A method to optimize the size of the transformer core for magnetic power transfer to linear moving devices," *in PCIM*, 1998, pp. 705-714.

[32] Ch-S. Wang, O. H. Stielau and G. A. Covic, "Design considerations for contactless electric vehicle battery charger," *in IEEE Transactions on Industrial Electronics*, v. 52, no. 5, pp.1308-1313, October 2005.

[33] H. Abe, H. Sakamoto and K. Harada. "A noncontact charger using a resonant converter with parallel capacitor of the secondary coil," *in IEEE Transactions on Industry Applications*, v. 36, no. 2, pp. 444 -451, March/April 2000.

[34] T. Bieler, M. Perrottet, V. Nguyen and Y. Perriard, "Contactless power and information transmission," *in IEEE Transactions on Industry Applications*, v. 18, no. 5, pp. 1266-1272, September/October 2002.

[35] K.W. Klontz, D.M. Divan, D.W. Novotny and R.D Lorenz, "Contactless power delivery system for mining applications," *in IEEE Transactions on Industry Applications*, v. 31, no. 1, pp. 27-35, January/March 1995.

[36] A.W. Kelly and W.R. Owens, "Connectorless power supply for an aircraft-passenger entertainment system," *in IEEE Transactions on power Electronics*, v. 4, no. 3, pp. 348-35, July 1989.

[37] O. H. Stielau and G. A. Covic, "Design of loosely coupled inductive power transfer systems," *in International Conference on Power System Technology Proceedings*, PowerCon, December 2000, pp. 85-90.

[38] J. T. Boys, G. A. Covic and A. W. Green, "Stability and control of inductively coupled power transfer systems," *in IEE Proceedings – Electric Power applications*, v. 147, no. 1, pp. 37–43, January 2000.

[39] A.W. Green and J. T. Boys, "10 kHz inductively coupled power transfer-concept and control," *in 5th International conference on Power Electronics and Variable-Speed Drives*, October 1994, pp. 694-699.

[40] J. F. Keithley, "*The story of electrical and magnetic measurements from 500 BC to the 1940s*," 1th ed. Wiley-IEEE Press, 1999, ISBN 0780311930.

[41] J. Miller and R. Smith, "Ultracapacitor assisted electric drives for transportation," Maxwell technologies, White Papers, www.maxwell.com, 2004.

[42] G. Zorpette, "Super charged," *in IEEE Spectrum*, v. 42, n. 1, pp. 32-37, 2005.

[43] M. Lätt, J. Leis, M. Arulepp, H. Kuura and E. Lust, "Latest developments in carbide derived carbon for energy storage application," *in Proceedings of 16th International Seminar on Double Layer Capacitors & Hybrid Energy Storage Devices*, 2006, pp. 62-72.

[44] A. Burke, "Ultracapacitors: why, how, and where is the technology," *in Journal of Power Sources*, 2000, pp. 37-50.

[45] P. A. von Jouanne, N. Enjeti and B. Banerjee, "Assessment of ride-through alternatives for adjustable-speed drives," *in IEEE Transactions on Industry Applications*, v. 35, no. 4, pp. 908-916, January 1999.

[46] L. Gao, R. A. Dougal and S. Liu, "Power enhancement of an actively controlled battery/ultracapacitor hybrid," *in IEEE Transactions on Power Electronics*, v. 20, no. 1, pp. 236-243, January 2005.

[47] R.L. Spyker and R.M. Nelms, "Classical equivalent circuit parameters for a double-layer capacitor," *in IEEE Transactions on Aerospace and Electronic Systems*, v. 36, no. 3 , pp. 829-836, July 2000.

[48] Y. Diab, P. Venet, H. Gualous and G. Rojat, "Self-discharge characterization and modeling of electrochemical capacitor used for power electronics applications," *in IEEE Transactions on Power Electronics*, v. 24 , no. 2, pp. 510-517, February 20009.

[49] Maxwell Active Cell Voltage Management Electronics Document, Revision 1.0, February 2007, http://www.maxwell.com/products/ultracapacitors/docs/maxwell_active_cell_voltage_management_electronics_rev1.pdf.

[50] BPAK0058, Energy Series Datasheet, http://about.maxwell.com/pdf/uc/datasheets/eol/BC_15V_ PAK_Energy_1009475_rev4.pdf.

[51] N. Mohan, T. M. Undeland and W. P. Robins, "*Power electronics converters, applications, and design*," 3th ed. New York: John Wiley & Sons, 2002, ISBN 0471226939.

[52] Ferrite and accessories PM 114/93, http://www.epcos.com/inf/80/db/fer_07/pm_114_93.pdf.

[53] Aluminum electrolytic capacitors with 4-pin snap-in terminals and solder pins, http://www.epcos.com/inf/20/30/db/aec_2011/B43511__21.pdf.

[54] R. B. Ridley, B. H. Cho and F. C. Lee, "Analysis and interpretations of loop gains of multiloop-controlled switching regulators," *in IEEE Transactions on Power Electronics*, v. 3, no. 4, Oct 1988, pp. 489 -498.

[55] L. Dixon, "Average current control of switching power supplies," UNITRODE, Application Note U-140, pp. 457-470, 1994.

[56] P. Mutschler. Class Lecture, Topic: "Control of drives," Institute of Power Electronics and Control of Drives, TU Darmstadt, September 2004.

[57] M. Qiao, P. Parto and R. Amiran, "Stabilize the buck converter with transconductance amplifier," International Rectifier Corporation, Application Note AN-1043, pp. 1-11, 2002.

[58] W. Tang, F.C. Lee and R.B. Ridley, "Small-signal modeling of average current-mode control," *in IEEE Transactions on Power Electronics*, v. 8, no. 2, pp. 112-119, April 1993.

[59] SKM75GB123D SEMITRANS®2 IGBT Modules, http://www.semikron.com/products/data/cur/ assets/SKM75GB123D_22890000.pdf.

[60] SKHI22A/B H4 SEMIDRIVERTM Hybrid Dual IGBT Driver, http://docs-europe.electrocomponents .com/ webdocs/0563/0900766b80563f08.pdf.

[61] Voltage Transducer LV 25-P, http://www.lem.com/docs/products/lv%2025-p.pdf.

[62] Current Transducer LA 25-NP, http://www.lem.com/docs/products/la%2025-np%20e.pdf.

[63] Y. Zhang, S. Sobhani and R. Chokhawala, "Snubber considerations for IGBT applications," International Rectifier Corporation, Technical Paper, pp. 1-9.

[64] Linear drives LSE, LSC, LSA, http://www.baumueller.de/DownloadInternet/Prospekteenglisch/Linearmotoren_en_web.pdf.1

[65] SEW-EURODRIVE, Mobile Energy Supply MOVITRANS®THM10C/THM10E Pick-ups (Operating Instructions), Edition 07/2010, http http://www.sew-eurodrive.de/download/pdf/16994019.pdf.

[66] Force sensor KD40S, http://www.me-systeme.de/en/datasheets/kd40s.pdf

[67] Strain gage measuring amplifier GSV-1, http://www.me-systeme.de/en/datasheets/gsv1.pdf

[68] Mitsubishi Semiconductor, Dual-inline-package Intelligent Power Module PS22056 insulated type, May 2005, http://www.mitsubishielectric-mesh.com/products/pdf/ps22056_e.pdf.

[69] S. Silaghiu and P. Mutschler, "Communication topology in a modular servo-drive system based on long stator permanent magnet synchronous linear motor," *in 5th IET International conference on Power Electronics, Machines and Drives*, PEMD, April 2010, pp. 1-6.

[70] J. Lamp, "IGBT peak voltage measurement and snubber capacitor specification," SEMIKRON, Application Note AN-7006, pp. 1-8, 2008.

[71] Spectrum Digital INC., eZdsp™F2812 (Technical Reference), 07/2003, http://c2000.spectrumdigital.com/ezf2812/docs/ezf2812_techref.pdf.

[72] Texas Instruments, TMS320F2810 - TMS320F2812 Digital Signal Processors (Data manual), 03/2011, SPRS174S, http://www.ti.com/lit/ds/sprs174s/sprs174s.pdf.

[73] PC/104 Embedded Consortium, http://www.pc104.org/.

[74] EUROTECH, DuraNAV, http://www.eurotech-inc.com/info/datasheets/duranav1000-sf.pdf.

[75] Texas Instruments, OMAP™4 mobile applications platform, http://www.ti.com/lit/ml/swpt034b/swpt034b.pdf.

[76] CONDUCTIX wampfler, Inductive Power Transfer IPT (Product overview), http://www.ipandc.com/acatalog/download/inductive.pdf.

[77] S. Campbell and H. A. Toliyat, "*DSP-Based Electromechanical Motion Control*," CRC Press, Boca Raton, 2003, ISBN 0849319188.

[78] W. Leonhard, "*Control of Electrical Drives*," 3rd Ed., Springer-Verlag, 2001, ISBN 3540418202.

[79] I. Boldea and S. A. Nasar, "*Linear Electric Actuators and Generators*," Cambridge University Press, 2005, ISBN 0521020328.

[80] N. P. Quang and J. A. Dittrich, "*Vector Control of Three-Phase AC Machines: System Development in the Practice*," 1th ed., Springer, 2008, ISBN 3540790284.

[81] J. K. Seok and S. K. Sul, "Induction motor parameter tuning for high-performance drives," *in IEEE Transactions on Industrial Applications*, v. 37, no. 1, Jan/Feb 2001, pp. 35-41.

[82] S. Maiti, C. Chakraborty, Y. Hori, and M. C. Ta, "Model reference adaptive controller-based rotor resistance and speed estimation techniques for vector controlled induction motor drive utilizing reactive power," *in IEEE Transactions on Industrial Electronics*, v. 55, no. 5, pp. 594-601, April 2008.

[83] R. Benavides and P. Mutschler, "Compensation of disturbances in segmented long stator Linear drives using finite element models," *in IEEE International Symposium on Industrial Electronics*, ISIE, July 2006, pp. 2445-2449.

[84] S. Preitl, R. E. Precup, A. I. Stinean, C.A. Dragos and B. M. Radac, "Extensions in symmetrical optimum design method. Advantages, applications and perspectives," *in 6th IEEE International Symposium on Applied Computational Intelligence and Informatics*, SACI, May 2011, pp. 17-22.

[85] J. Holtz, "Sensorless control of induction motors-performance and limitations," *in Proceedings of the 2000 IEEE International Symposium on Industrial Electronics*, December 2000.

[86] P. Vas, "*Sensorless Vector and Direct Torque Control*," 1th ed., Oxford University Press, 1998, ISBN0198564651.

[87] R. Leidhold and P. Mutschler, "Speed sensorless control of a long-stator linear synchronous motor arranged in multiple segments," *in IEEE Transactions on Industrial Electronics*, v. 54, no. 6, pp. 3246-3254, December 2007.

[88] R. Hyung-Min, H. Jung-Ik and S. Seung-Ki, "A new sensorless thrust control of linear induction motor," *in Conference Record of the 2000 IEEE Industry Applications Conference*, October 2000, pp. 1655-1661.

[89] P.L. Jansen and R.D. Lorenz, "Transducerless field orientation concepts employing saturation-induced saliencies in induction machines," *in IEEE Transactions on Industrial Electronics*, v. 32, no. 6, pp. 1380-1393, November/December 1996.

[90] R. Leidhold, "Position Sensorless Control of PM Synchronous Motors Based on Zero-Sequence Carrier Injection," *in IEEE Transactions on Industrial Electronics*, v. 58, no. 12, pp. 5371-5379, December 2011.

[91] R. Leidhold and P. Mutschler, "Sensorless position-control method based on magnetic saliencies for a Long-Stator Linear Synchronous-Motor," *in 32th Annual Conference on IEEE Industrial Electronics*, IECON, November 2006, pp. 781-786.

[92] P.L. Jansen, R.D. Lorenz and D.W. Novotny, "Observer-based direct field orientation: Analysis and comparison of alternative methods," *in IEEE Transactions on Industry Applications*, v. 30, no. 4, pp. 945-953, July/August 1994.

[93] P.L. Jansen and R.D. Lorenz, "A physically insightful approach to the design and accuracy assessment of flux observers for field oriented I.M. drives," *in IEEE Transactions on Industry Applications*, v. 30, no. 1, pp. 101-110, January/February 1994.

[94] C. Schauder, "Adaptive speed identification for vector control of induction motors without rotational transducers," *in IEEE Transactions on Industrial Applications*, v. 28, no. 5, pp. 1054-1061, September/October 1992.

[95] D. Leggate and R.J. Kerkman, "Pulse-based dead-time compensator for PWM voltage inverters," *in IEEE Transactions on Industrial Electronics*, v. 44, no. 2, pp. 191-197, April 1997.

[96] M. Carmeli, F. Castelli Dezza, M. Iacchetti and R. Perini, "Effect of the inverter non-linearities compensation on a MRAS speed estimator in a double fed induction motor drive," *in Electrical Engineering*, v. 90, no. 4, pp. 283-291, April 2008.

[97] H. Namho, H. Kichul and N. Kwanghee, "Sensorless vector control in the presence of voltage and current measurement errors by dead-time," *in 32th Industry Applications Society Annual Meeting*, IAS, October 1997, pp. 433-438.

[98] A.R. Munoz and T.A. Lipo, "On-line dead-time compensation technique for open-loop PWM-VSI drives," *in IEEE Transactions on Power Electronics*, v. 14, no. 4, pp. 683-689, July 1999.

[99] TMS320x281x DSP Event Manager (EV) Reference Guide, 07/2007, SPRU065E, http://www.ti.com/lit/ug/spru065e/spru065e.pdf.

[100] P.L. Jansen, C.O. Thompson and R.D. Lorenz, "Observer-based direct field orientation for both zero and very high speed operation," *in Power Conversion Conference*, PCC, April 1993, pp. 432-437.

[101] F.Z. Peng and T. Fukao, "Robust speed identification for speed-sensorless vector control of induction motor," *in IEEE Transactions on Industry Applications*, v. 30, no. 5, pp. 1234-1240, September/October 1994.

[102] V. Vorpérian, "Simplify PWM converter analysis using a PWM switch model," *in PCIM*, 1990, pp. 10-15.

# Appendix A

## A.1 Bidirectional DC-DC converter

The operation analysis and small signal model deductions for the Buck mode and the two-quadrant (Boost mode) described in following.

### A.1.1 Two-quadrant operation (Boost mode) at the boundary between continuous and discontinuous conduction

Figure A.1 shows the waveform at the edge of continuous conduction. In this operation $i_L$ goes to zero at the end of the interval. The $I_L'$ current at boundary condition is given by:

$$\begin{aligned} I_L' &= \frac{1}{2} i_{Lpeak} \\ I_L' &= \frac{1}{2} \frac{V_{UC}}{L_{\min}} t_{on} \\ I_L' &= \frac{1}{2} \frac{V_{UC}}{L_{\min}} \frac{(V_{dclink} - V_{UC}) T_s}{V_{dclink}} \\ I_L' &= \frac{1}{2} \frac{(V_{dclink} - V_{UC}) V_{UC} T_s}{L_{\min} V_{dclink}} \end{aligned} \tag{A.1}$$

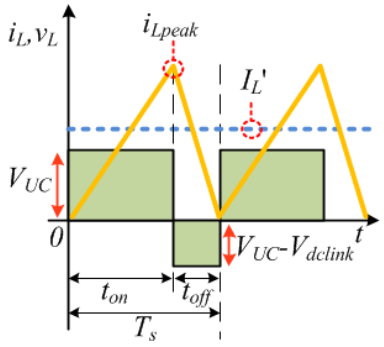


Figure A.1: two-quadrant (Boost mode) boundary between continuous and discontinuous mode.

Since $I_L'=I_{UCmax}$ and $V_{UC}=V_{UCf}$, the value of $L_{\min}$ to design the converter is based in the equation (A.1) in the boundary condition. Thus $L_{min}$ is:

$$L_{\min} = \frac{1}{2} \frac{(V_{dclink} - V_{UCf}) V_{UCf} T_s}{I_{UCmax} V_{dclink}} \tag{A.2}$$

Since the inductor voltage is:

$$v_L = L \frac{\Delta I_L}{\Delta t} \tag{A.3}$$

The maximum inductor current occurs in the conduction $t_{on}$ and for the minimum value of the ultracapacitor bank voltage $V_{UCf}$, so that $v_L=V_{UCf}$ and $\Delta t=t_{on}=\lambda T_s$ then:

$$\Delta I_L = \frac{V_{UCf}}{L}\lambda T_s \tag{A.4}$$

Assuming a current ripple of 10%, the inductor value is:

$$L = \frac{V_{UCf}}{\Delta I_L}\lambda T_s = \frac{V_{UCf}}{I_{UC\max}0.1}\lambda T \simeq 0.8mH \tag{A.5}$$

### A.1.2 Buck operation in continuous conduction mode

Figure A.2 shows the current steady-state waveforms where the inductor current flows continuously. In steady state the time integral of the inductor voltage over on time period must be zero, then:

$$(V_{dclink} - V_{UC})t_{on} - V_{dclink}t_{off} = 0 \tag{A.6}$$

Therefore, the conduction period of the switch T2 is:

$$t_{on} = \frac{V_{UC}t_{off}}{V_{dclink} - V_{UC}} \tag{A.7}$$

Dividing both sides by $T_s$, and rearranging terms:

$$\frac{V_{UC}}{V_{dclink}} = \lambda \tag{A.8}$$

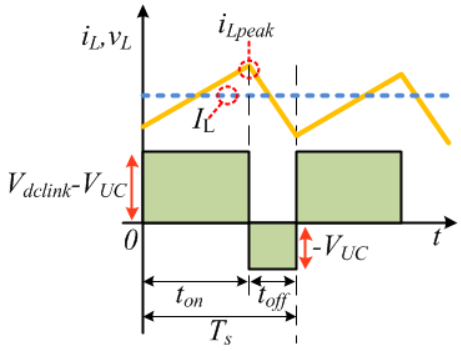


Figure A.2: Buck continuous mode.

Dividing both sides by $T_s$, and rearranging terms:

$$\frac{V_{UC}}{V_{dclink}} = \lambda \tag{A.9}$$

Assuming a circuit without losses, we get $I_L$:

$$I_L = \frac{1}{\lambda}I_{dclink} \tag{A.10}$$

### A.1.3 Buck operation at the boundary between continuous conduction and discontinuous conduction

Figure A.3 shows the waveform at the edge of continuous conduction. In this operation $i_L$ goes to zero at the end of the interval. The $I_L$' current at boundary condition is given by:

$$
\begin{aligned}
I_L' &= \frac{1}{2} I_{Lpeak} \\
I_L' &= \frac{1}{2} \frac{(V_{dclink} - V_{UC})}{L_{\min}} t_{on} \\
I_L' &= \frac{1}{2} \frac{(V_{dclink} - V_{UC})}{L_{\min}} \frac{V_{UC} T_s}{V_{dclink}} \\
I_L' &= \frac{1}{2} \frac{(V_{dclink} - V_{UC}) V_{UC} T_s}{L_{\min} V_{dclink}}
\end{aligned}
\tag{A.11}
$$

Since $I_L'=I_{UCmax}$ and $V_{UC}=V_{UCf}$, the value of $L$ to design the converter is based in the equation (A.11) in the boundary condition. Thus $L$ is:

$$
L_{\min} = \frac{1}{2} \frac{(V_{dclink} - V_{UCf}) V_{UCf} T_s}{I_{UCmax} V_{dclink}} \tag{A.12}
$$

Considering that we will have the same output power and switching period for the Boost and Buck operation. The value of the inductor will have the same value, as shown in equations (A.2) and (A.12). Therefore, we can use the same inductor for the both operation modes (Buck and Boost) in the topology presented in Figure 2.6.

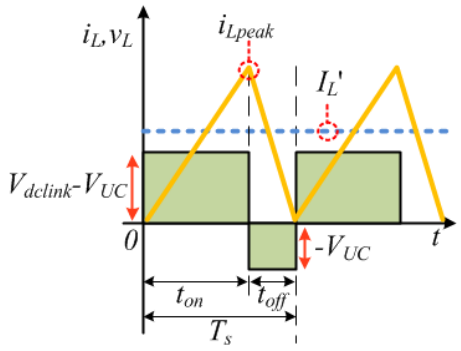


Figure A.3: Buck Boundary between continuous and discontinuous mode.

### A.1.4 Bidirectional DC-DC converter voltage gain

Theoretically, the bidirectional DC-DC converter for two quadrant boost operation has an

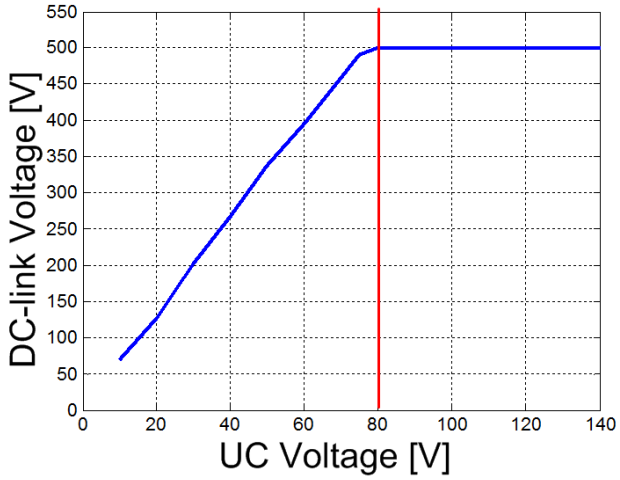


Figure A.4: UC voltage vs. DC-link voltage.

infinite voltage gain, but considering the parasitic characteristics of the converter, the voltage gain for boost operation is limited. Figure A.4 shows the experimentally acquired ultracapacitor voltage vs. DC-link voltage curve. From the Figure A.4 the final ultracapacitor voltage is $V_{UCf}$=80V.

### A.1.5 DC-link capacitor

To design the DC-link capacitor, the desired DC-link voltage ripple $\Delta V_{dclink}$ should be considered. A high voltage ripple makes a high current ripple through the ESR, increasing the temperature and the losses, that means it would be good a capacitor with a smaller ESR. The capacitor is charged during the conduction of IGBT T1 (Boost mode) and its delivers its energy during the conduction of T2 (Boost mode). Hence:

$$I = C\frac{\partial V}{\partial t}$$

$$C_{dclink} = \frac{I_{dclink} t_{on}}{\Delta V_{dclink}} \qquad (A.13)$$

$$C_{dclink} = \frac{I_{dclink} \lambda}{\Delta V_{dclink} f_s}$$

### A.1.6 PWM switch model [104]

The PWM switch model is a block that represents the total nonlinearity of the converters. This block (see Figure A.5a) has three-terminal: passive, active and common. An example, as shown in Figure A.5a, this block substitutes the real switch and diode of the depicted bidirectional DC-DC converter in buck mode.

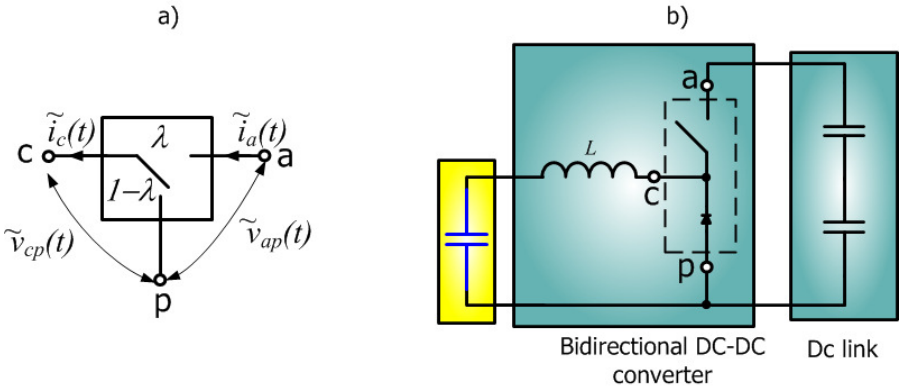


Figure A.5: a) PWM switch b) Bidirectional DC-DC converter in buck mode.

The invariant relationships between the terminal currents and voltages of the PWM switch are investigated in Figure A.6a. It can be seen that the instantaneous current in the active terminal $\tilde{i}_a$ is always the same as the current in the common terminal $\tilde{i}_c$ during the ON interval $\lambda T_s$. Also, the instantaneous voltages $\tilde{v}_{cp}(t)$ and $\tilde{v}_{ap}(t)$ are always coincident during $\lambda T_s$.

Therefore, the invariant relations in the instantaneous terminal quantities are given by:

$$\tilde{i}_a(t) = \begin{cases} \tilde{i}_c(t) & 0 \le t \le \lambda T_s \\ 0, & \lambda T_s \le t \le T_s \end{cases} \qquad (A.14)$$

$$\tilde{v}_{cp}(t)=\begin{cases}\tilde{v}_{ap}(t) & 0\le t\le \lambda T_s\\ 0, & \lambda T_s\le t\le T_s\end{cases} \tag{A.15}$$

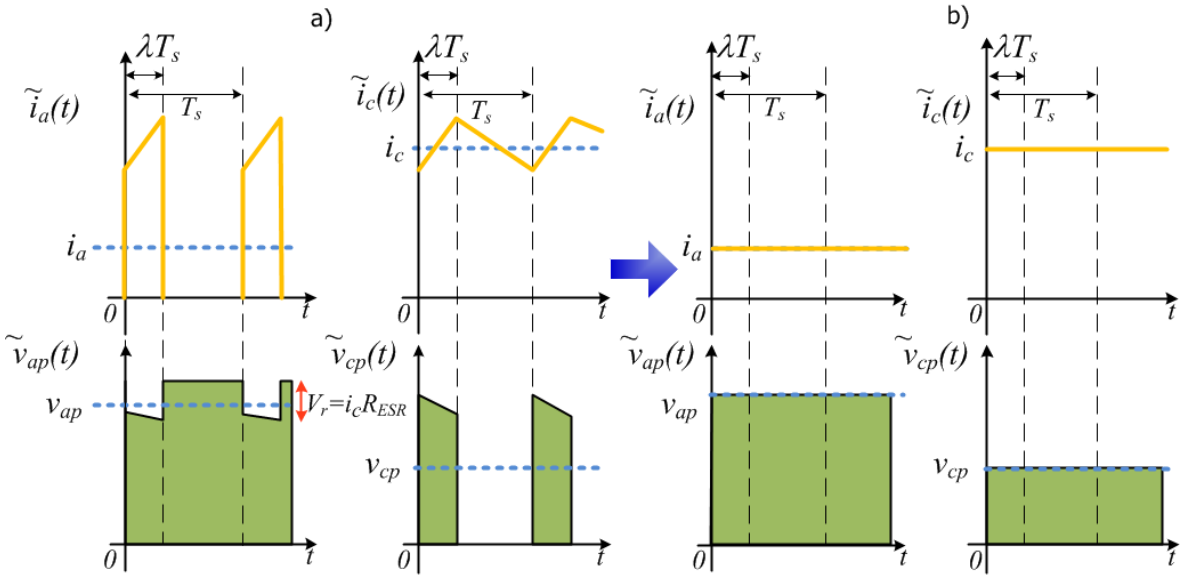


Figure A.6: a) Relation between the terminal voltages and current of the PWM switch b) Relation between the terminal voltages and current of the PWM switch neglecting the ESR voltage drop and with the averaging process.

If the voltage drop due to the ESR of the DC-link capacitor and the ripple in the current and voltage are neglected, the instantaneous voltages and currents are continuous, as shown in Figure A.6b. From Figure A.6b, we can find the behavior of the average quantities, thus the simplified relation between the average port voltages and currents are depicted in (A.16) and (A.17).

$$i_a = d i_c \tag{A.16}$$

$$v_{cp} = d v_{ap} \tag{A.17}$$

where: $d$ is the differential (small change in) of the duty cycle λ.

### A.1.6.1 DC and small signal model of the PWM switch

Now, assuming that the duty ratio is fixed at $d$=λ and the terminal voltage and currents of the PWM are perturbed due to some perturbation in either the input or output, we get:

$$\hat{i}_a = \lambda \hat{i}_c \tag{A.18}$$

$$\hat{v}_{cp} = \lambda \hat{v}_{ap} \tag{A.19}$$

The above equations correspond to the model of the PWM switch for a fixed duty cycle ratio as show in Figure A.7 which is valid for the DC analysis.

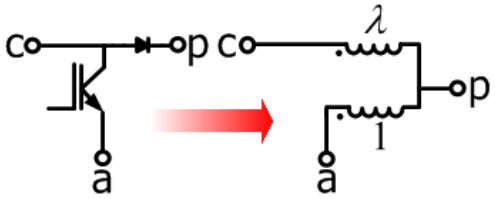


Figure A.7: Equivalent average circuit of PWM switch for fixed duty cycle.

To determine the response of a converter to perturbations in the duty cycle, then we perturb (A.16) and (A.17) as follows:

$$\hat{i}_a = \lambda \hat{i}_c + I_c \hat{d} \tag{A.20}$$

$$\hat{v}_{cp} = \lambda \hat{v}_{ap} + V_{ap} \hat{d} \tag{A.21}$$

From the above equations, the corresponding small-signal model of the PWM switch is shown in Figure A.8. The depicted model can be also valid for the DC analysis if $\hat{d}$ is considered equal to zero.

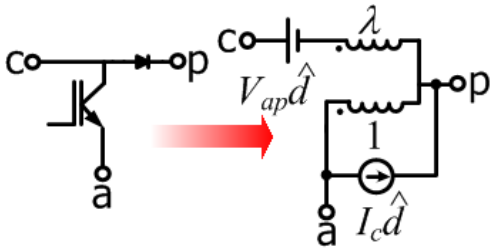


Figure A.8: Simplified dc and small-signal model of PWM switch.

### A.1.7 Small signal model for two-quadrant operation (Boost mode)

The transfer function of an average current-mode control circuit is based on the PWM switch model discussed in the previous subsection. The simplified dc and small-signal models using PWM switch model is a single block that represents the total nonlinearity of the converters and perturbations in the duty cycle. The switch depicted in the two-quadrant (Boost mode) (see Figure A.9a) is substituted by the PWM switch model (see Figure A.8), resulting in the circuit shown in Figure A.9b.

- DC analysis

A DC analysis of the circuit (Figure A.9b) is carried out. Then, DC-link capacitor (represented as a constant power source) is opened, the inductor is shorted and the duty cycle for small signal model is kept constant ($\hat{d}$ =0), as shown in Figure A.9c. Therefore:

$$V_{ap} = -V_o \tag{A.22}$$

$$I_c = 0 \tag{A.23}$$

- Control-to-voltage-output transfer function

The control-to-voltage-output transfer function is the most used transfer function for control loop analysis [51]. The DC voltage input and output (ultracapacitor and DC-Link capacitors simplified as constant voltage source) are shorted to the ground, because we only want the AC component of the transfer function. It was assumed that the DC voltage input has zero input resistance. Therefore, the DC-circuit (Figure A.8a) turns the circuit illustrated in Figure A.9b. Now, writing a voltage loop equation in the circuit we obtain:

$$v_{ap} = -v_o \tag{A.24}$$

$$R_L i_c + L i_c s - V_{ap} \hat{d} - \lambda v_{ap} - v_o = 0 \tag{A.25}$$

$$i_a = i_c \lambda + I_c \hat{d} \tag{A.26}$$

$$-i_c + i_a - i_1 = 0 \tag{A.27}$$

where: $R_L$ is the inductor resistance.

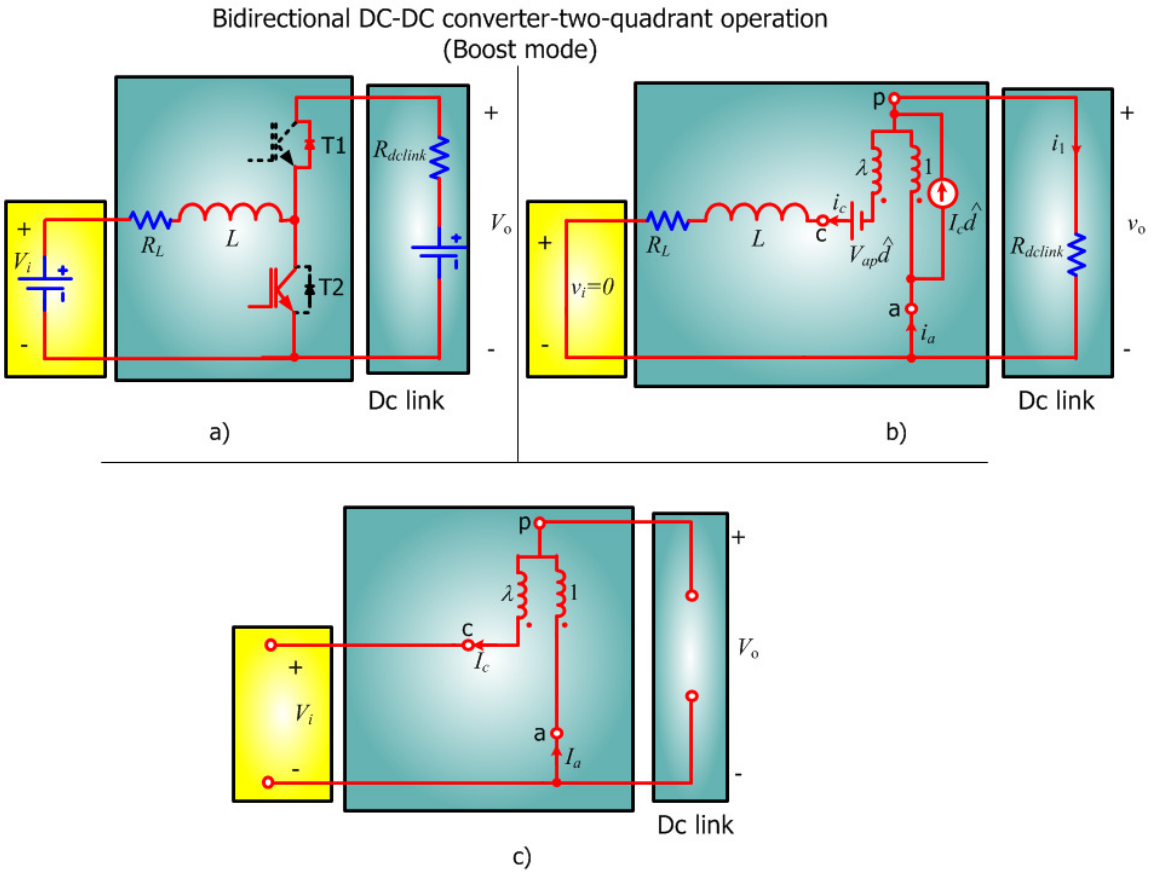


Figure A.9: a) DC model b) Small-signal model c) Small-signal model used for DC analysis.

Solving (A.26) and (A.27) we get:

$$\begin{aligned} &-i_c + i_a - i_1 = 0 \\ &-i_c + i_c\lambda + I_c\hat{d} - i_1 = 0 \\ &-i_c \underbrace{(1-\lambda)}_{\lambda'} + I_c\hat{d} - \frac{v_o}{R_{dclink}} = 0 \\ &-i_c\lambda' + I_c\hat{d} - \frac{v_o}{R_{dclink}} = 0 \end{aligned} \tag{A.28}$$

where: $R_{dclink}$ is equivalent series resistance of the DC-link capacitors.

Inserting (A.23) in (A.28) it is obtained:

$$\begin{aligned} &-i_c\lambda' - \frac{v_o}{R_{dclink}} = 0 \\ &i_c = \frac{-v_o}{R_{dclink}\lambda'} \end{aligned} \tag{A.29}$$

Solving (A.25) and (A.24) we get:

$$\begin{aligned} &R_L i_c + L i_c s - V_{ap}\hat{d} - \lambda v_{ap} - v_o = 0 \\ &(R_L + Ls) i_c - V_{ap}\hat{d} - v_o\lambda' = 0 \end{aligned} \tag{A.30}$$

Inserting (A.29) in (A.30) we obtain:

$$\left(R_L + Ls\right)\frac{-v_o}{R_{dclink}\lambda'} - V_{ap}\hat{d} - v_o\lambda' = 0$$

$$v_o = \frac{-V_{ap}\hat{d}\lambda' R_{dclink}}{Ls + \left(R_L + R_{dclink}\lambda'^2\right)} \tag{A.31}$$

Since $V_{ap}$=-$V_o$ (see Equation A.22), (A.31) can be rewritten as:

$$\frac{v_o}{\hat{d}} = \frac{V_o\lambda' R_{dclink}}{Ls + \left(R_L + R_{dclink}\lambda'^2\right)} \tag{A.32}$$

Or, using (2.5) and considering $V_o$=$v_{dclink}$=$v_{UC}$/$\lambda$' and $\hat{d} = \lambda$, we get:

$$\frac{v_{dclink}}{v_{UC}} = \frac{\lambda R_{dclink}}{Ls + \left(R_L + R_{dclink}\lambda'^2\right)} \tag{A.33}$$

Hence, the control-to-voltage-output transfer function has been completely determined.

- Control-to-current-output transfer function

Following the same conditions to find the control-voltage-output transfer function, the dc voltage input is shorted to the ground. Then, from (A.29) the output voltage $v_o$ is:

$$v_o = -i_c R_{dclink}\lambda' \tag{A.34}$$

Solving (A.30) and (A.34) we get:

$$\left(R_L + Ls\right)i_c - V_{ap}\hat{d} + i_c R_{dclink}\lambda'^2 = 0$$

$$i_c = \frac{V_{ap}\hat{d}}{Ls + \left(R_L + R_{dclink}\lambda'^2\right)} \tag{A.35}$$

As $i_c$=-$i_L$. Finally:

$$\frac{i_L}{\hat{d}} = \frac{-V_{ap}}{Ls + \left(R_L + R_{dclink}\lambda'^2\right)} \tag{A.36}$$

Or, using (2.5) and $V_{ap}$=-$V_o$ and $\hat{d} = \lambda$, we get:

$$\frac{i_L}{v_{UC}} = \frac{\lambda}{\lambda'\left(Ls + \left(R_L + R_{dclink}\lambda'^2\right)\right)} \tag{A.37}$$

- Output impedance transfer function

Dividing (A.33) by (A.37) output impedance transfer function is:

$$\frac{v_{dclink}}{i_L} = \lambda' R_{dclink} \tag{A.38}$$

### A.1.8 Small signal model for Buck operation

- DC analysis

The switch depicted in the Buck operation (see Figure A.10a) is substituted by the PWM switch model, resulting in the circuit shown in Figure A.10b.

A DC analysis of the circuit (Figure A.10b) is carried out. Then, DC-link capacitor (represented as a constant power source) is opened, the inductor is shorted and the duty cycle for small signal model is kept constant ($\hat{d}$ =0), as shown in Figure A.10c. Then:

$$V_{ap} = V_i \tag{A.39}$$

- Control-to-voltage-output transfer function

Following the same conditions to find the control-voltage-output transfer function for two-quadrant operation (Boost mode), the DC voltage input and output (DC-link capacitors and the ultracapacitor bank simplified as constant voltage source) are shorted to the ground, it was assumed that the DC voltage input has zero input resistance. Then, the DC-circuit (Figure A.10a) turns the circuit illustrated in Figure A.10b.

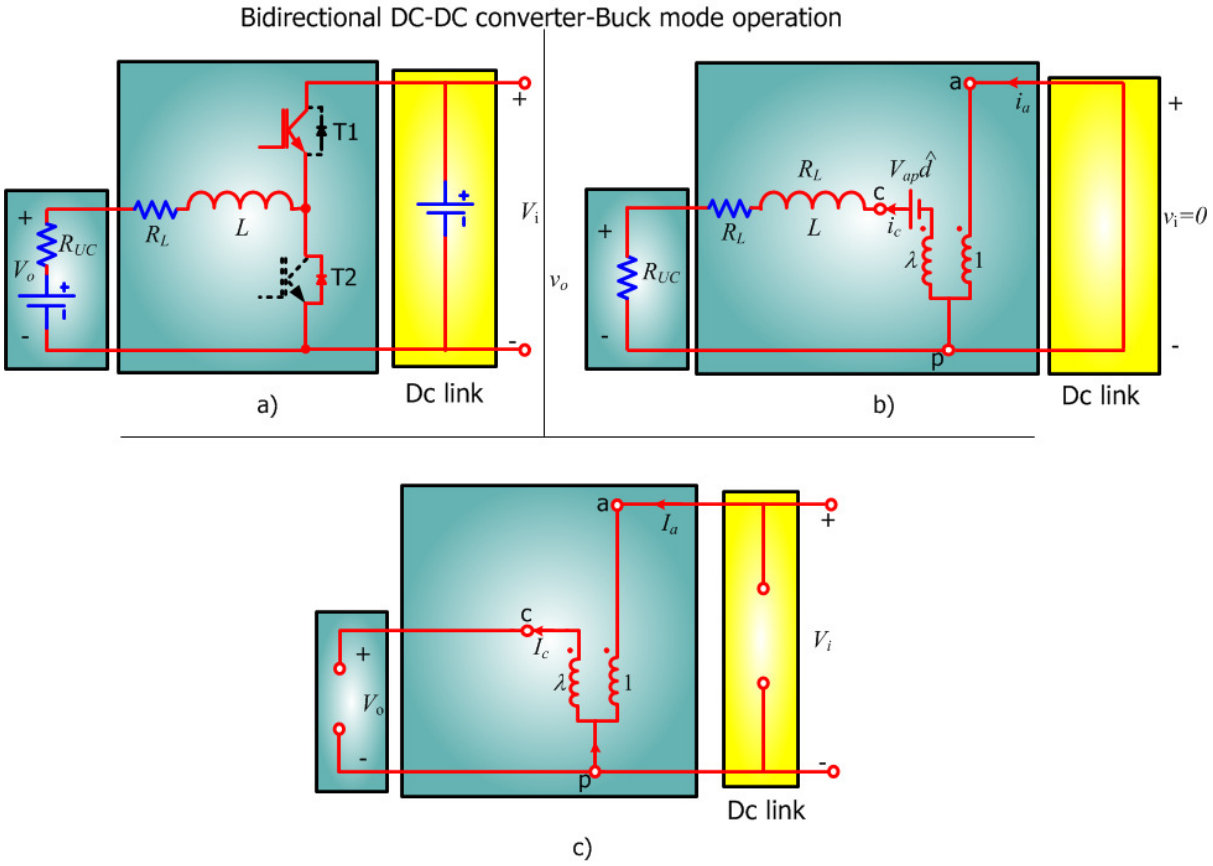


Figure A.10: a) DC model b) Small-signal model c) Small-signal model used for DC analysis.

Now, writing a voltage loop equation in the circuit we obtain:

$$v_o + R_L i_c + L i_c s - V_{ap}\hat{d} = 0 \tag{A.40}$$

$$i_c = \frac{v_o}{R_{UC}} \tag{A.41}$$

where: $R_{UC}$ is equivalent series resistance of ultracapacitor bank.

Solving (A.40) and (A.41) we get:

$$\left(\frac{Ls + (R_L + R_{UC})}{R_{uc}}\right) v_o - V_{ap}\hat{d} = 0$$

$$\frac{v_o}{\hat{d}} = \frac{V_{ap} R_{UC}}{Ls + (R_L + R_{UC})} \tag{A.42}$$

Since $V_{ap}$=$V_i$ (see Equation A.39), (A.42) can be rewritten as:

$$\frac{v_o}{\hat{d}} = \frac{V_i R_{UC}}{Ls + (R_L + R_{UC})} \tag{A.43}$$

Or, considering $V_i$=$v_{dclink}$ and $\hat{d} = \lambda$, we get:

$$\frac{v_{UC}}{v_{dclink}} = \frac{\lambda R_{UC}}{Ls + (R_L + R_{UC})} \tag{A.44}$$

- Control-to-current-output transfer function

Following the same conditions to find the control-voltage-output transfer function, the DC voltage input is shorted to the ground. Then, from (A.41) the output voltage $v_o$ is:

$$v_o = i_c R_{UC} \tag{A.45}$$

Substituting (A.45) into (A.40), we get:

$$i_c R_{UC} + R_L i_c + L i_c s - V_{ap}\hat{d} = 0$$

$$\frac{i_c}{\hat{d}} = \frac{V_{ap}}{Ls + (R_L + R_{UC})} \tag{A.46}$$

As $i_c$=$i_L$ and $V_{ap}$=$V_i$ Finally:

$$\frac{i_c}{\hat{d}} = \frac{V_i}{Ls + (R_L + R_{UC})} \tag{A.47}$$

Or, considering and $\hat{d} = \lambda$, we get:

$$\frac{i_L}{v_{dclink}} = \frac{\lambda}{Ls + (R_L + R_{UC})} \tag{A.48}$$

- Output impedance transfer function

Dividing (A.44) by (A48) output impedance transfer function is:

$$\frac{v_{UC}}{i_L} = R_{UC} \tag{A.49}$$

# Appendix B

## B.1 Clarke transformation

The stationary two-phase variables of the Clarke`s transformation are denoted as $\alpha$ and $\beta$. As depicted in Figure B.1, the $\alpha$-axis coincides with the phase-$a$ and the $\beta$-axis is 90 degree phase-shifted from the $\alpha$-axis [56][77][78]. Therefore, the transformation is bidirectional.

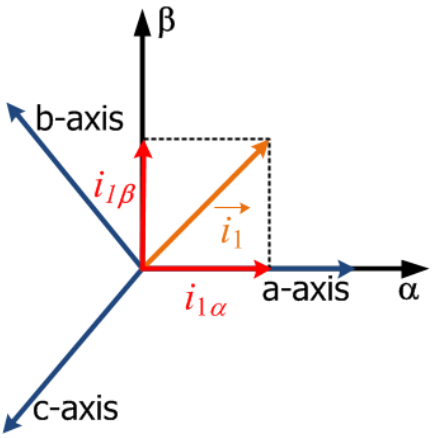


Figure B.1: Space vector in $\alpha\beta$-stationary reference frame and *abc*-stationary reference frame.

The projection of the primary current vector in this frame, not considering the zero sequence current ($i_{1a}+i_{1b}+i_{1c}=0$) yields:

$$\begin{bmatrix} i_{1\alpha} \\ i_{1\beta} \end{bmatrix} = [T_{\alpha\beta}] \begin{bmatrix} i_{1a} \\ i_{1b} \\ i_{1c} \end{bmatrix} \tag{B.1}$$

where the transformation matrix $T_{\alpha\beta}$ is given by:

$$[T_{\alpha\beta}] = \frac{2}{3} \begin{bmatrix} 1 & -\frac{1}{2} & -\frac{1}{2} \\ 0 & \frac{\sqrt{3}}{2} & -\frac{\sqrt{3}}{2} \end{bmatrix} \tag{B.2}$$

The inverse transform is:

$$\begin{bmatrix} i_{1a} \\ i_{1b} \\ i_{1c} \end{bmatrix} = \begin{bmatrix} 1 & 0 \\ -\frac{1}{2} & \frac{\sqrt{3}}{2} \\ -\frac{1}{2} & -\frac{\sqrt{3}}{2} \end{bmatrix} \begin{bmatrix} i_{1\alpha} \\ i_{1\beta} \end{bmatrix} \tag{B.3}$$

## B.2 Park transformation

The park transformation allows us to align the electrical position of the secondary flux along the *A*-axis. That means, the frame rotates with the secondary flux [56][77][78], as shown in Figure B.2.

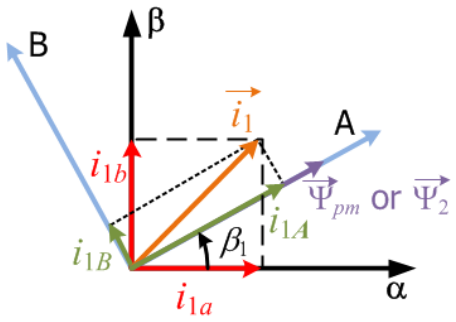


Figure B.2: Relationship between the rotating *AB*- reference frame and *αβ*-stationary reference frame

The projection of the primary current vector is:

$$\begin{bmatrix} i_{1A} \\ i_{1B} \end{bmatrix} = [T_{AB}] \begin{bmatrix} i_{1\alpha} \\ i_{1\beta} \end{bmatrix} \tag{B.4}$$

where the transformation matrix $T_{AB}$ is defined as:

$$[T_{AB}] = \begin{bmatrix} \cos(\beta_1) & \sin(\beta_1) \\ -\sin(\beta_1) & \cos(\beta_1) \end{bmatrix} \tag{B.5}$$

and the inverse is given by:

$$\begin{bmatrix} i_{1\alpha} \\ i_{1\beta} \end{bmatrix} = [T_{AB}]^{-1} \begin{bmatrix} i_{1A} \\ i_{1B} \end{bmatrix} \tag{B.6}$$

$$[T_{AB}]^{-1} = \begin{bmatrix} \cos(\beta_1) & -\sin(\beta_1) \\ \sin(\beta_1) & \cos(\beta_1) \end{bmatrix} \tag{B.7}$$

## B.3 Anti-windup PI controller

In order to avoid the unwanted integral windup, an additional logic to "switch off" the integral term in certain situations is essential, thus the integral term is kept within limits [80]. The situation occurs when a signal which is depending on the output of a controller's integrator is limited to a max- or min-value. Therefore, it can cause an oscillation and an overshoot of the controller variable around the limitation. Figure B.3 shows the block diagram for a PI controller with anti-windup.

The PI controller was discretized using the backward approximation. The algorithm of a PI controller with anti-windup is described below.

$$e[k] = r[k] - y[k]$$
$$u[k] = k_p e[k] + w[k]$$
$$if\ \left(u[k] \geq u_{\max}\right) \rightarrow u[k] = u_{\max}$$
$$if\ \left(u[k] \leq u_{\min}\right) \rightarrow u[k] = u_{\min}$$
$$w[k] = w[k-1] + \left(u[k] - w[k-1]\right)\frac{T_{sample}}{T_i}$$

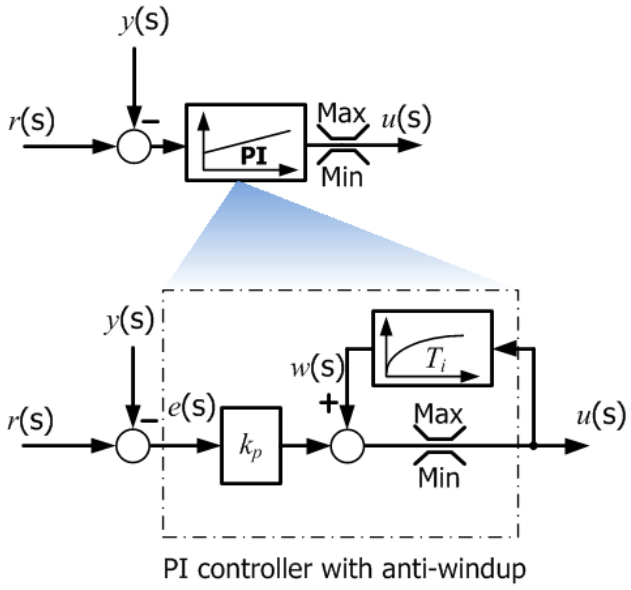


Figure B.3: PI controller with anti-windup.

## B.4 Space vector modulation

The principle of the space vector modulation is described briefly. There are eight possible combinations to produce one vector (six effective vectors and two zero vectors), as shown in Figure B.4. These vectors split the plan into six sectors, and depending on the location of the voltage reference vector $\vec{V}*$, two adjacent vectors are utilized to compose it. Thus, the given adjacent vectors are time weighted in a sample period $T_{sample}$ to produce the desired output. That is:

$$\vec{V}* = \underbrace{\vec{V}_n \frac{T_1}{T_{sample}}}_{\Delta\vec{V}_n} + \vec{V}_{n+1}\frac{T_2}{T_{sample}}, (n = 1...6) \tag{B.8}$$

where: $T_1$ and $T_2$ are the time intervals of applying $\vec{V}_n$ and $\vec{V}_{n+1}$ vectors, respectively.

The time intervals of $T_1$, $T_2$ and for $T_0$ (null-voltage vectors) are calculates as:

$$T_1 = \sqrt{3}\frac{\left|\vec{V}*\right|}{V_{dclink}} T_{sample}\left(\frac{\pi}{3} - \theta\right) \tag{B.9}$$

$$T_2 = \sqrt{3}\frac{\left|\vec{V}*\right|}{V_{dclink}} T_s \sin\left(\theta\right) \tag{B.10}$$

$$T_0 = T_{sample} - \left(T_1 + T_2\right) \tag{B.11}$$

where: $\theta$ is the phase angle of the reference voltage vector.

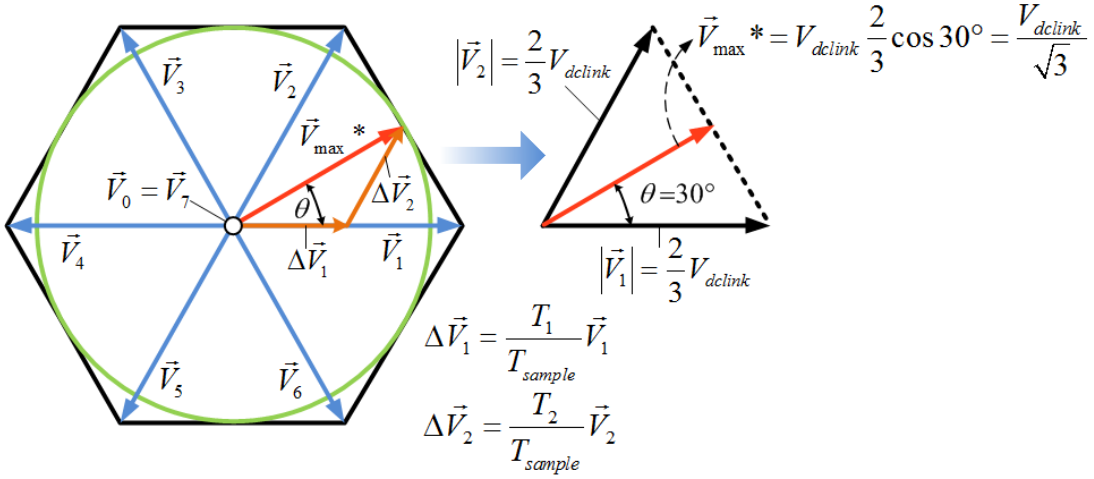


Figure B.4: Space vector diagram.

To produce a sinusoidal output voltage, the trajectory of the output voltage must trace a circle inscribed into the hexagon, as depicted in Figure B.4. Above it, the voltage waveform of the VSI is distorted. Therefore, it is recommended for high-quality servo drives to limit on the inner circle [78][80], so the modulus of the commanded voltage reference vector must not exceed:

$$V_{max}^* = \frac{V_{dclink}}{\sqrt{3}} \tag{B.12}$$

where: $V_{max}$* is the maximum value of the reference voltage vector.

The generated SV PWM waveforms are symmetrical with respect to the middle of each PWM period [77]. The Figure B.5 shows the utilized switching pattern for the reference voltage vector presented above.

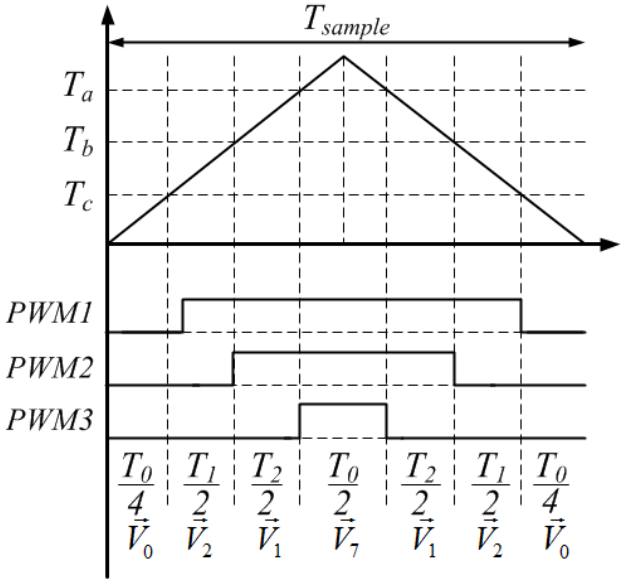


Figure B.5: A symmetric space vector PWM switching pattern.

where: $T_a$ is time compare value for the phase voltage *a*.

$T_b$ is time compare value for the phase voltage *b*.

$T_c$ is time compare value for the phase voltage *c*.

## B.5 Block diagram of the dead-time compensation using the F2812 DSP.

The DSP board has two event managers (EVM A and B) and three compare units for PWM generation. The period registers are used to produce the PWM signal carrier. The compare units (CMPR1, CMPR2, CMPR3) are updated/reloaded twice per cycle. The first update occurs in the beginning of the PWM (underflow) period and the second update in the middle of the PWM period (period match). The block diagram of the dead-time compensation using the F2812 DSP is shown in Figure B.6. From the voltage references ($u_{1a}$*, $u_{1b}$*, $u_{1c}$*), the time compare values ($T_a$, $T_b$, $T_c$) are calculated for the PWM generation. Then, the polarity of the phase current is determined. Thereafter, the compare values are added or subtracted by the specific value which is related with the dead-time $T_{dead}$, and finally they are sent to the SV PWM block, as shown in Figure B.6.

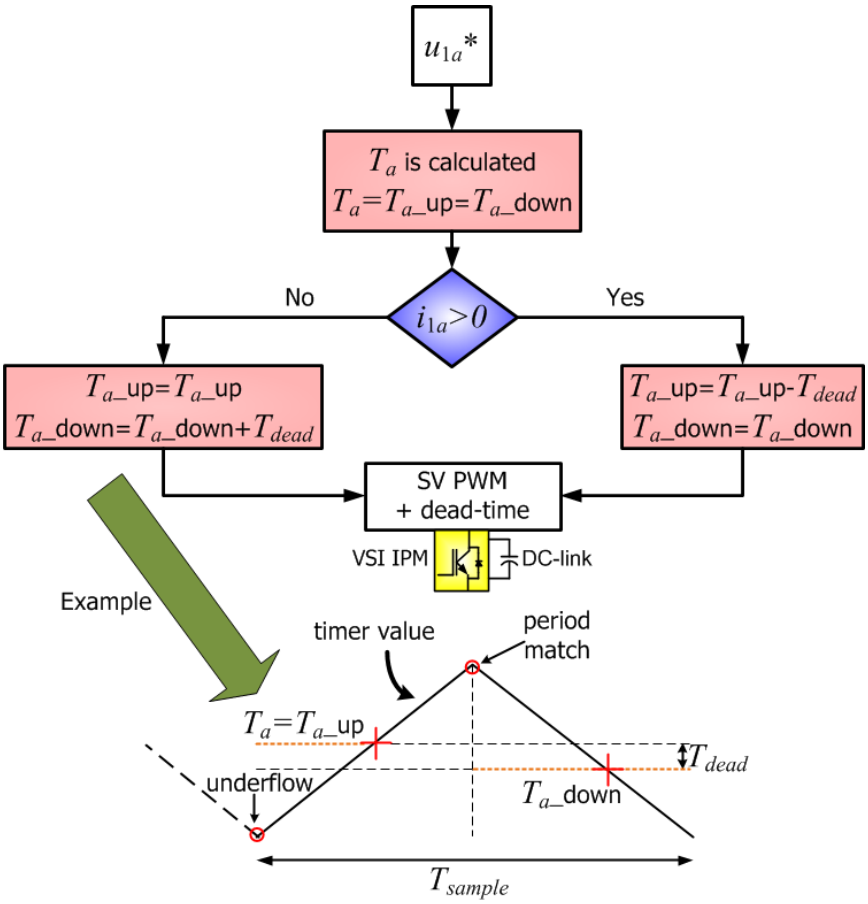


Figure B.6: Block diagram of the dead-time compensation using the F2812 DSP

# Appendix C

## C.1 Technical data of the experimental setup

| **Voltage Source Inverter (VSI)** | |
|---|---|
| DC-Link voltage | 500V |
| DC-Link capacitors | 2x680µF |
| Switching frequency | 10kHz |
| Maximal power | Up to 3.7kW |
| Snubber capacitor | 0.22 µF |
| Shunt resistors | 3x33mΩ |
| Semiconductors | IPM: PS22056, *Mitsubishi* |
| Auxiliary power supply | DC/DC-converter 40W, 24V,±15V/0.3A, 5V/6A, TEN40-2432, *TRACO* |
| **Bidirectional DC-DC converter** | |
| DC-Link voltage | 500V |
| DC-Link capacitors | 2x680µF/400V |
| Switching frequency | 15kHz |
| Maximal power | Up to 4kW |
| Snubber capacitor | 0.01 µF |
| Snubber resistances | 33Ω/5W |
| Semiconductors | IGBT Module: SKM75GB123, *Semikron* |
| IGBT driver | SKHI 22 A/B H4, *Semikron* |
| Voltage transducer | 2x LV 25-P *LEM* |
| Current transducer | LA 25-NP *LEM* |
| Inductor core | Ferrite N27, Pm 114/93, *EPCOS* |
| Ultracapacitors bank | 10x58F/15V BPAK0058 *Maxwell Technologies* |
| Auxiliary power supply | DC/DC-converter 40W, 24V,±15V/0.3A, 5V/6A, TEN40-2432, *TRACO* |

# Curriculum Vitae

M.Sc. Tobias Rafael Fernandes Neto

Born in Fortaleza-CE, Brazil, 30.09.1981

Married

| | |
|---|---|
| Since 2008 | Studying the PhD at the Department of Power Electronics and Control of Drives, Darmstadt University of Technology, Germany. |
| 2011-2012 | Working as assistant at the Department of Power Electronics and Control of Drives, Darmstadt University of Technology, Germany. |
| 2008-2012 | Full Scholarship for PhD studies in Germany granted by the CNPq (Brazilian Agency for Science and Technology) |
| 2005-2007 | Master of Science in Electrical Engineering at Universidade Federal do Ceará, Fortaleza, Brazil. |
| 1999-2004 | Bachelor of Electrical Engineering at Universidade de Fortaleza, Fortaleza, Brazil. |
| 1996-1998 | High school at Colégio Santo Inácio, Fortaleza, Brazil. |

**Publications**


[1] T.R Fernandes Neto and P. Mutschler, "Short primary linear synchronous motor drive with an ultracapacitor regenerative braking system for material handling and processing," *in 8th International Symposium on Linear Drives for Industry Applications*, 2011, LDIA'11.

[2] T.R Fernandes Neto and P. Mutschler, "Ultracapacitor energy storage system for material handling applications based on short primary linear induction drives," *in International Aegean Conference on Electric Machines and Power Electronics*, 2011, ACEMP 2011, pp. 764-769.

[3] T.R Fernandes Neto and P. Mutschler, "Combined operation of short-primary permanent magnet linear synchronous motor and linear induction motor in material handling applications," *in Applied Power Electronics Conference and Exposition*, 2012, APEC 2012, pp. 915-922.

[4] T.R Fernandes Neto and P. Mutschler, "Implementation of sensorless speed control for industrial material handling and processing applications based on short primary linear induction motor" *in IEEE International Conference on Industrial Technology*, 2012, ICIT 2012, pp. 730-735.

[5] T.R Fernandes Neto and P. Mutschler, "Motion control for short primary linear drive using induction or synchronous operation in different sections for material handling applications," *in Power Electronics, Machines and Drives Conference, 2012*, PEMD 2012.